

ENERGY HARVESTING FROM HUMAN MOTION USING
ECCENTRIC-ROTOR-BASED GENERATORS
WITH PIEZOELECTRIC TRANSDUCERS

by

Tiancheng Xue

A dissertation submitted to the faculty of
The University of Utah
in partial fulfillment of the requirements for the degree of

Doctor of Philosophy

Department of Mechanical Engineering

The University of Utah

August 2018

ProQuest Number: 10935827

All rights reserved

INFORMATION TO ALL USERS

The quality of this reproduction is dependent on the quality of the copy submitted.

In the unlikely event that the author did not send a complete manuscript and there are missing pages, these will be noted. Also, if material had to be removed, a note will indicate the deletion.



ProQuest 10935827

Published by ProQuest LLC (2020). Copyright of the Dissertation is held by the Author.

All Rights Reserved.

This work is protected against unauthorized copying under Title 17, United States Code
Microform Edition © ProQuest LLC.

ProQuest LLC
789 East Eisenhower Parkway
P.O. Box 1346
Ann Arbor, MI 48106 - 1346

Copyright © Tiancheng Xue 2018

All Rights Reserved

ABSTRACT

Inertial energy harvesting from human motion enables self-powered sensing capabilities for wearable applications. It not only allows 24/7 continuous mobile clinical health monitoring but also helps improve user experience for wearable commercial electronics by reducing battery maintenance. The inherent limitation of utilizing human motion as the source for energy harvesting is that it only provides excitations with very low and irregular frequencies, which is incompatible with conventional resonant energy harvesters. Frequency up-conversion is a commonly applied strategy to tackle this issue by transforming the low-frequency input motion into a high-frequency actuation of the transducer. In terms of piezoelectric energy harvesters, plucking a cantilever beam is one technique that applies such a strategy. Compared to the conventional translational proof mass, a rotational proof mass has no inherent motion limit. In addition, a rotational system with an eccentric weight responds to excitations in all directions. These characteristics cater to the multidirectional human motion with large amplitudes.

This project investigates the potentials, and limitation, of eccentric-rotor-based inertial wearable energy harvesting systems with the objective of determining the maximum extractable energy from human motion at various body locations and the underlying principles and design parameters needed to approach the maximum power. This is achieved with a generalized viscous-damped rotational energy harvester model that predicts the theoretical upper bound power. In addition, extensive characterization work is

conducted on electromagnetic microgenerators in existing commercial off-the-shelf watches made by Seiko and Kinetron for benchmarking. A distributed analytical model for magnetically plucked piezoelectric beams is derived and experimentally validated to study different magnetic plucking configurations. Finally, this project delivers several energy harvester prototypes utilizing custom microfabricated piezoelectric beams through a series of iterations with design-model-fabrication-characterization cycles, demonstrating the feasibility of wearable piezoelectric energy harvesting.

These days people don't read Ph.D. dissertations anyway.

- Shad Roundy

TABLE OF CONTENTS

ABSTRACT.....	iii
LIST OF TABLES.....	ix
ACKNOWLEDGMENTS.....	x
Chapters	
1. INTRODUCTION.....	1
1.1 Motivation.....	1
1.2 Energy Harvesting from Human Motion: A Review.....	3
1.3 Research Objectives.....	16
1.4 Dissertation Overview.....	17
1.5 References.....	19
2. CHARACTERIZATION OF MICROGENERATORS IN COMMERCIAL MOTION-POWERED QUARTZ WATCHES: PART I, SEIKO KINETIC.....	26
2.1 Abstract.....	27
2.2 Introduction.....	27
2.3 Model.....	28
2.4 Data Collection.....	30
2.5 Analysis on Power Output.....	31
2.6 Conclusion.....	33
2.7 Acknowledgement.....	34
2.8 References.....	34
3. CHARACTERIZATION OF MICROGENERATORS IN COMMERCIAL MOTION POWERED QUARTZ WATCHES: PART II, KINETRON MGS.....	35
3.1 Introduction.....	36
3.2 Modeling.....	38
3.3 Data Collection.....	45
3.4 Simulation and Experimental Results.....	49
3.5 Design Considerations.....	56
3.6 Conclusion.....	59
3.7 Appendix.....	59
3.8 References.....	61

4. MAGNETIC PLUCKING FOR FREQUENCY UP-CONVERTING PIEZOELECTRIC ENERGY HARVESTERS	64
4.1 Abstract.....	65
4.2 Introduction.....	65
4.3 Magnetic Plucking Configurations	66
4.4 A Model for Magnetically Plucked Piezoelectric Beams.....	69
4.5 Experimental Results	71
4.6 Conclusions.....	74
4.7 Acknowledgements.....	74
4.8 References.....	74
4.9 Biographies	75
5. DEVELOPMENT OF WRIST-WORN ROTATIONAL ENERGY HARVESTERS WITH OUT-OF-PLANE PLUCKED PIEZOELECTRIC TRANSDUCERS: PART I: ASTERISK-SHAPE THIN-FILM PIEZOELECTRIC ELEMENT.....	76
5.1 Introduction.....	76
5.2 Design and Fabrication	80
5.3 Experiment and Result.....	83
5.4 Conclusion	85
5.5 References.....	86
6. DEVELOPMENT OF WRIST-WORN ROTATIONAL ENERGY HARVESTERS WITH OUT-OF-PLANE PLUCKED PIEZOELECTRIC TRANSDUCERS: PART II: PETAL-SHAPE THIN-FILM PZT BEAMS	88
6.1 Abstract.....	89
6.2 Keywords.....	89
6.3 Introduction.....	89
6.4 Design and Modeling.....	89
6.5 Fabrication and Assembly	90
6.6 Testing Results.....	91
6.7 Conclusions.....	92
6.8 Acknowledgements.....	92
6.9 References.....	92
6.10 Contact.....	92
7. DEVELOPMENT OF WRIST-WORN ROTATIONAL ENERGY HARVESTER WITH IN-PLANE PLUCKED BIMOPRH THIN-FILM PZT BEAMS.....	93
7.1 Introduction.....	94
7.2 Generalized Rotational Harvester Model.....	97
7.3 Multibeam Harvester Development.....	102
7.4 Experiment.....	108
7.5 Conclusions.....	116
7.6 Appendix.....	117

7.7 References.....	119
8. CONCLUSIONS.....	123
8.1 Summary of Conclusions.....	123
8.2 Original Contribution.....	128
8.3 Future Work.....	129
8.4 References.....	131
APPENDIX: EXPERIMENTAL METHOD TO OBTAIN MECHANICAL DAMPING RATIO	132

LIST OF TABLES

Tables

1.1. Commercial wearable inertial energy harvesting devices	12
1.2. Published wearable inertial energy harvester prototypes.....	14
2.1. Parameters for the Seiko Kinetic Watch model.....	29
3.1. Parameters for the Kinetron MGS model	44
3.2. Real-world characterization tests.....	48
4.1. Parameters for the piezoelectric bimorph beam.....	71
7.1. Parameters for the bimorph PZT/Ni/PZT beam.....	110

ACKNOWLEDGMENTS

First, I want to express my sincere gratitude to my advisor, Prof. Shad Roundy, for becoming my Yoda and helping me grow in research and beyond. I appreciate the methodical and intellectual support as well as the liberty to define my own path. Thank you for your dedication, candor, and patience.

I want to acknowledge the financial support for this work from the National Science Foundation through the NSF Nanosystems Engineering Research Center (NERC) for Advanced Self-Powered Systems of Integrated Sensors and Technologies (ASSIST) under award number EEC 1160483. I appreciate the constant reminder that academia is after all, a business.

I would like to thank all my labmates for accompanying me on this long journey. Special thanks go to the lab gym rats, Rob, Hamid, Erik, Shane, Binh, and you-know-who. I could have graduated a little bit earlier without the peer pressure to lift weights.

I would also like to thank my ASSIST collaborators, Hong Goo Yeo, Xiaokun Ma, Miao Meng, Dixiong Wang, Profs. Susan Trolier-McKinstry, Chris Rahn, and Mehdi Kiani, for all the constructive conversations, both over the phone and in person. It has been a great pleasure to work with all of you.

Throughout my PhD years, many individuals have assisted me in various forms. I especially appreciate the commiseration, advice, and encouragement from my fellow friends in graduate schools. To Yue, Mingfeng, Huizhong, Xiaojun, and Qingbo, thank you

for enriching my life in Salt Lake. To Heng, Juanyong, Haoyang, Li, and many others scattered across the globe, I am truly grateful for your friendship.

Finally, I want to thank my parents, for leaving me alone when I needed my solitude and, above all, for indulging me and letting me stay in school for 20 years. This is for you.

CHAPTER 1

INTRODUCTION

1.1 Motivation

The wearable technology market is projected to reach USD 51.6 billion with a compound annual growth rate (CAGR) of 15.51% between 2016 and 2022 [1]. One of the major obstacles to the emerging wearable technologies, as well as other traditional electronics, is the limited single-charge lifespan of conventional batteries that rely on internal electrochemical reactions. For wearable consumer electronics, battery-related maintenance greatly undermines the user experience [2]. Some wearable/implantable healthcare applications require energy independence: clinical vital sign monitoring such as electrocardiography (ECG) requires 24/7 continuous operation [3]; the use of batteries for medical implantable sensors can lead to additional surgeries for replacement, which is inconvenient and costly. On one side, there has been continuous endeavor to boost the energy density of conventional batteries. On the other side, the reduction of power consumption has enabled the feasibility of alternative approaches to drive these low-power devices, largely thanks to the ongoing miniaturization of the semiconductor technologies. Researchers have proposed primarily two battery-alternative solutions with respect to different user cases. One solution utilizes wireless power transfer (WPT) to replace the on-site battery with a near-site source that can conveniently draw power from the grid. This

method is ideal for implanted sensors that operate intermittently or wearable sensors on hospitalized patients. Different implementations of wireless power transfer techniques including radio frequency (RF), inductive power transfer (IPT), and acoustic power transfer (APT) offer different ranges of operational frequency and distance [4]. The other solution, coined as energy harvesting (EH), scavenges power from ambient sources such as vibration, temperature gradient, and stray electromagnetic field. This approach has the potential of realizing a self-powered wearable device, which is indispensable for continuous mobile health monitoring that demands minimal maintenance. In addition, for power-hungry wearable consumer electronics, deploying energy harvesters as secondary energy sources in addition to conventional batteries can bring advantages of either a reduction of charging frequency or additional sensing modalities.

The human body is an enormous energy reservoir that dissipates energy in various forms applicable for energy harvesting, for instance, ubiquitous body motion, and perpetual body heat. This project investigates methods to harvest inertial energy from human motion primarily with piezoelectric transducers. It is part of a greater effort led by the National Science Foundation (NSF) Engineering Research Center for Advanced Self-Powered Systems for Integrated Sensors and Technologies (ASSIST). ASSIST envisions a flexible, self-powered, multimodal wearable sensing platform that enables monitoring of personal health and environmental exposure with maximum comfort and system lifetime [5]. Energy harvesting from human motion is one of the core technologies in development to realize this aim of achieving affordable long-term chronic disease prediction and treatment. In a bigger picture, general energy harvesting techniques can be transformed to other applicable areas where energy independence is required such as self-powered wireless sensor nodes

(WSN) to realize the Internet of Things (IoT).

1.2 Energy Harvesting from Human Motion: A Review

This section reviews the fundamentals and the state-of-the-art of energy harvesting with an emphasis on human motion-driven energy harvesters.

1.2.1 Energy Harvesting Fundamentals

Although the term “energy harvesting” (or “energy scavenging”) came into existence only a few decades ago, its fundamental concept, i.e., the interdomain energy transfer, has been well applied to increase productivity before the invention of engines or batteries. For instance, windmills were developed centuries ago to convert the kinetic energy from wind into rotations of windwheels to pump water or grind grain [6]. In a narrower contemporary sense, however, energy harvesting only refers to methods that convert energy from ambient sources to electricity.

The discussion of energy harvesting techniques primarily revolves around two subjects: the available energy sources, and the applicable energy transduction mechanisms. There are many surveys on energy sources in published articles with different foci [7–10]. For example, Roundy et al. reviewed different vibration sources for powering WSN [7], and Starner specifically investigated the human body as an energy source to enable wearable computing [8]. Fundamentally, most of the potential energy harvesting sources that have been discussed in the literature can be classified into three forms: electromagnetic radiant energy, thermal energy, and mechanical energy.

Since the electromagnetic radiation spans a large spectrum, it can be further divided

into different subdomains, among which light (visible and near-infrared primarily) and RF (between 10^4 and 10^{12} Hz approximately) are two commonly utilized energy harvesting sources. As a matter of fact, in present days, the most commonly seen energy harvesting techniques are solar cells that convert light into electricity via the photovoltaic effect. It is commercially available across a wide range of scales from GW level solar farms to the very popular μW level solar powered watches [11]. The primary limitation, however, is the dependence on light exposure, which significantly reduces the power capability in indoor environments or under poor weather conditions. Electromagnetic radio waves are free from weather impact, but their ubiquity is limited in urbanized areas. Prototyping and commercialization efforts have been made to utilize RF sources such as WiFi [12] and TV broadcasting [13]. RF energy harvesting relies on a resonant antenna for efficient energy capture. The same principle has been applied in other mature technologies such as Radio Frequency Identification (RFID). The achievable power levels for RF energy harvesting are limited by international rules on RF transmission and the long-term effect on health from RF exposure is still subject to debate [14,15].

Thermal energy harvesting converts a temperature difference into electricity via the Seebeck effect. A thermoelectric generator (TEG) functions like a heat engine and thus is governed by the Carnot efficiency. In addition, its performance depends on its thermoelectric figure of merit ZT , which is related to material properties. A steady temperature difference is indispensable to the functionality of TEGs. Therefore, factories and automobiles are ideal target applications where both a significant amount of waste heat and a need for continuous sensing exist [16]. There has been a growing interest in harvesting energy from body heat to power wearable electronics. Early pioneers including

Seiko and Citizen have produced thermoelectric powered wristwatches in the 1990s [17]. For a wearable TEG, the challenges lie in the small temperature difference and its susceptibility to environmental conditions. For instance, a good thermal contact to the skin and a continuous airflow over the device can greatly improve the energy generation [18]. These conditions, however, are not always guaranteed in a wearable scenario.

Although the deployment of an energy harvester is always a site-specific study with no universal solution, mechanical energy is generally viewed as a highly versatile energy harvesting source, largely thanks to the omnipresence of vibration. Williams and Yates first proposed the concept of vibration energy harvesting in 1996 [19] and since then, many early vibration energy harvester prototypes in the scale of microelectromechanical systems (MEMS) emerged in the early 2000s aiming to be the battery alternative to power μW level WSN [20–22]. These prototypes fall into the category of energy harvesters that utilize inertial forces acting on a proof mass, i.e., inertial energy harvesters. In addition, there is a different category, namely force-driven (or torque-drive) energy harvesters. A typical example of these is a shoe-mounted piezoelectric energy harvester that makes use of heel strikes [23]. Force-driven harvesters require physical connections to two different entities to allow a relative motion. Inertial harvesters hold an advantage of only needing one point of contact, as its relative motion is induced by acceleration.

For both types of mechanical harvesters, the energy conversion is achieved through a transducer that provides a damping force opposing the relative motion. There are three most commonly applied transduction mechanisms in mechanical energy harvesters: electromagnetic, electrostatic, and piezoelectric. Some other feasible, albeit not as popular, mechanisms have been proposed and implemented. One example is triboelectric energy

conversion [24]. Many comparisons of these mechanisms can be found in the literature [7,10]. As pointed out in [19], the choice of transducer is predominantly driven by practical design considerations; the selection makes little difference to the amount of achievable power in theory. Below is a brief summary of these mechanisms, highlighting piezoelectric transducers.

Electromagnetic generators are widely used in macroscale machines. The standard design incorporates a permanent magnet and a coil to induce a change in flux linkage that is eventually converted into electricity governed by Faraday's law of induction. It is well suited for rotating structures as well as translational ones. In the small scale, however, practical issues for electromagnetic transducers such as insufficient coupling at low frequencies and limited coil turns could lead to very low voltages that require an additional boost converter.

The basic idea behind electrostatic energy conversion is a capacitor with a variable gap or overlap. Mechanical work against the attraction of conductors will be converted into electricity. Electrostatic energy harvesters can function with a constant voltage or a constant charge, although real-world devices work somewhere in the middle. One drawback of electrostatic conversion is that it requires a pre-charge voltage for proper function. However, an electret can replace an active charging circuit for convenience.

Piezoelectric transducers rely on materials (e.g., crystals, certain ceramics) that exhibit the piezoelectric effect, which was first discovered by Jacques and Pierre Curie in 1880 [25]. These materials generate electric charge in response to applied mechanical stress (the converse effect). Likewise, they undergo physical deformation in the presence of an external electric field (the direct effect). A popular engineering piezoelectric material at the

present time is lead zirconate titanate (PZT, specifically $\text{PbZr}_{0.52}\text{Ti}_{0.48}\text{O}_3$), which exhibits strong electromechanical coupling after proper polarization. Other commonly used materials include aluminum nitride (AlN) and polyvinylidene fluoride (PVDF). Details of the principles of piezoelectricity can be found in the IEEE Standard on Piezoelectricity [26]. The linear constitutive equations for piezoelectricity are given by:

$$S_{ij} = s_{ijkl}^E T_{kl} + d_{kij} E_k \quad (1.1)$$

$$D_i = d_{ikl} T_{kl} + \epsilon_{ik}^T E_k \quad (1.2)$$

where S_{ij} is the strain tensor, T_{kl} the stress tensor, E_k the electric field tensor, D_i the electric displacement tensor, and s_{ijkl} , d_{ikl} , and ϵ_{ik} the elastic compliance, piezoelectric constants, and permittivity constants, respectively. Parameters with superscripts E and T are evaluated at constant electric field and constant stress, respectively. Piezoelectric energy harvesters are typically designed as cantilever composite beams with piezoelectric layer(s), which provides strain cycles under base excitation for efficient energy conversion. In addition, this arrangement is often indispensable for ceramic piezoelectric materials due to their low strain tolerance. A detailed continuum model for a bimorph piezoelectric beam will be presented in Chapter 4.

Many review articles provide more in-depth analysis specifically on piezoelectric energy harvesting [27–29]. Both piezoelectric and electrostatic devices are advantageous for MEMS integration due to their established microfabrication processes, but they typically function in the translational mode and are rarely seen in rotational structures. One advantage piezoelectric harvesters hold over electromagnetic ones is the ability to directly provide usable voltages even at small scales [30]. Many researchers characterize energy harvesters using power density as the figure of merit, which is often calculated as the power

output per unit volume. For vibration energy harvesters, the input level (acceleration amplitude and frequency) should be reflected in the figure of merit as well, but they are sometimes overlooked. Nevertheless, piezoelectric conversion is often favored over electrostatic conversion for its higher achievable power density [7,30].

1.2.2 Inertial Energy Harvesting from Human Motion

As mentioned earlier, Starner presented one of the first comprehensive reviews on the potentials of powering wearable electronics from the human body itself and concluded that the human motion provides the highest energy availability [8]. Based on the mechanical work done, upper limb motion and walking provide 60 W and 67 W of power, respectively, which are at least one order of magnitude higher than other sources. Considering the limited energy recovering ratio and other losses in practice, a more reasonable estimate of achievable power output is a few Watts. However, this level of power output requires a direct force or torque input, which can be cumbersome for users. In general, the lower body delivers a higher energy potential than the upper body. Shoe-mounted energy harvesters that rely on heel strikes likely need no additional user effort but lack local sensing demands as most of the physiological measurements are obtained from the upper body (e.g., wrist and chest). For these locations, one criterion for wearables is an unnoticeable user experience. Therefore, inertial harvesters are preferable due to a reduced adverse effect on the user.

Figure 1.1 depicts a generic inertial energy harvester first proposed by Williams and Yates. A proof mass of weight m is suspended in a frame with a relative displacement z from the input motion y . The suspension consists of a spring element k , a mechanical

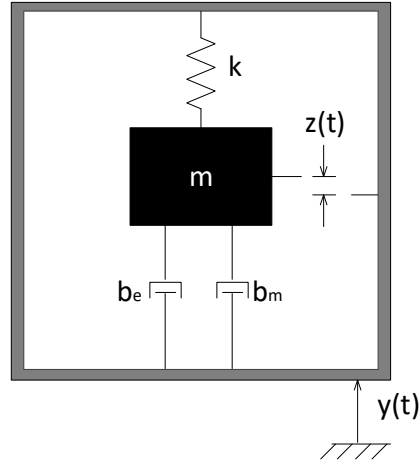


Figure 1.1. Schematic of a generic inertial energy harvester.

damper b_m , and an electrical damper b_e . The mechanical damper represents any energy loss (e.g., friction) and the electrical damper represents the transducer that extracts electrical energy from the system. By assuming harmonic excitation, with an amplitude Y_0 and angular frequency ω , the maximum attainable power for an inertial energy harvester with a mass travelled distance Z_l (zero-to-peak) is given by

$$P_{max} = \frac{2}{\pi} Y_0 Z_l \omega^3 m \quad (1.3)$$

Note that the above equation applies a constant acceleration of $Y_0 \omega^2$ to the proof mass in the direction of travel, which is manifestly an unrealistic assumption (i.e., the acceleration profile is a square wave). For a typical linear inertial harvester that operates at resonance, the acceleration and proof mass motion would be sinusoidal. A further reduction of achievable power will be imposed when specific transducer damping mechanism is introduced. Mitcheson et al. presented an analytical framework for inertial energy harvesters [31] and categorized them into three types based on the damping mechanisms: velocity-damped resonant-generator (VDRG), Coulomb-damped resonant-generator (CDRG), and Coulomb-force parametric-generator (CFPG). The VDRG model

is a fairly accurate representation for electromagnetic generators (this is reflected in Chapters 2 and 3) and can approximately model piezoelectric generators as well. Both CDRG and CFPG models can be implemented with electrostatic conversion. The optimal architecture depends on both the excitation frequency to resonance frequency ratio and the displacement ratio Z_l/Y_0 . At resonance, however, the VDRG is the superior structure when $Z_l/Y_0 > 0.1$, and its optimal power output at resonance is given by

$$P_{max,VDRG} = \frac{1}{2}Y_0Z_l\omega^3m \quad (1.3)$$

Based on the equation, one evident limiting factor for resonant energy harvesters is the size, which constrains both mass m and displacement Z_l . On the other side, resonant energy harvesters can take advantage of the peak dynamic magnification at resonance. Therefore, they are well suited for industrial applications where machine vibrations often occur in one direction with a consistent frequency signature. In general, a lower displacement amplitude is associated with a higher excitation frequency. For machine vibrations that occur between 10^1 and 10^3 Hz, the excitation amplitude (tens or hundreds of microns) is not too low for a cm-scale device to produce useful power. Naturally commercial harvesters exist for such applications [32]. However, human motion contains a high amount of arbitrary nonlinear movement that often exhibits a very low frequency and a large amplitude of displacement. This is problematic for linear resonant harvesters as such low matched frequency at small scales often requires a proof mass displacement larger than feasible. There have been attempts to drive the resonant frequency down to sub-10 Hz [33,34]. Unfortunately, these still fell short as the dominant frequencies on many body locations generally occur between 1 and 2 Hz [35]. In general, standard linear resonant harvesters suffer from low effectiveness for human applications [10].

Some alternative nonresonant approaches have been proposed to efficiently capture the inertial energy of human motion in light of its distinct characteristics. Frequency up-conversion is a commonly applied strategy by transforming the low-frequency, large-amplitude input motion into a high-frequency, small-amplitude operation of the transducer. This concept was first proposed for energy harvesting from low-frequency environmental vibrations [36] and later extended to human applications. In addition, a rotational proof mass is advantageous to a translational one for excitations with large amplitude because it has no intrinsic displacement limit. The following sections will review these techniques in detail using existing devices as examples.

1.2.3 Wearable Inertial Energy Harvesting in Commercial Consumer Electronics

The concept of inertial energy harvesting from a rotational proof mass was first materialized in mechanical self-winding watches centuries ago. The proof mass is arranged as an eccentric rotor of a semicircular shape, which responds to both linear and rotational excitations as well as any change in the direction of earth's gravitational field viewed from the frame of reference of the device. More recently, automatic quartz watches including Seiko Kinetic [37] and Swatch Autoquartz (energy generation unit made by Kinetron [38]) came on the market. Compared to mechanical self-winding watches, they utilize electromagnetic generators and quartz movements in place of mechanical movements. These watches are the first successful demonstration of wearable inertial energy harvesting techniques in the commercial space and occurred before there was much activity in the research community on small-scale energy harvesting. However, the embedded energy generating units have not been thoroughly characterized in response to real-world

excitations with a system-level model. Prior modeling endeavors tend to decouple the system from the real-world motion inputs: Wang et al. analyzed the magnetic generating rotor in the Seiko Kinetic in isolation with an optimization study on pole numbers [39]; Lossec et al. modeled the microgenerator used in the Swatch Autoquartz to study the power capability including scaling effects [40]. In addition, the actual power output of these watches under specific excitations has not been reported in any literature. As shown in Table 1.1, only vague descriptions are provided in the manuals.

As mentioned earlier, electromagnetic generators at small scales can suffer from low electromechanical coupling and low voltage output. To tackle this, both watches came up with designs to significantly increase the velocity of generating rotor and thus the coupling. Whereas the Seiko Kinetic directly adds a high-ratio gear train in the transmission, the Kinetron MGS utilizes the cogging torque commonly seen among electric motors to accumulate energy in a spring and release it at a much higher frequency. These mechanisms, however, come with a cost of a higher amount of mechanical damping from the high-speed bearings.

Benchmarking these watches is the first task of this project to fill in the gap of knowledge. Chapters 2 and 3 will present the comprehensive model-based characterization of the Seiko Kinetic and the Kinetron Micro Generator System (MGS), respectively.

Table 1.1. Commercial wearable inertial energy harvesting devices

Year	Manufacturer	Transducer	Mass Weight [g]	Volume [cm ³]	Dimension [cm]	Current claim on Power Output
1984	Kinetron bv, [38]	Electro-magnetic	4	8.2	$\phi 3.4 \times 0.9$	600 mJ (4000 revolutions) per day (MGS 26.4)
1991	Seiko Watch Corp, [37,41]	Electro-magnetic	4.7	9.2	$\phi 3.6 \times 0.9$	250 swings provide 1 day of operation (caliber 5M63)

1.2.4 Published Wearable Inertial Energy Harvester Prototypes

A list of published wearable inertial energy harvester prototypes is given in Table 1.2. As mentioned earlier, it hasn't been proven in the literature that any transduction mechanism holds fundamental advantages over others. This is reflected in published prototypes as all mechanisms have been attempted. Although rotational architectures are preferable due to their susceptibility to multi-axis excitation, there is actually an equal representation of both translational and rotational proof mass. However, the typical slender cylinder shape of translational energy harvesters is not an ideal form factor for wearables. Rotational harvesters can be made in the shape of wrist-worn watches or sewed in the fabric if sufficiently thin. A looped energy harvester in the shape of a wrist band provides an alternative form factor for wearables as well [42]. In the context of rotational structures, its equivalent eccentricity, the radius of the wristband, is much larger than other wrist watch-like devices. Yeatman first systematically analyzed rotational approaches for inertial energy harvesting with a planar model and compared 1D translational excitation against rotational excitation [43].

A displacement limit is often implemented in the form of mechanical or magnetic endstops, typically for wearable energy harvesters with translational proof mass. This constraint introduces nonlinearity and shifts the resonance characteristics of the system. Therefore, they are no longer devices with linear resonance, which can be beneficial for human motion applications (e.g., lower Q , lower dominant frequency). As a matter of fact, the energy recovery mechanism can be entirely designed in the endstops [44], which applies the frequency up-conversion principle, serving the same end as a gear train. Frequency up-conversion, primarily used in piezoelectric and electromagnetic generators,

Table 1.2. Published wearable inertial energy harvester prototypes

Year	Authors	Transducer	Mass movement and weight [g]	Volume [cm ³]	Dimension [cm]	Additional system characteristics	Claim on power output
2005	Cavallier et al., [45]	Piezoelectric	Rotational, 0.035 × 4	0.3	φ1.4 × 0.2	Impact-based	0.5 μW @ 1.4-g, 6 Hz
2007	von Büren and Tröster, [52]	Electromagnetic	1D-translational, 1.37	0.5 w/o case	N/A	Endstops	35 μW below knee from walking
2008	Saha et al., [34]	Electromagnetic	1D-translational, 27	12.7	φ1.7 × 5.5	Magnetic endstops	14.55 μW @ 0.39-g, 8 Hz
2009	Naruse et al., [53]	Electrostatic	1D-translational, N/A	N/A	2.0 × 4.5 × h	Spring	40 μW @ 0.4-g, 2 Hz
2009	Renaud et al., [46]	Piezoelectric	1D-translational, 4	25	N/A	Impact-based	400+ μW from shaking in hand @ 10 Hz with 10 cm amplitude
2009	Romero et al., [54]	Electromagnetic	Rotational, 2.2	1.5 w/o case	N/A	N/A	3.9 μW on ankle from walking
2011	Galchev et al., [44]	Electromagnetic	1D-translational, 9.3	3.8	φ1.5 × 2.7	Spring, endstops, actuation magnets	13.6 μW @ 1-g, 10 Hz
2012	Galchev et al., [49]	Piezoelectric	1D-translational, 9.3	2.8	φ1.5 × 1.4	Spring, endstops, actuation magnets	3.25 μW @ 1-g, 10 Hz
2013	Rao et al., [55]	Electromagnetic	Spherical, 8.0	39	φ3.7 × 3.5	N/A	33 μW / 100 μW on wrist from walking / jogging
2014	Halim et al., [56]	Electromagnetic	1D-translational, 4.6	7.2	φ1.4 × 5.0	Spring, endstops	110 μW from shaking in hand @ 2-g, 4.6 Hz
2014	Lockhart et al., [48]	Piezoelectric	Rotational, N/A	3.5	φ3.0 × 0.5	Mechanical pins	6 μW on wrist from walking
2014	Pillatsch et al., [50]	Piezoelectric	Rotational, 4.8	5.0	φ3.0 × 0.7	Actuation magnets	43 μW @ 2-g, 2 Hz 7 μW on upper arm from running
2015	Gutierrez et al., [57]	Electromagnetic	Planar, 4.53	N/A	φ4.4 × h	Magnetic endstops (circular)	41 μW @ 0.1-g, 8.2 Hz
2015	Ju et al., [47]	Piezoelectric	1D-translational, 1.3	4.7	2.7 × 2.7 × 0.65	Impact-based	~10 μW from pendulum (20 cm) swing @ 60 deg/s
2015	Nakano et al., [58]	Electrostatic	Rotational, N/A	N/A	φ4.0 × h	N/A	3.6 μW @ 1 rps of proof mass rotation
2015	Ylli et al., [59]	Electromagnetic	1D-translational, 9.8	21	N/A	Magnetic endstops	400 μW on foot from walking @ 4 km/h
2017	Geisler et al., [42]	Electromagnetic	Rotational, 2	21	N/A	N/A	4.8 mW on upper arm from running @ 8 km/h

can be accomplished either with mechanical contact (e.g., impact [45–47], mechanical pin [48]) or without. The contactless actuation is often achieved with magnetic coupling [44,49,50]. A magnetically plucked cantilever beam is a typical implementation of the frequency-up conversion for piezoelectric generators. This architecture is identical to the piezomagnetoelastic structure for broadband vibration energy harvesting that exhibits a strange attractor motion [51].

Some additional observations from these publications are described as follows, which will provide the basis for the significance and merit as well as some guidance for this research project:

- Previous prototyping endeavors with rotational structures rarely build upon vigorous mathematical modeling, which results in a device-specific analysis that is not generalizable. Without a generalized 3-dimensional rotational energy harvester model, some fundamental questions remained unanswered: what is the upper bound on power generation from this type of energy harvester and what are the design optimizations that can lead to the upper bound?
- A standard experimental characterization for wearable energy harvester prototypes is lacking. A certain level of arbitrariness can be seen from the selection of input in the publications including base excitations for linear oscillators and shaking-in-hand, neither of which are germane to a real-world wearable application. The ideal characterization should be a combination of repeatable on-bench tests that resemble some characteristics of human motion and real-world human subject tests.
- On the scale of wearable devices, piezoelectric transducers directly produce

voltages appropriate for rectifying. Magnetic plucking a piezoelectric beam is a frequency up-conversion technique that has been proven suitable for low-frequency inputs including human motion. The elimination of physical contact reduces mechanical loss and improves robustness. This strategy will be applied in the prototyping effort of this research project.

1.3 Research Objectives

There are three objectives to this project and they are arranged in a progressive manner as follows:

Objective 1: determine the upper bound on power generation from an eccentric-rotor-based inertial energy harvester with respect to various activities and body locations. Note that throughout the dissertation, the term eccentric-rotor-based and the term rotational are used interchangeably to describe the proposed energy harvester prototypes although the scope of rotational is larger than eccentric-rotor-based. A generalized 3-dimensional rotational harvester model is responsible for obtaining such an estimate, which not only provides insight to the potential and the practicality of wearable inertial energy harvesting, but also identifies the gap between the theoretical maximum and what has been achieved by existing devices.

Objective 2: characterize the microgenerators used in commercial off-the-shelf motion powered quartz watches. The model-based approach relies on the generalized rotational harvester model (Objective 1), which is augmented with real-world mechanical and electrical components used in the watches. Bench-top and human subject tests create new knowledge for the state-of-the-art in commercial wearable energy harvesting

capabilities. In addition, empirical corroboration enables the predictive capabilities of the system-level watch models for design optimization.

Objective 3: design, fabricate, and characterize wearable energy harvester prototypes utilizing magnetic plucked piezoelectric transducers. The third objective is realized in a series of design iterations with different magnet configurations and piezoelectric geometry in an eccentric-rotor-based wearable energy harvester. The prototyping effort relies on the experience gained from modeling (Objective 1) and benchmarking (Objective 2).

1.4 Dissertation Overview

This dissertation is divided into eight chapters that correspond to the background and motivation (Chapter 1); characterization of geared electromagnetic generators in commercial watches for benchmarking (Chapters 2 and 3); an analysis of magnetic plucking for frequency up-converting piezoelectric energy harvesters (Chapter 4); design, model, fabrication, and testing of a series of rotational energy harvester prototypes utilizing magnetically actuated piezoelectric transducers (Chapters 5-7); and the conclusion of the dissertation (Chapter 8). The piezoelectric energy harvester prototypes are made in collaboration primarily with Dr. Hong Goo Yeo and Prof. Susan Trolier-McKinstry from Pennsylvania State University who fabricate thin-film PZT beams as the piezoelectric transducers [60–62]. A generalized 3-dimensional rotational energy harvester model is referenced throughout the dissertation. The model serves not only as a tool to estimate the power upper bound on energy generation from human motion, but also as the basis of the system-level models of all the rotational energy harvester devices (Chapters 2-7). The

detailed derivation of this generalized model is included in the appendix of Chapter 7.

- Chapter 1 introduces the motivation of this project and discusses research objectives, followed by a comprehensive literature review on energy harvesting from human motion.
- Chapter 2 reports the characterization of the microgenerator in the Seiko Kinetic watch with respect to the theoretical power upper bound that includes modeling, bench-top tests, and human subject experiments. The human subject experiment data collection is carried out with a custom-made data logger. This chapter is a reprint of a conference proceeding published in *Proceedings of SPIE Vol.9801*. Note that there is an erroneous equation in this reprint. In Eq. (2.1), the first order and second order terms of the relative angular rotor displacement ϕ_z should be replaced with the terms of the absolute angular rotor displacement ψ_z .
- Chapter 3 reports the characterization of the microgenerator in the Kinetron MGS system that follows the same protocol for the Seiko Kinetic watch. The human subject data collection is carried out with a commercial off-the-shelf (COTS) data logger. This chapter is a journal manuscript that has been submitted to *IEEE/ASME Transactions on Mechatronics*.
- Chapter 4 switches gears to a study of magnetic plucking for frequency up-converting piezoelectric energy harvesters. The study compares different magnet configurations in terms of their underlying physics and evaluates their energy harvesting capabilities based on an experimentally validated model that describes the magnetically plucked piezoelectric cantilever system. Both out-

of-plane and in-plane plucking configurations are realized in later prototyping efforts (Chapter 5-7). This chapter is a reprint of a journal article that has been published in *Sensors and Actuators A: Physical*.

- Chapter 5 presents the first prototyping effort: a rotational energy harvester prototype that implements the out-of-plane plucking configuration with an asterisk-shape piezoelectric element. In addition, it includes an overview on the entire prototyping endeavors.
- Chapter 6 builds on experiences from Chapter 5 and presents an improved out-of-plane plucking design with petal-shape piezoelectric beams via modeling, design, fabrication, and testing. This chapter is a reprint of a conference proceeding published in *Transducers 2017*.
- Chapter 7 presents the final iteration of the rotational energy harvester prototype that implements the in-plane plucking configuration via modeling, design, fabrication, and a comprehensive characterization (on the basis of both individual beam and system as a whole). This chapter is a journal manuscript that has been submitted to *Smart Materials and Structures*.
- Chapter 8 summarizes the findings with a comparison between commercial geared electromagnetic generators and magnetically plucked piezoelectric generators. In addition, this chapter identifies original contributions of this project and offers suggestions for future work.

1.5 References

- [1] 2017, “Wearable Technology Market by Product (Wristwear, Headwear/Eyewear, Footwear, Neckwear, Bodywear), Type (Smart Textile, Non-Textile), Application

- (Consumer Electronics, Healthcare, Enterprise & Industrial), and Geography - Global Forecast to 2022,” marketsandmarkets.com [Online]. Available: <https://www.marketsandmarkets.com/Market-Reports/wearable-electronics-market-983.html>. [Accessed: 22-Jan-2018].
- [2] Ballard, B., 2007, *Designing the Mobile User Experience*, Wiley.
- [3] Pantelopoulos, A., and Bourbakis, N. G., 2010, “A Survey on Wearable Sensor-Based Systems for Health Monitoring and Prognosis,” *IEEE Trans. Syst. Man Cybern. Part C Appl. Rev.*, **40**(1), pp. 1–12.
- [4] Basaeri, H., Christensen, D. B., and Roundy, S., 2016, “A Review of Acoustic Power Transfer for Bio-Medical Implants,” *Smart Mater. Struct.*, **25**(12), p. 123001.
- [5] Misra, V., Bozkurt, A., Calhoun, B., Jackson, T., Jur, J., Lach, J., Lee, B., Muth, J., Oralkan, O., Ozturk, M., Trolier-McKinstry, S., Vashae, D., Wentzloff, D., and Zhu, Y., 2015, “Flexible Technologies for Self-Powered Wearable Health and Environmental Sensing,” *Proc. IEEE*, **103**(4), pp. 665–681.
- [6] Hills, R. L., 1996, *Power from Wind : A History of Windmill Technology*, Cambridge University Press.
- [7] Roundy, S., Wright, P. K., and Rabaey, J., 2003, “A Study of Low Level Vibrations As a Power Source for Wireless Sensor Nodes,” *Comput. Commun.*, **26**(11), pp. 1131–1144.
- [8] Starner, T., 1996, “Human-Powered-Wearable-Computing,” *IBM Syst. J.*, **35**(3.4), pp. 618–629.
- [9] Romero, E., Warrington, R. O., and Neuman, M. R., 2009, “Energy Scavenging Sources for Biomedical Sensors,” *Physiol. Meas.*, **30**(9), pp. R35–R62.
- [10] Mitcheson, P. D., Yeatman, E. M., Rao, G. K., Holmes, A. S., and Green, T. C., 2008, “Energy Harvesting From Human and Machine Motion for Wireless Electronic Devices,” **96**(9), pp. 1457–1486.
- [11] Parida, B., Iniyar, S., and Goic, R., 2011, “A Review of Solar Photovoltaic Technologies,” *Renew. Sustain. Energy Rev.*, **15**(3), pp. 1625–1636.
- [12] “PCC110/PCC210” [Online]. Available: <http://www.powercastco.com/wp-content/uploads/2016/12/PCC110-PCC210-Overview-V1.4.pdf>. [Accessed: 14-Feb-2018].
- [13] Nishimoto, H., Kawahara, Y., and Asami, T., 2010, “Prototype Implementation of Ambient RF Energy Harvesting Wireless Sensor Networks,” *2010 IEEE Sensors*, IEEE, pp. 1282–1287.

- [14] Rössli, M., 2008, “Radiofrequency Electromagnetic Field Exposure and Non-Specific Symptoms of Ill Health: A Systematic Review,” *Environ. Res.*, **107**(2), pp. 277–287.
- [15] Calvente, I., Pérez-Lobato, R., Núñez, M.-I., Ramos, R., Guxens, M., Villalba, J., Olea, N., and Fernández, M. F., 2016, “Does Exposure to Environmental Radiofrequency Electromagnetic Fields Cause Cognitive and Behavioral Effects in 10-Year-Old Boys?,” *Bioelectromagnetics*, **37**(1), pp. 25–36.
- [16] Yang, J., 2005, “Potential Applications of Thermoelectric Waste Heat Recovery in the Automotive Industry,” *ICT 2005. 24th International Conference on Thermoelectrics, 2005.*, IEEE, pp. 170–174.
- [17] Kishi, M., Nemoto, H., Hamao, T., Yamamoto, M., Sudou, S., Mandai, M., and Yamamoto, S., “Micro Thermoelectric Modules and Their Application to Wristwatches as an Energy Source,” *Eighteenth International Conference on Thermoelectrics. Proceedings, ICT’99 (Cat. No.99TH8407)*, IEEE, pp. 301–307.
- [18] Hyland, M., Hunter, H., Liu, J., Veety, E., and Vashae, D., 2016, “Wearable Thermoelectric Generators for Human Body Heat Harvesting,” *Appl. Energy*, **182**, pp. 518–524.
- [19] Williams, C. B., and Yates, R. B., 1996, “Analysis of a Micro-Electric Generator for Microsystems,” *Sensors Actuators A Phys.*, **52**, pp. 8–11.
- [20] Williams, C. B., Shearwood, C., Harradine, M. A., Mellor, P. H., Birch, T. S., and Yates, R. B., 2001, “Development of an Electromagnetic Micro-Generator,” *IEE Proc. - Circuits, Devices Syst.*, **148**(6), p. 337.
- [21] Meninger, S., Mur-Miranda, J. O., Amirtharajah, R., Chandrakasan, A., and Lang, J. H., 2001, “Vibration-to-Electric Energy Conversion,” *IEEE Trans. Very Large Scale Integr. Syst.*, **9**(1), pp. 64–76.
- [22] Roundy, S., Wright, P. K., and Pister, K. S. J., 2002, “Micro-Electrostatic Vibration-to-Electricity Converters,” *Microelectromechanical Systems*, ASME, pp. 487–496.
- [23] Shenck, N. S., and Paradiso, J. A., 2001, “Energy Scavenging with Shoe-Mounted Piezoelectrics,” *IEEE Micro*, **21**(3), pp. 30–42.
- [24] Dhakar, L., Liu, H., Tay, F. E. H., and Lee, C., 2013, “A Wideband Triboelectric Energy Harvester,” *J. Phys. Conf. Ser.*, **476**(1), p. 12128.
- [25] Curie, J., and Curie, P., 1880, “Développement Par Compression de L’électricité Polaire Dans Les Cristaux Hémihédres À Faces Inclinaées,” *Bull. la Société minérolgique Fr.*, **3**, pp. 90–93.
- [26] Standards Committee of the IEEE Ultrasonics Ferroelectrics and Frequency Control

Society, 1988, *IEEE Standard on Piezoelectricity*, IEEE, New York.

- [27] Sodano, H. A., Inman, D. J., and Park, G., 2004, “A Review of Power Harvesting from Vibration Using Piezoelectric Materials,” *Shock Vib. Dig.*, **36**(3), pp. 197–205.
- [28] Anton, S. R., and Sodano, H. A., 2007, “A Review of Power Harvesting Using Piezoelectric Materials (2003–2006),” *Smart Mater. Struct.*, **16**(3), pp. R1–R21.
- [29] Priya, S., 2007, “Advances in Energy Harvesting Using Low Profile Piezoelectric Transducers,” *J. Electroceramics*, **19**(1), pp. 167–184.
- [30] Cook-Chennault, K. A., Thambi, N., and Sastry, A. M., 2008, “Powering MEMS Portable Devices—a Review of Non-Regenerative and Regenerative Power Supply Systems with Special Emphasis on Piezoelectric Energy Harvesting Systems,” *Smart Mater. Struct.*, **17**(4), p. 43001.
- [31] Mitcheson, P. D., Green, T. C., Yeatman, E. M., and Holmes, A. S., 2004, “Architectures for Vibration-Driven Micropower Generators,” *J. Microelectromechanical Syst.*, **13**(3), pp. 1–12.
- [32] “microGen Systems – Providing Energy Harvester-Based Power Solutions to the Connected World.” [Online]. Available: <https://www.microgensystems.com/>. [Accessed: 27-Feb-2018].
- [33] Tashiro, R., Kabei, N., Kotera, H., Katayama, K., Ishizuka, Y., Tsuboi, F., and Tsuchiya, K., 2001, “Development of an Electrostatic Generator That Harnesses the Motion of a Living Body. Generation Using Heartbeat,” *Trans. Japan Soc. Mech. Eng. Ser. C*, **67**(659), pp. 2307–2313.
- [34] Saha, C. R., O’Donnell, T., Wang, N., and McCloskey, P., 2008, “Electromagnetic Generator for Harvesting Energy from Human Motion,” *Sensors Actuators A Phys.*, **147**(1), pp. 248–253.
- [35] Yun, J., Patel, S. N., Reynolds, M. S., and Abowd, G. D., 2011, “Design and Performance of an Optimal Inertial Power Harvester for Human-Powered Devices,” *IEEE Trans. Mob. Comput.*, **10**(5), pp. 669–683.
- [36] Kulah, H., and Najafi, K., 2008, “Energy Scavenging From Low-Frequency Vibrations by Using Frequency Up-Conversion for Wireless Sensor Applications,” *IEEE Sens. J.*, **8**(3), pp. 261–268.
- [37] Hayakawa, M., 1991, “Electronic Wristwatch with Generator.”
- [38] Kinetron, 2014, “Micro Generator System ‘26.4’” [Online]. Available: <http://www.kinetron.eu/wp-content/uploads/2015/01/MGS-26.4.pdf>. [Accessed:

01-Sep-2017].

- [39] Wang, J., Wang, W., Jewell, G. W., and Howe, D., 2005, "Design of a Miniature Permanent-Magnet Generator and Energy Storage System," *IEEE Trans. Ind. Electron.*, **52**(5), pp. 1383–1390.
- [40] Lossec, M., Multon, B., Ahmed, H. Ben, and Ben Ahmed, H., 2010, "Micro-Kinetic Generator: Modeling, Energy Conversion Optimization and Design Considerations," *MELECON 2010 - 2010 15th IEEE Mediterr. Electrotech. Conf.*, pp. 1516–1521.
- [41] Seiko, "Cal. 3M62, 5M62, 5M63" [Online]. Available: https://www.seikowatches.com/support/ib/pdf/SEIKO_3M62_5M62_5M63.pdf. [Accessed: 01-Sep-2017].
- [42] Geisler, M., Boisseau, S., Gasnier, P., Willemin, J., Gobbo, C., Despesse, G., Ait-Ali, I., and Perraud, S., 2017, "Looped Energy Harvester for Human Motion," *Smart Mater. Struct.*, **26**(10), p. 105035.
- [43] Yeatman, E. M., 2008, "Energy Harvesting from Motion Using Rotating and Gyroscopic Proof Masses," *Proc. Inst. Mech. Eng. Part C J. Mech. Eng. Sci.*, **222**(1), pp. 27–36.
- [44] Galchev, T., Kim, H., and Najafi, K., 2011, "Micro Power Generator for Harvesting Low-Frequency and Nonperiodic Vibrations," *J. Microelectromechanical Syst.*, **20**(4), pp. 852–866.
- [45] Cavallier, B., Berthelot, P., Nouria, H., Foltete, E., Hirsinger, L., and Ballandras, S., "Energy Harvesting Using Vibrating Structures Excited by Shock," *IEEE Ultrasonics Symposium, 2005.*, IEEE, pp. 943–945.
- [46] Renaud, M., Fiorini, P., van Schaijk, R., and van Hoof, C., 2009, "Harvesting Energy from the Motion of Human Limbs: The Design and Analysis of an Impact-Based Piezoelectric Generator," *Smart Mater. Struct.*, **18**(3), p. 35001.
- [47] Ju, S., and Ji, C.-H., 2015, "Piezoelectric Vibration Energy Harvester Using Indirect Impact of Springless Proof Mass," *J. Phys. Conf. Ser.*, **660**, p. 12122.
- [48] Lockhart, R., Janphuang, P., Briand, D., and De Rooij, N. F., 2014, "A Wearable System of Micromachined Piezoelectric Cantilevers Coupled to a Rotational Oscillating Mass for on-Body Energy Harvesting," *Proc. IEEE Int. Conf. Micro Electro Mech. Syst.*, pp. 370–373.
- [49] Galchev, T., Aktakka, E. E., and Najafi, K., 2012, "A Piezoelectric Parametric Frequency Increased Generator for Harvesting Low-Frequency Vibrations," *J. Microelectromechanical Syst.*, **21**(6), pp. 1311–1320.

- [50] Pillatsch, P., Yeatman, E. M., and Holmes, A. S., 2014, "A Piezoelectric Frequency up-Converting Energy Harvester with Rotating Proof Mass for Human Body Applications," *Sensors Actuators, A Phys.*, **206**, pp. 178–185.
- [51] Erturk, A., Hoffmann, J., and Inman, D. J., 2009, "A Piezomagnetoelastic Structure for Broadband Vibration Energy Harvesting," *Appl. Phys. Lett.*, **94**(25), pp. 92–95.
- [52] von Büren, T., and Tröster, G., 2007, "Design and Optimization of a Linear Vibration-Driven Electromagnetic Micro-Power Generator," *Sensors Actuators A Phys.*, **135**(2), pp. 765–775.
- [53] Naruse, Y., Matsubara, N., Mabuchi, K., Izumi, M., and Suzuki, S., 2009, "Electrostatic Micro Power Generation from Low-Frequency Vibration such as Human Motion," *J. Micromechanics Microengineering*, **19**(9), p. 94002.
- [54] Romero, E., Warrington, R. O., and Neuman, M. R., 2009, "Body Motion for Powering Biomedical Devices," *Proc. 31st Annu. Int. Conf. IEEE Eng. Med. Biol. Soc. Eng. Futur. Biomed. EMBC 2009*, pp. 2752–2755.
- [55] Rao, Y., McEachern, K. M., and Arnold, D. P., 2013, "A Compact Human-Powered Energy Harvesting System," *J. Phys. Conf. Ser.*, **476**, p. 12011.
- [56] Halim, M. A., and Park, J. Y., 2014, "A Non-Resonant, Frequency up-Converted Electromagnetic Energy Harvester from Human-Body-Induced Vibration for Hand-Held Smart System Applications," *J. Appl. Phys.*, **115**(9).
- [57] Gutierrez, M., Shahidi, A., Berdy, D., and Peroulis, D., 2015, "Design and Characterization of a Low Frequency 2-Dimensional Magnetic Levitation Kinetic Energy Harvester," *Sensors Actuators A Phys.*, **236**, pp. 1–10.
- [58] Nakano, J., Komori, K., Hattori, Y., and Suzuki, Y., 2015, "MEMS Rotational Electret Energy Harvester for Human Motion," *J. Phys. Conf. Ser.*, **660**, p. 12052.
- [59] Ylli, K., Hoffmann, D., Willmann, A., Becker, P., Folkmer, B., and Manoli, Y., 2015, "Energy Harvesting from Human Motion: Exploiting Swing and Shock Excitations," *Smart Mater. Struct.*, **24**(2), p. 25029.
- [60] Yeo, H. G., and Trolier-McKinstry, S., 2014, "{001} Oriented Piezoelectric Films Prepared by Chemical Solution Deposition on Ni Foils," *J. Appl. Phys.*, **116**(1), p. 14105.
- [61] Yeo, H. G., Ma, X., Rahn, C., and Trolier-McKinstry, S., 2016, "Efficient Piezoelectric Energy Harvesters Utilizing (001) Textured Bimorph PZT Films on Flexible Metal Foils," *Adv. Funct. Mater.*, **26**(32), pp. 5940–5946.
- [62] Yeo, H. G., 2017, "Mechanical Energy Harvesters Utilizing {001} Textured PZT

Films on Flexible Metal Foils,” Ph.D. Dissertation, The Pennsylvania State University, University Park, PA.

CHAPTER 2

CHARACTERIZATION OF MICROGENERATORS IN
COMMERCIAL MOTION-POWERED
QUARTZ WATCHES: PART I,
SEIKO KINETIC

© 2016 SPIE. Reprinted, with permission from, T. Xue, S. Kakkar, Q. Lin, and S. Roundy, “Characterization of micro-generators embedded in commercial-off-the-shelf watches for wearable energy harvesting,” in *Proceedings of SPIE - The International Society for Optical Engineering*, 2016, vol. 9801, p. 98010O.

Note that there is an erroneous equation in this reprint. In Eq. (2.1), the first order and second order terms of the relative angular rotor displacement ϕ_z should be replaced with the terms of the absolute angular rotor displacement ψ_z .

Characterization of Micro-Generators Embedded in Commercial-Off-the-Shelf Watches for Wearable Energy Harvesting

Tiancheng Xue^{*a}, Shantnu Kakkar^a, Qianyu Lin^b and Shad Roundy^a

^aUniversity of Utah, Dept. of Mech. Eng., 1495 E 100 S, Salt Lake City, UT 84112, USA;

^bDuke University, Durham, NC 27708, USA

ABSTRACT

This paper presents the characterization of the micro-generators embedded in Commercial-Off-The-Shelf (COTS) watches based on a generalized rotational energy harvester model which predicts the upper bound on energy generation given certain system constraints and specific inputs. We augment this generalized model to represent the actual micro-generator used in the Seiko Kinetic watch with realistic damping coefficients which allow us to identify optimizations to move the system output towards the upper bound. We have developed a mobile data logging platform which captures 6 DOF inertia data and the voltage output from the micro-generator simultaneously. We have asked 6 subjects to conduct a series of daily activities with the platform worn on different locations of the body. This effort not only serves as the experimental validation of our model but also provides insight into the state of the art in wearable kinetic energy harvesting devices that are commercially available. Finally we identify the opportunity for improvement on energy generation and show that we can increase the power by reducing the mechanical damping in the system, which might require an alternative mechanism with inherent lower friction.

Keywords: Energy harvesting, micro-generator, wearable, watch, characterization

1. INTRODUCTION

Energy harvesting provides a promising solution to powering wearable sensors 24/7 as the limited battery life is one the major obstacles to the emerging wearable technologies. The challenge of harnessing kinetic energy from the human body lies in the unpredictable nature of the low-frequency dominated human motion. Frequency up-conversion, usually achieved through plucking a piezoelectric element, is often applied in reported wearable energy harvester prototypes¹⁻³ to bridge the gap between the non-periodic excitation and the conventional resonant transducer. Different means to the same end, however, have already been taken in some of the COTS motion-powered quartz watches such as the Seiko Kinetic, the Swatch Autoquartz and the Citizen Eco-Drive Duo models.

Motion-powered quartz watches are a successful demonstration of energy harvesting technologies in commercial applications. These watch movements are classified as automatic quartz, which combines the advantages of an automatic watch (free from battery replacement) and a quartz watch (accuracy). Interestingly some of these watches came into the market before there was much activity in the research community on small scale energy harvesting. Yet the micro-generators embedded in these watches have not been thoroughly characterized in response to a real-world excitations with a system-level model to the authors' knowledge. Prior modeling endeavors tend to decouple the system from the real-world motion input: Wang *et al.* analyzed the magnetic generating rotor in the Seiko Kinetic in isolation with an optimization study on pole numbers⁴; Lossec *et al.* modeled the micro-generator used in Swatch Autoquartz with analysis on power capability including scaling effects⁵. In addition, the actual power output of these micro-generators under specific excitation hasn't been reported in any literature. Rough estimates such as 5 μ W average from the Seiko Kinetic² or 600 mJ per day from the MGS26.4 fabricated by Kinetron (supplier of the micro-generators used in Swatch Autoquartz)⁶ exist in prior research publications or manuals provided by the manufacturers.

In this paper we characterize the micro-generators embedded in COTS watches with a primary focus on the Seiko Kinetic. Currently all the commercially available micro-generators apply the electromagnetic induction according to Faraday's Law to convert the rotation of the eccentric weight to electricity. These watches typically implement a sophisticated speed conversion mechanism in order to directly obtain a useful voltage instead of employing a boost converter. The Seiko Kinetic uses a high ratio gear train to increase the speed while the Kinetron micro-generator applies a torsional spring as

* tiancheng.xue@utah.edu

an intermediate energy storage. In principal, all these micro-generators can be modeled as an ideal rotational energy harvester with a semicircular disk as the proof mass. This generalized model predicts the upper bound on energy generation given certain inputs while the augmented model for the actual micro-generator with specific speed conversion mechanism and other realistic constraints allows us to identify optimizations that could be made to move the system output towards the upper bound. We have developed a mobile data logging platform to capture the 6 DOF inertia data and the power output from the Seiko Kinetic watch simultaneously from real-world tests to serve as the inputs to the simulation and the experimental validation of our model respectively.

2. MODEL

2.1 Generalized rotational energy harvester model

The characterization of the micro-generators is based on a published generalized rotational harvester model⁷ which predicts the upper bound on energy generation given 6 axis motion input and system constraints such as rotational inertia, eccentricity, etc. An electrical and a mechanical rotational damper are included in the model to represent extracted and lost energy respectively. This model is an analogy to the linear velocity damped resonant generator (VDRG) model⁸, making the assumption that the power dissipated through an optimal viscous damper that represents the electromechanical transducer is the maximum electrical power that can be extracted from the system. All eccentric-rotor based energy harvesters including the Seiko Kinetic should in theory be limited by the predicted upper bound on power output.

The 3 dimensional model accounts for 6 axis inertial inputs. The harvester can be excited either linearly, rotationally or both. As illustrated in Figure 1, the rotation of the eccentric mass is constrained in the XY plane and the governing equations in the local XYZ coordinate are given by:

$$m \begin{bmatrix} -l \cos \phi_z \cdot \dot{\phi}_z^2 - l \sin \phi_z \cdot \ddot{\phi}_z \\ -l \sin \phi_z \cdot \dot{\phi}_z^2 - l \cos \phi_z \cdot \ddot{\phi}_z \end{bmatrix} = -m \begin{bmatrix} \ddot{X} \\ \ddot{Y} \end{bmatrix} + \begin{bmatrix} F_x \\ F_y \end{bmatrix} + m \begin{bmatrix} g_x \\ g_y \end{bmatrix} \quad (1)$$

$$I_G \ddot{\theta}_z = -I_G \ddot{\phi}_z - (D_e + D_m) \dot{\phi}_z + F_x l \sin \phi_z - F_y l \cos \phi_z \quad (2)$$

Where m , I_G , and l are the mass, the moment of inertia and the eccentric distance of the rotor respectively. \ddot{X} , \ddot{Y} are the linear acceleration inputs to the system. F_x , F_y and g_x , g_y are the forces from the supporting shaft and the gravitational acceleration respectively in each local coordinate. ϕ_z denotes the relative angular displacement between the rotor and the housing, which determines the power output as:

$$P = D_e \dot{\phi}_z^2 \quad (3)$$

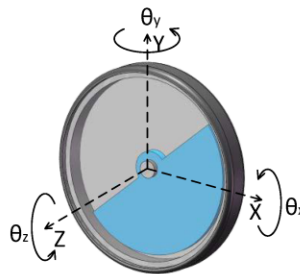


Figure 1. Dynamic model of the eccentric-rotor based rotational energy harvester

2.2 Seiko Kinetic model

The Kinetic series was first introduced by Seiko in 1986. Kinetic models with slightly different functions have come into market since its first release. The fundamental energy generation unit, however, hasn't changed much to the authors' knowledge. The only apparent improvement is that a rechargeable lithium ion battery replaced the original capacitor.

We augmented the generalized rotational energy harvester model with realistic damping coefficients to match the actual components in the 5M63, the caliber in the Seiko Kinetic watch that we analyzed in this paper. We reassembled the energy

generation unit with partial parts to identify individual mechanical loss qualitatively in each component. We applied the standard logarithmic decrement method to obtain the damping ratios quantitatively. The damping coefficients were tuned in the model to match the experimental results.

As shown in Figure 2, the energy generation unit consists of an oscillating weight, a 3-gear train, a magnetic generating rotor, a generating coil and a battery. The oscillating weight is supported by a ball bearing, which is associated with a viscous damping loss. Although Seiko claims that the rotor is suspended with magnetic levitation with no friction, by our inspection, the rotor and other gears are still supported by the standard jewel bearings used in the watch industry. Granting the fact that jewel bearings only operate well for low speed rotation, the suspension of the generating rotor is indispensable for this design to work yet hard to verify. We lump all the mechanical loss associated with the jewel bearings and gear train transmission into a coulomb damper and a viscous damper. The electromagnetic transducer is modeled as a viscous damper with respect to the generating rotor rather than the oscillating weight as in the generalized model.

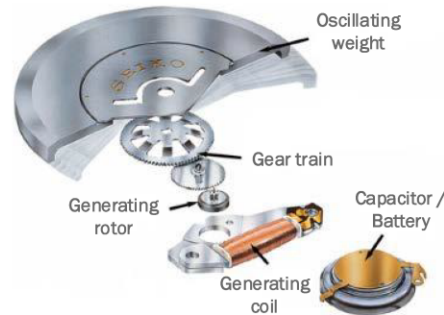


Figure 2. Exploded view of the energy generation unit in Seiko Kinetic watch⁹

Since the effective inertial torques contributed from the gears and the rotor are at least two orders of magnitude smaller than the one from the oscillating weight, we only augmented Equation (2) with the updated damping terms as follows.

$$I_G \ddot{\theta}_z = -I_G \dot{\phi}_z - D_{m1} \dot{\phi}_z - (D_{m2} + D_e) \eta_1 \eta_2 \dot{\phi}_z - \text{sgn}(\dot{\phi}_z) T_C + F_x l \sin \phi_z - F_y l \cos \phi_z \quad (4)$$

Where the parameters are listed in Table 1 and the power output is defined as

$$P = D_e \eta_1 \eta_2 \dot{\phi}_z^2 \quad (5)$$

Table 1. Parameters of the Seiko Kinetic Watch model

Component	Parameter	Value
Oscillating weight	Mass m	$4.7 \times 10^{-3} \text{ kg}$
	Moment of inertia about center of mass I_G	$2.5 \times 10^{-7} \text{ kg} \cdot \text{m}^2$
	Moment of inertia about rotating axis I_O	$3.25 \times 10^{-7} \text{ kg} \cdot \text{m}^2$
	Eccentricity l	$4 \times 10^{-3} \text{ m}$
Gear train	Oscillating weight wheel to intermediate wheel ratio η_1	1:76/7
	Intermediate wheel to generating rotor ratio η_2	1:61/7
Damper	Ball bearing viscous damping coefficient D_{m1}	$1.1 \times 10^{-7} \text{ N} \cdot \text{m} \cdot \text{s}$
	Lumped viscous damping coefficient D_{m2}	$2 \times 10^{-8} \text{ N} \cdot \text{m} \cdot \text{s}$
	Lumped Coulomb damping torque T_C	$2.2 \times 10^{-5} \text{ N} \cdot \text{m}$
	Electrical damping coefficient (with an optimal resistive load) D_e	$4 \times 10^{-7} \text{ N} \cdot \text{m} \cdot \text{s}$

3. DATA COLLECTION

3.1 Mobile data logging platform

We have developed a mobile data logging platform (Gen-1) to be worn on test subjects which can capture the 6 degree of freedom inertia data and the voltage outputs from the micro-generators simultaneously. As shown in Figure 3, this Arduino based platform consists of a 9 axis BNO055 inertial measurement unit (IMU) and an Adafruit data logging shield that records inertia data as well as the voltage output of a Seiko Kinetic at 50 Hz. An RC filter was used to obtain the voltage output from the Seiko Kinetic watch. Since we removed the actual power conditioning circuit in the watch, this circuit should match the simplified electrical damper model.

A miniaturized data logger (Gen-2) based on TinyDuino platform, shown in Figure 3 as well, can sample at a higher sampling rate of 800 Hz. Note that the data presented in this paper were collected using the Gen-1 platform. We will use the Gen-2 platform for future data collection to ensure minimal hindrance to the natural motion of test subjects.

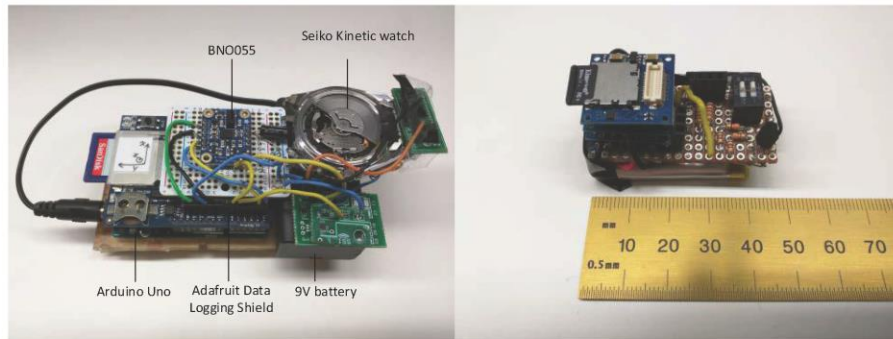


Figure 3. Photographs (not in the same scale) of the data logging platforms: Gen-1(left) and Gen-2(right).

3.2 Data collection procedure

Six subjects including both male and female participated in the data collection experiments. The data logger was attached to different body locations including the wrist, the upper arm, the chest, the waist and the upper leg using a cell phone band or bandages with Velcro. The dominant hand was chosen for attachment on the arm and the wrist. Details of the experimental set up are illustrated in Figure 4.

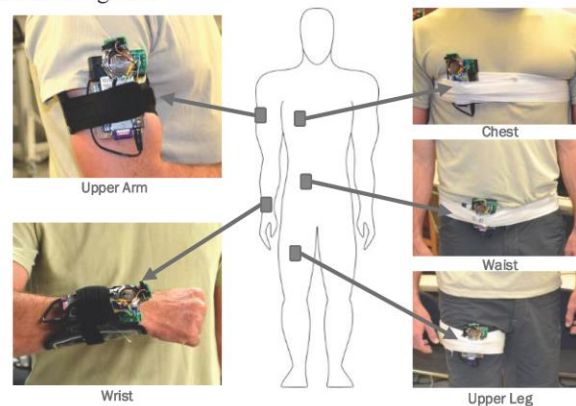


Figure 4. Photographs of the data logging platform on different body locations.

We asked all the subjects to conduct a series of daily activities including walking, jogging, running, web surfing and writing (the same text) on whiteboard. To obtain the most authentic data we specifically instructed the subjects to behave naturally and not to exaggerate the motion. Data were collected for one minute for each activity on each body location.

We have observed significant variation in activity level from subject to subject during the experiment, and thus a variation in the energy availability to harvest is expected.

4. ANALYSIS ON POWER OUTPUT

The generalized rotational harvester model provides an estimate of the maximum power output in an ideal scenario in which the electromechanical coupling can be closely approximated by an optimal linear viscous damper and mechanical damping losses (i.e. $D_m = 0$) and parasitic electrical losses are neglected. This may seem counterintuitive as assuming $D_m = 0$ in a linear vibration energy harvester would result in an optimal D_e of almost zero and infinite displacement. In our rotational case, however, there is no resonant effect as there is no restoring spring. Thus, in practice the optimal D_e is much higher than the implemented realistic D_m as observed in our simulation. Thus we take this approach to obtain the theoretical upper bound. Real-world constraints will certainly lower the actual maximum. The power output was found to be a function of the electrical damping coefficient and the eccentric rotor size. The theoretical maximum power output obtained at the optimal electrical damping coefficient at different body locations from different activities are given in Figures 5-9. The eccentric rotor applied in simulation is assumed to be made of brass with a 2mm thickness. The rotor radius ranges from 1.2 cm to 1.6 cm. Note that a small number of data are excluded in the post-processing due to an anomaly caused by an apparent motion artifact. The average power output measured from the Seiko Kinetic watch of all the subjects are marked as colored stars to match the activity with respect to its actual rotor inertia in Figures 5-9 as well. The actual power generated from web surfing and writing on whiteboard is minimal and thus not plotted.

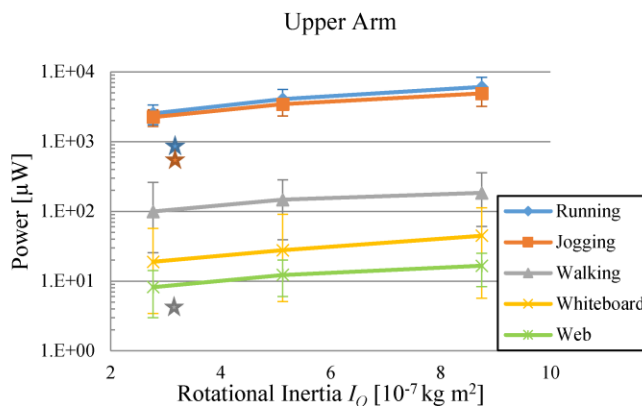


Figure 5. Average power upper bound from different activities taken at the upper arm location. The star marks the corresponding average measured power output from the Seiko Kinetic watch. The stars are color coded by activity.

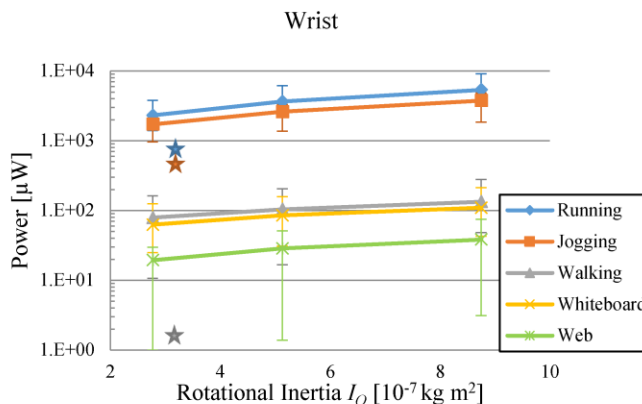


Figure 6. Average power upper bound from different activities taken at the wrist location. The star marks the corresponding average measured power output from the Seiko Kinetic watch. The stars are color coded by activity.

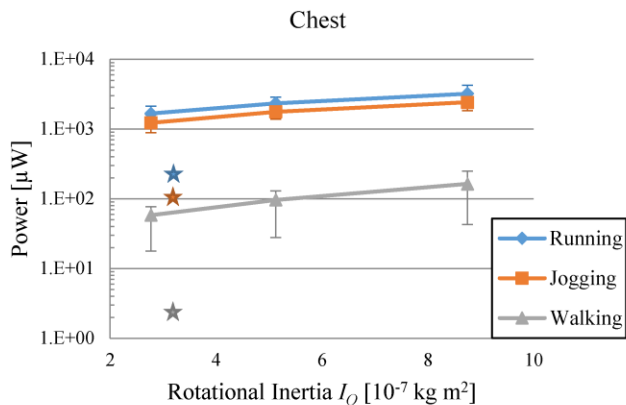


Figure 7. Average power upper bound from different activities taken at the chest location. The star marks the corresponding average measured power output from the Seiko Kinetic watch. The stars are color coded by activity.

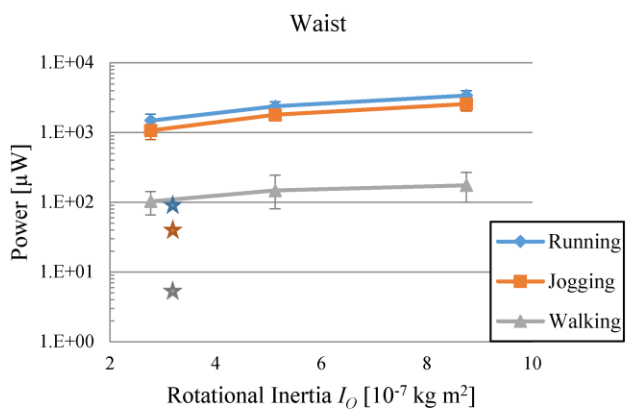


Figure 8. Average power upper bound from different activities taken at the waist location. The star marks the corresponding average measured power output from the Seiko Kinetic watch. The stars are color coded by activity.

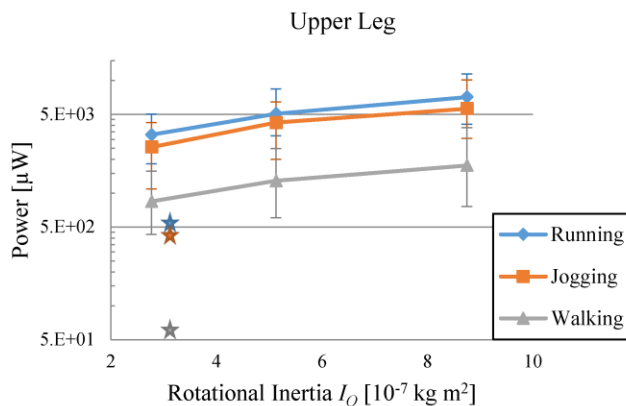


Figure 9. Average power upper bound from different activities taken at the upper leg location. The star marks the corresponding average measured power output from the Seiko Kinetic watch. The stars are color coded by activity.

As expected the power output scales with the intensity of the motion input at the same body location with running being the greatest and web surfing the least. Note that motions including web surfing and whiteboard writing involve little or no lower body motion thus the inertia data were only collected from the upper body locations. The variation in power output among different subjects, depicted as the error bar range, is in general smaller in vigorous activities such as running than in moderate activities such as walking. This agrees with the fact that the motion profile of human gait can be drastically different among the population, which is another challenge in designing a wearable energy harvester.

Additionally, these data demonstrate that a substantial gap between the theoretical maximum and what has been realized in commercial products exists. The gap among mild activities such as walking is more than one order of magnitude with the Seiko Kinetic producing less than $5 \mu\text{W}$ while the theoretical maximum is around $100 \mu\text{W}$ on the wrist. The discrepancy for more vigorous activities is smaller, but still significant. This corroborates the Coulomb damping assumption in the Seiko model, i.e. there is a static torque that the oscillating weight needs to overcome before producing power. The effect of this static torque becomes negligible when the motion is more intense.

As shown in Figure 10, the power output predicted by the Seiko Kinetic model agrees well with the measured data on an average basis given the real-world motion inputs to the nonlinear system. This system-level model allows us to identify optimizations by tuning the parameters. As a matter of fact, the power output improvement can be achieved by simply reducing the mechanical damping coefficient or the Coulomb damping torque in simulation. For example, a 24% improvement can be made by reducing the lumped damping (D_{m2} and T_c) terms by half, and a 48% improvement can be made by eliminating them in the case of the wrist location from running. In both of these cases, D_e , the electrically induced damping term, was left unchanged. If we allow the electromechanical transducer to be altered by choosing the optimal D_e , a three-time improvement can be achieved, which is close to the theoretical maximum with no friction at all. In terms of the mechanical damping itself the Coulomb damping contributes more to the mechanical loss than the viscous damping. The realization of a system with much lower mechanical damping (and an optimal level of electrically induced damping) will likely require a method of frequency up-conversion that fundamentally imposes less loss than a gear train and a high speed friction bearing.

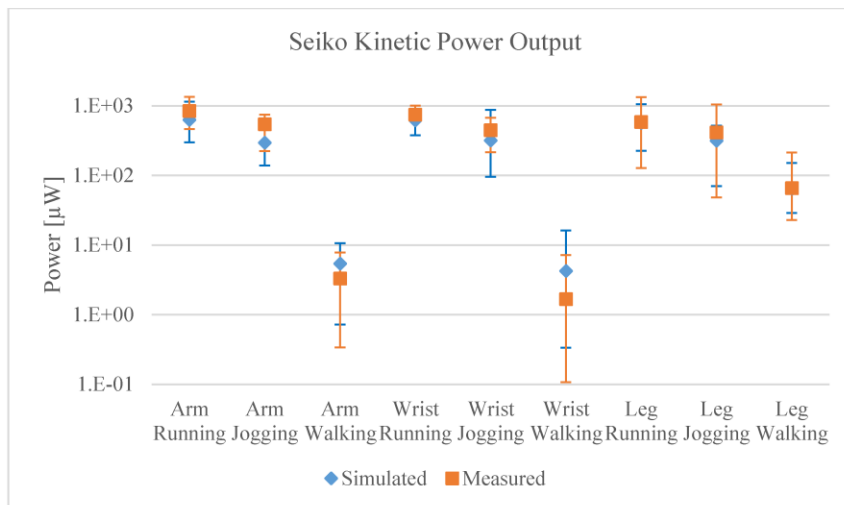


Figure 10. Average power output from the Seiko Kinetic watch: simulated vs. measured.

5. CONCLUSION

This paper has presented the characterization of the micro-generator embedded in the Seiko Kinetic watch based on a model augmented from the previously developed generalized rotational energy harvester model. We have developed a mobile data logging platform to collect power output from the Seiko Kinetic watch as well as six axis inertial data as the input to the simulation model at different body locations from multiple subjects for a series a daily activities. By comparing

the theoretical upper bound and what has been achieved through a commercial product, we have demonstrated the space for improvement on power generation. Finally we conclude that optimization could be made by tuning system parameters to increase the power output with examples of 24% to 48% improvement by reducing mechanical damping.

As an ongoing effort to collect authentic data from more represented subjects, we are upgrading the data logger platform with a higher sampling rate and a smaller form factor. We intend to apply the same modelling procedure to other COTS watch micro-generators and improve the model with the actual circuit components to allow us tune the system electrically. Most importantly we will need to experimentally realize the optimization in future work.

6. ACKNOWLEDGEMENT

This work was supported by the National Science Foundation ASSIST Nanosystems ERC under Award Number EEC-1160483.

REFERENCES

- [1] Galchev, T., Kim, H., Najafi, K., "Micro Power Generator for Harvesting Low-Frequency and Nonperiodic Vibrations," *J. Microelectromechanical Syst.* **20**(4), 852–866 (2011).
- [2] Pillatsch, P., Yeatman, E. M., Holmes, A. S., "A piezoelectric frequency up-converting energy harvester with rotating proof mass for human body applications," *Sensors Actuators A Phys.* **206**, 178–185 (2014).
- [3] Xue, T., Roundy, S., "Analysis of Magnetic Plucking Configurations for Frequency Up-Converting Harvesters," *J. Phys. Conf. Ser.* **660**, 012098 (2015).
- [4] Wang, J., Wang, W., Jewell, G. W., Howe, D., "Design of a miniature permanent-magnet generator and energy storage system," *IEEE Trans. Ind. Electron.* **52**(5), 1383–1390 (2005).
- [5] Lossec, M., Multon, B., Ahmed, H. Ben., "Micro-kinetic generator: Modeling, energy conversion optimization and design considerations," *MELECON 2010 - 2010 15th IEEE Mediterr. Electrotech. Conf.*, 1516–1521 (2010).
- [6] Kinetron., "Micro Generator System '26.4,'" <<http://www.kinetron.eu/wp-content/uploads/2015/01/MGS-26.4.pdf>> (21 February 2016).
- [7] Xue, T., Ma, X., Rahn, C., Roundy, S., "Analysis of Upper Bound Power Output for a Wrist-Worn Rotational Energy Harvester from Real-World Measured Inputs," *J. Phys. Conf. Ser.* **557**, 012090 (2014).
- [8] Mitcheson, P. D., Green, T. C., Yeatman, E. M., Holmes, A. S., "Architectures for Vibration-Driven Micropower Generators," *J. Microelectromechanical Syst.* **13**(3), 1–12 (2004).
- [9] "Kinetic | Our clean energy watches | SEIKO WATCH CORPORATION.," <<http://www.seiko-cleanenergy.com/watches/kinetic-1.html>> (21 February 2016).

CHAPTER 3

CHARACTERIZATION OF MICROGENERATORS IN COMMERCIAL MOTION POWERED QUARTZ WATCHES: PART II, KINETRON MGS

This chapter is a journal manuscript that has been submitted to *IEEE/ASME Transactions on Mechatronics* and is currently under review.

3.1 Introduction

Energy harvesting for wearable applications has gained significant traction in recent years. It provides a promising alternative to conventional batteries when energy independence is preferred or even necessary. Feasible applications include wearable health monitors and implantable sensors [1]. A major obstacle to harvesting energy in a wearable fashion is the unpredictable nature of the human motion, which is dominated by nonperiodic and low-frequency quasiperiodic excitations. A technique coined as frequency up-conversion is often applied in the research communities to efficiently utilize higher frequency resonant harvesters with a low-frequency, nonperiodic environmental input [2–4]. In the commercial space, however, motion-powered quartz watches have achieved effective frequency up-conversion by different means, often with the involvement of gear trains. In many cases, reported wearable energy harvesting prototypes utilize an eccentrically weighted rotational proof mass [3,5–7] as it can be excited in all directions with no inherent motion limit. The harvesters often resemble the shape of a wrist-worn watch.

Motion-powered quartz watches, sometimes also referred to as automatic quartz, are successful demonstrations of energy harvesting techniques for commercial wearable applications. Examples of these include Seiko Kinetic, Citizen Eco-Drive Duo, and Swatch Autoquartz, which uses the Micro Generator System (MGS) made by Kinetron as the energy generation unit. Although the latter two have been discontinued, the first is still in production. These motion-powered watches are often overlooked in the wearable energy harvesting literature largely because they are developed empirically (i.e., without the use of predictive modeling) and in the commercial space, yet they are ideal candidates against

which to benchmark for many research endeavors in wearable energy harvesting. Some existing characterization work exists in the literature where the system is often analyzed in isolation without any rotor kinematics or real-world input [8,9]. Seiko only provides vague descriptions for its power capabilities in the user manual [10] whereas Kinetron claims 600 mJ per day from the MGS [11]. A reasonable estimate of power output is roughly $5 \mu\text{W}$ on a daily average basis for these watches [12]. An 8-hour measurement for the Seiko Kinetic reports a median power of $0.5 \mu\text{W}$ among subjects [13]. Another full-day measurement for the Kinetron MGS reports a total energy generation of 1.1 J [14]. However, for benchmarking purposes, there is a lack of knowledge in terms of power output with respect to specific excitations. In addition, to understand the potential and limitations of these motion-powered watches for wearable energy harvesting better, a thorough model-based characterization is indispensable.

We have characterized the microgenerator embedded in the Seiko Kinetic watch in a previous work [15] based on a generalized rotational harvester model [16]. The Seiko Kinetic watch employs a sophisticated gear train with a 1: 100 ratio to increase the velocity of the rotating magnetic rotor and thus the effective electromechanical coupling, which also ensures an appropriate voltage output for power conditioning. However, this high gear ratio is also reflected on the viscous damping associated with the bearings and reduces the available maximal energy for harvesting [16]. Given the higher damping on the rotational mass that results from the high-ratio gear train, alternative frequency up-conversion techniques might be required to achieve the improved power output that we see in simulation with reduced mechanical damping [15]. Unlike the Seiko Kinetic, the Kinetron MGS decouples its transducer from the rotational mass with a spring as an intermediate

energy storage element. To our knowledge, a full model-based characterization of Kinetrone MGS has never been published in the literature. The characterization includes both bench-top and human subject experiments on power generation, which will shed light on the state of the art in commercial wearable energy harvesting capabilities. In addition, we will study the scaling laws with respect to power output and explore pathways to improved power output in simulation-based studies.

3.2 Modeling

3.2.1 Generalized Rotational Energy Harvester Model

The characterization of Kinetrone MGS is based on the previously developed generalized rotational harvester model [16]. The model predicts an upper bound on energy generation given the 6-axis motion inputs and system constraints such as the rotational inertia and the eccentricity of the eccentric proof mass. An electrical and a mechanical rotational viscous damper, namely b_e and b_m , are applied to the rotational proof mass to represent extracted and lost energy, respectively. This model is an analogy to the linear velocity damped resonant generator (VDRG) model [17,18], making the assumption that the power dissipated through an optimal viscous damper that represents the electromechanical transducer is the maximum electrical power that can be extracted from the system. This hypothesis has only been proven for linear oscillators under periodic base excitations. For rotational architectures with quasiperiodic or even chaotic excitations such as real-world human motion, we believe a reasonable estimate of the maximum achievable power can be derived based upon this assumption nonetheless. In theory, all eccentric-rotor-based energy harvesters including both the Seiko Kinetic and the Kinetrone MGS

should be limited by the predicted upper bound on power output.

The 3-dimensional model accounts for 5 axis inertial inputs (there is no \ddot{Z}) as the harvester can be excited with linear excitations, rotational excitations, or both. As illustrated in Fig. 3.1, the model can be reduced into 2 dimensions as the rotation of the eccentric mass is constrained in the XY plane. Applying Newton's second law to this lumped model, we have

$$m\ddot{\mathbf{r}} = \mathbf{F}_h + m\mathbf{g} \quad (3.1)$$

$$I\ddot{\psi}_z = -(b_m + b_e)\dot{\phi}_z + (-\mathbf{L}) \times \mathbf{F}_h \quad (3.2)$$

where the torques are summed at the rotor center of mass. m , I , and \mathbf{L} are the mass, the moment of inertia and the eccentricity vector of the rotor (its amplitude is denoted L), respectively. \mathbf{F}_h and \mathbf{g} are the forces from the housing via the supporting shaft and the gravitational acceleration, respectively. \mathbf{r} and ψ_z denote the absolute linear and angular displacement of the rotor whereas ϕ_z denotes its relative angular displacement with respect to the housing. The governing equation of the system [5] is derived as

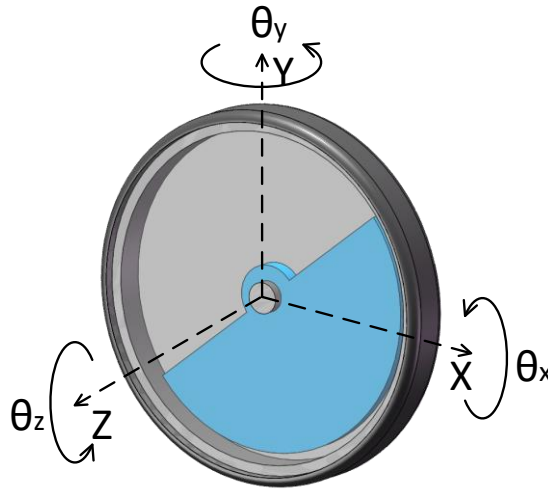


Figure 3.1. A generalized eccentric-rotor-based rotational energy harvester.

$$\ddot{\phi}_z = \frac{-(b_m + b_e)\dot{\phi}_z + mL[(\ddot{X} - g_x) \sin \phi_z - (\ddot{Y} - g_y) \cos \phi_z]}{I + mL^2} - \ddot{\theta}_z \quad (3.3)$$

where \ddot{X} , \ddot{Y} , and $\ddot{\theta}_z$ are the linear and rotational acceleration inputs to the system. Conveniently the combination of the linear accelerations and the negative gravitational accelerations are usually the raw accelerometer output, which can be obtained alongside the rotational velocity from an inertial measurement unit (IMU). The power output for this viscously damped generalized harvester model is determined by:

$$P = b_e \dot{\phi}_z^2 \quad (3.4)$$

The full derivation of the model is given in the appendix.

3.2.2 Kinetron MGS Model

As illustrated in Fig. 3.2 [11], the Kinetron MGS utilizes the oscillating weight to capture the inertial energy from human motion. The bidirectional rotation of the oscillating weight is converted to the unidirectional winding of a spiral spring through a mechanical

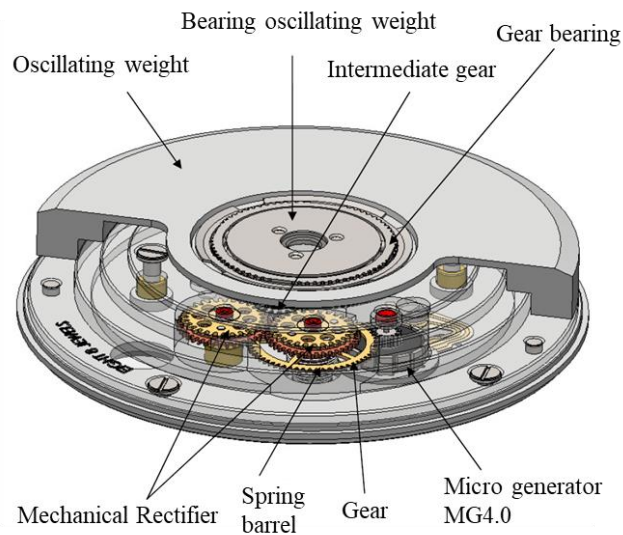


Figure 3.2. Components of the Kinetron Micro Generator System (MGS).

rectifier, which consists of two ratchet wheels. The rectifier imposes a backlash deadband of approximately 10 degrees when the oscillating weight switches direction and a new rectification is initiated. The upper extremity of the spring is tied to the end of the mechanical rectifier and the lower extremity is fastened to a gear that turns the microgenerator at a ratio of 1 to 5. An exploded view of the microgenerator is given in Fig. 3.3 [19]. The generator comprises a 14-pole magnet as the generating rotor and a claw-pole stator. As the spring restoring torque builds up, the generating rotor is held by the detent (or cogging) torque induced by the claw structure of the stator until the restoring torque surpasses the maximum detent torque. Then a sudden spring jump occurs and turns the generating rotor at a high speed, which induces changes of magnetic flux through the coil and thus electricity. The spring functions as an intermediate energy storage element and the generator itself is highly decoupled from the characteristics of the environmental excitation. However, under extreme conditions when the oscillating weight moves sufficiently fast, the spring degenerates to a fixed connection.

The entire MGS can be viewed as an intermittently coupled system between the oscillating weight structure and the microgenerator depending on the state of the

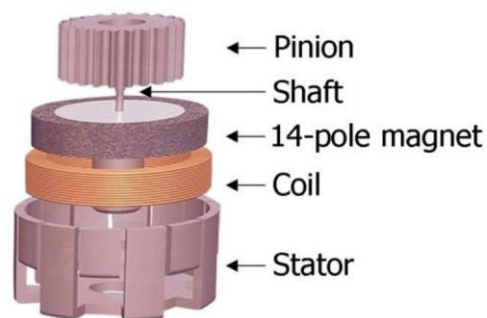


Figure 3.3. Components of microgenerator MG4.0.

mechanical rectifier. Hence, we can initially model two subsystems individually. When the rectifier operates in the deadband and the spring is disengaged, the governing equation for the oscillating weight is identical to Eq. (3.3) with the absence of the electrical damper (i.e., the microgenerator in this case). It will be shown later that a hybrid damping mechanism with a Coulomb damping torque, T_c , in addition to the viscous damper better represents the frictional energy loss associated with the jewel bearings and the gear transmission.

$$\ddot{\phi}_z = \frac{-b_m \dot{\phi}_z - T_c \text{sgn}(\dot{\phi}_z) + mL[(\ddot{X} - g_x) \sin \phi_z - (\ddot{Y} - g_y) \cos \phi_z]}{I + mL^2} - \ddot{\theta}_z \quad (3.5)$$

On the other hand, when not operating in the deadband, the state of the microgenerator is determined by the summation of the torques applied including the spring restoring torque T_k , the electromagnetic torque T_{em} , the viscous damping torque T_f , and the detent torque T_d .

$$\ddot{\alpha} = \frac{T_k + T_{em} + T_f + T_d}{I_{gt}} \quad (3.6)$$

where I_{gt} is the moment of inertia of the generating rotor (i.e., the 14-pole magnet) and we use α to denote its angular displacement. Accordingly, the flux linkage is determined by the maximum magnetic flux Φ_{max} and the phase of the generating rotor.

$$\Phi_f(\alpha) = \Phi_{max} \cos(p\alpha) \quad (3.7)$$

In the equation above, p denotes the number of pole pairs. The instantaneous electromagnetic torque T_{em} is the product of the armature current i and the derivative of the flux linkage with respect to the generator angle.

$$T_{em} = i \frac{d\Phi_f}{d\alpha} = -\frac{1}{R_c + R_l} \frac{d\Phi_f}{dt} \frac{d\Phi_f}{d\alpha} \quad (3.8)$$

where R_c and R_l are the resistance of the coil and the load, respectively. Note that for characterization purposes, we terminate the coil with a resistive load whereas in the original

MGS system, the voltage output is rectified and stored in a lithium-ion battery. In addition, the inductance of the coil is neglected. The restoring torque of the spiral spring is defined by the difference between the two extremities and the spring stiffness k . In addition, the torque applied to the generator is geared down by a ratio of η_2 .

$$T_k = \eta_2(\beta - \eta_2\alpha)k \quad (3.9)$$

Here we use β to denote the lower extremity angle, which is the output of the mechanical rectifier. When the rectifier overcomes the slippage angle and engages the spring, this lower extremity angle tracks the absolute value of the relative angular displacement of the oscillating weight ϕ_z accumulatively and with a gear up ratio of η_1 . We assign b_{gt} as the viscous damping coefficient for the generating rotor, and thus obtain the damping torque as

$$T_f = -b_{gt}\dot{\alpha} \quad (3.10)$$

The detent torque is a well-known phenomenon that exists in all claw-pole motors that use permanent magnets. It is the result of a tendency of the rotor to stay in a particular position with respect to the claw of the stator where the permeance of the magnetic circuit is maximized. Although an undesirable byproduct in most applications, the detent torque is indispensable to the functionality of the microgenerator in this case. It allows the spring to accumulate energy and release it at a higher frequency with proper voltage output. In general, electromagnetic generators suffer from low voltage output when the mass velocity is slow. It has been shown that an analytical solution for the detent torque can be derived with the knowledge of the detailed geometry of the stator [20], in the absence of which, however, we can approximate its profile as a sinusoidal function with respect to the phase given that the maximum torque can be experimentally obtained [9].

$$T_d = -T_{dmax} \sin(2p\alpha) \quad (3.11)$$

Substitute (8)-(11) into (6), we have

$$\ddot{\alpha} = -\frac{\left(b_{gt} + \frac{p^2 \Phi_{max}^2 \sin^2(p\alpha)}{R_c + R_l}\right) \dot{\alpha} + \eta_2^2 k \alpha + T_D \sin(2p\alpha) - \beta \eta_2 k}{I_{gt}} \quad (3.12)$$

When the mechanical rectifier operates out of the deadband, the spring is engaged and its restoring torque is reflected on the oscillating weight via the associated gear train.

As a result, the governing equation for the oscillating weight structure is modified as

$$\ddot{\phi}_z = \frac{-b_m \dot{\phi}_z - T_c \operatorname{sgn}(\dot{\phi}_z) - \frac{T_k}{\eta_1 \eta_2} + mL[(\ddot{X} - g_x) \sin \phi_z - (\ddot{Y} - g_y) \cos \phi_z]}{I + mL^2} - \ddot{\theta}_z \quad (3.13)$$

Finally, the power output across a resistive load is given by

$$P = R_l \left(\frac{1}{R_c + R_l} \frac{d\Phi_f}{dt} \right)^2 \quad (3.14)$$

We implement the Kinetron MGS model using Eq. (5)-(13) in Matlab with the parameters listed in Table 3.1 [9,11,19,21] and carry out the simulation in the time domain using a numerical ordinary differential equation (ODE) solver. In order to obtain an

Table 3.1. Parameters for the Kinetron MGS model

Component	Parameter	Value
Oscillating weight	Mass m	4.0×10^{-3} kg
	Moment of inertia about center of mass I	2.6×10^{-7} kg · m ²
	Eccentricity L	6.6×10^{-3} m
Generating rotor	Moment of inertia about center of mass I_{gt}	5.5×10^{-11} kg · m ²
	Number of pole pairs p	7
	Maximum flux linkage Φ_{max}	7.0×10^{-3} V · s
	Maximum detent torque T_{dmax}	1.1×10^{-5} N · m
	Coil resistance R_c	3.2×10^2 Ω
Gear train	Oscillating weight to spring ratio η_1	28:45
	Spring to microgenerator ratio η_2	12:60

accurate numerical solution, integrations are restarted at the instances of discontinuity, primarily due to the mechanical rectifier (this is done by two ODE events and a switch-case loop to alternate between (5) and (13) as the governing equation of the oscillating weight based on the state of rectification). The inclusion of Coulomb damping escalates the computational cost at a fixed local error tolerance.

3.3 Data Collection

We divided our experimental characterization into two parts: bench-top and human-subject characterization. On one hand, controllable and repeatable bench-top tests provide convenience for model corroboration. On the other hand, on-body tests are essential for any wearable device because they grant insight into the performance and its variation among the population.

3.3.1 Bench-top Data Collection

In the literature, the bench-top characterization of wearable energy harvester prototypes was carried out by conventional linear shaking systems in many cases [3,22]. Particularly for rotational architectures, a direct rotational input to the rotor itself was sometimes applied, which decouples the energy harvester from the inertial dynamics [7,9]. We adopted a previously developed driven pendulum test set-up [5,23] to carry out the bench-top tests for the Kinetron MGS. Driven by a microstepping-enabled stepper motor, the pendulum arm shown in Fig. 3.4 creates a sinusoidal trajectory at a variety of frequencies (0.8, 0.91, 1.1, and 1.25 Hz) and amplitudes (12.5, 18, and 25 degrees). We chose these values to resemble upper limb motion in gait profiles ranging from casual to

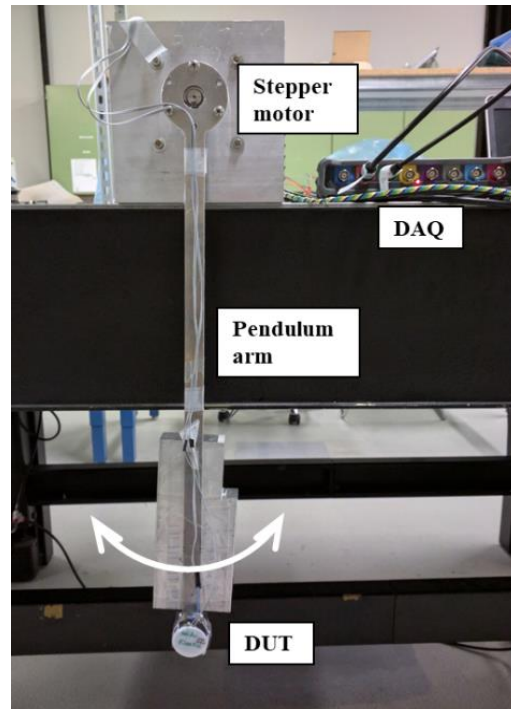


Figure 3.4. Photo of the pendulum arm test set-up.

vigorous walking [23]. This artificial quasiperiodic input roughly resembles a human arm in locomotion with the capability to provide rotational excitation in addition to linear accelerations.

The device under test (DUT) was attached at the end of the 50-cm long aluminum arm. The Kinetron MGS was terminated with a resistive load to extract energy from the system. Due to the pulsed nature of the energy generation, we experimentally determine the optimal load by measuring the energy generated per spring jump with a sweep of the resistive load. The optimal load was found to be larger than the coil resistance, which is likely due to the inductive effect and the additional mechanical impedance. However, there was significant inconsistency in terms of power generation per pulse with the same load resistance. This is possibly due to imbalances or asymmetry as a result of manufacturing

imperfections. (i.e., The maximum detent torque may depend on the resting position of the magnetic rotor.) In addition, the impedance of mechanical components is nonlinear in nature and dependent on the inertial input (including inertial conditions). We have identified a range of load resistance from approximately 500Ω to 1500Ω where the energy generation per pulse is nearly optimal. On average, the expectation of power output from a single spring jump is about $90 \mu\text{J}$.

3.3.2 Human Subject Data Collection

Thirty human subjects including 15 males and 15 females aged between 21 and 45 participated in our data collection. Among the test subjects, 26 are right-handed. Six degree of freedom inertial data from both wrists and the upper arm were recorded using a Shimmer3 IMU made by Shimmer sensing [24] at 50 Hz. These inertial data will serve as the input for model corroboration. As shown in Fig. 3.5, the IMU was placed directly on top of the Kinetron MGS, which is wrapped to the subject's wrist with an elastic bandage. Due to this arrangement, the inertial data collected by the IMU are not exactly the same as experienced by the Kinetron MGS. The power output from the MGS across a resistive load was recorded simultaneously using a USB PC oscilloscope made by Pico Technology at 1 MHz to surpass the Nyquist frequency. Test subjects wearing the IMU and the Kinetron MGS were instructed to conduct a series of activities involving upper limb movement including exercising on a treadmill, writing on a whiteboard, and office routines. Details of the tasks are explained in Table 3.2. The choice of a treadmill over simply walking or jogging on the ground is primarily due to its ability to control the velocity for consistency. Although differences exist, the overall gait parameters and kinematic patterns are similar

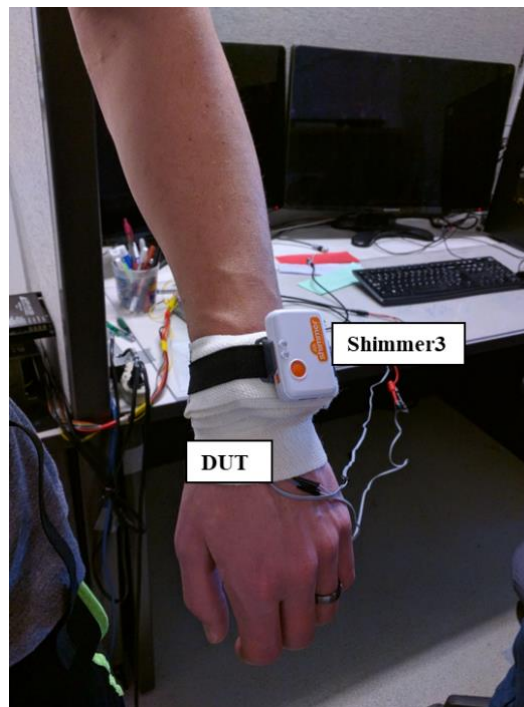


Figure 3.5. Photo of the human subject data collection set-up.

Table 3.2. Real-world characterization tests

Tasks		Description
Exercising on a treadmill	Slow walking	Velocity set as 2.5 mph, 2 minutes
	Fast walking	Velocity set as 3.5 mph, 2 minutes
	Jogging	Velocity set as 5.5 mph, 2 minutes
Office routines		Filing documents and serving coffee (repeat with both hands), time varies
Writing on a whiteboard		Writing the text “The quick brown fox jumps over the lazy dog” with the dominant hand, 1 minute

between walking on a treadmill and the ground [25]. However, we have observed a significant variation in the overall motion profile from subject to subject during the data collection process, which manifests as a large variation in energy availability among the population.

3.4 Simulation and Experimental Results

3.4.1 Transducer Model Validation

First, we characterize the microgenerator embedded in the Kinetron MGS as a standalone transducer. A no-load simulation of the electromotive force was presented in [9] to reveal its impulsive nature, yet no experimental validation was provided due to a lack of direct access to the electrical output. In this study, we used MGS samples provided by Kinetron with built-in access to the output from the microgenerator. Fig. 3.6 illustrates

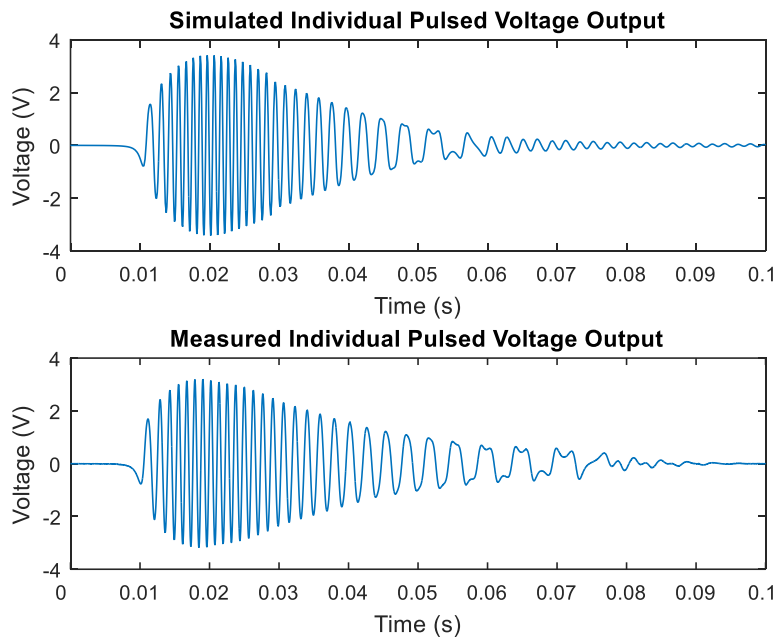


Figure 3.6. Simulated and measured pulsed voltage output from Kinetron MGS.

a comparison between simulated and measured voltage output with a resistive load of $1200\ \Omega$ from an individual spring release, which demonstrates good agreement in terms of both frequency and amplitude. However, the viscous damper assumption for the microgenerator model is not able to recreate the nonlinear time-varying damping pattern that exists in the later decay. A closer match is possible with a more complex damping model but it significantly increases the computation cost. This discrepancy can be neglected nonetheless due to the fact that the overall power output is dominated by the initial oscillations.

In addition, the model is able to recreate a phenomenon named extended jump when the oscillating mass moves sufficiently fast that the initial jump is overlaid with a second degenerated jump. Fig. 3.7 gives examples of this phenomenon in both simulation and measurement that resemble each other.

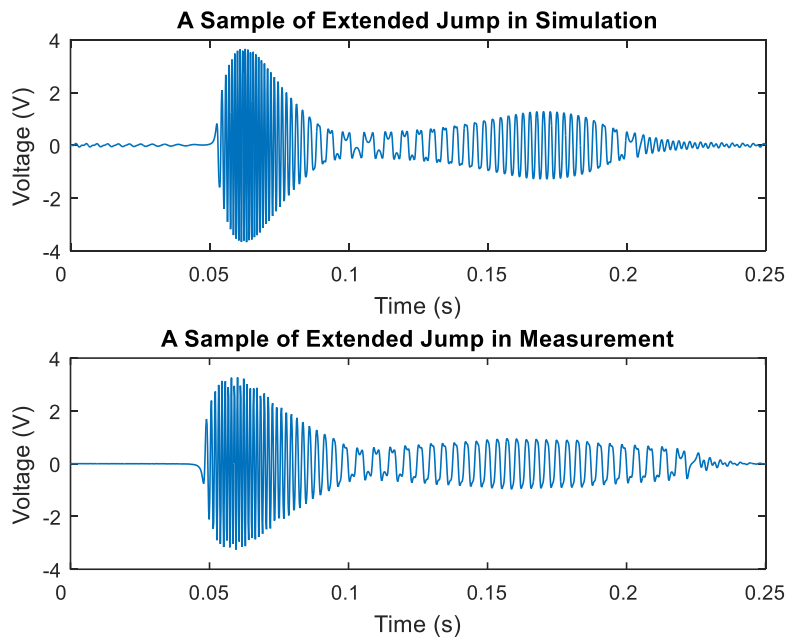


Figure 3.7. Extended jumps from Kientron MGS in simulation and measurement.

3.4.2 Bench-top Characterization

We arbitrarily chose two resistance values (550 Ω and 1200 Ω) towards both ends of the optimal range mentioned earlier as the load resistances for characterization. As shown in Fig. 3.8, a positive correlation exists between the power output and the excitation intensity (i.e., both amplitude and frequency). Each data point is obtained from a 40-second actuation. By our observation, 0.91 Hz exhibits a borderline case in which an individual pulse of energy is only occasionally and inconsistently generated. We denoted those power outputs as zero. Although the power output with the two load resistances are nearly identical, it appears that a 1200 Ω resistor extracts slightly more power. However, this is not a conclusive observation due to the inconsistent initial and the terminal conditions (i.e., the unknown amount of energy stored in the spring). The discrete nature of the power output profile increases the difficulty of eliminating the effect of residual spring energy at weak excitations. Nevertheless, the bench-top swing arm tests provide several data points with good enough repeatability for us to determine the damping parameters for the oscillating weight via trial-and-error data fitting.

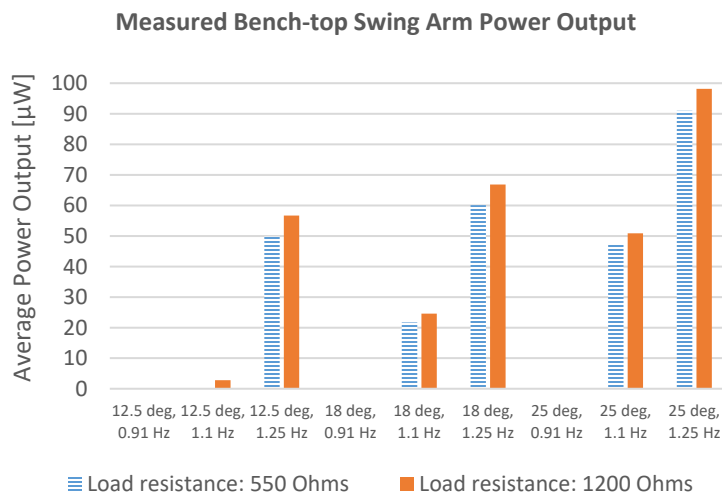


Figure 3.8. Measured bench-top swing arm power output from Kinetron MGS.

Fig. 3.9 illustrates the parametric fitting result with two damping models for the case with a 1200 Ω resistive load. For the purely viscously damped model, the rotational damping coefficient b_m is $3e-5$ Nms, whereas in the hybrid mode, b_m is $1.5e-6$ Nms and the Coulomb torque T_c is $7.5e-5$ Nm. Evidently, the inclusion of a Coulomb damper improves the match by imposing a static torque that prevents the oscillating weight from moving at weak excitations. Thus, the Kinetron MGS produces no power, which is in corroboration of the measured data. The viscous damper only model creates a linear power scaling with no cutoff frequency, which tends to overpredict power output at weak excitations.

3.4.3 Human Subject Test Results

Similar to the bench-top test, we divided 30 subjects into 2 groups of 15 to equip with either a 550 Ω or a 1200 Ω load resistance. Among each group, subjects are sorted

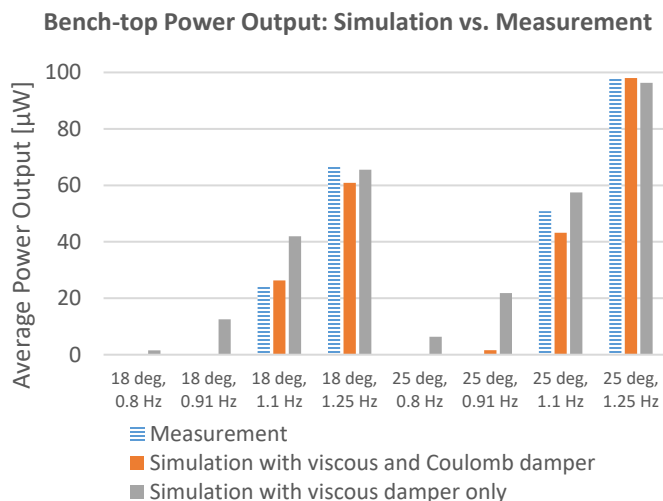


Figure 3.9. Simulated and measured bench-top swing arm power output from Kinetron MGS with a 1200 Ω resistive load.

into 3 equally numbered subgroups for the devices to be worn on the left wrist, the right wrist, and the upper arm, respectively. Fig. 3.10 to Fig. 3.13 illustrate all the measured power output along with the simulated results using the corresponding IMU data. For the wrist data with 10 subjects, we report the average power output, whereas for the upper arm data with 5 subjects, we use the median power output due to a more dominant effect of outliers in a smaller sample size. The error bars depict the range of power output among the subjects.

The different resistive loads do not result in significantly different power output. (Statistical significance tests indicate that there is no significant difference in power output between tests performed with $550\ \Omega$ and $1200\ \Omega$ load resistances for 3.5 mph, 5.5 mph, office routing, or writing. P-values from t-tests range from 0.24 to 0.91.) Jogging at 5.5 mph results in the most consistent power output whereas other activities, especially walking at 2.5 and 3.5 mph, result in significant variation. This agrees with the large

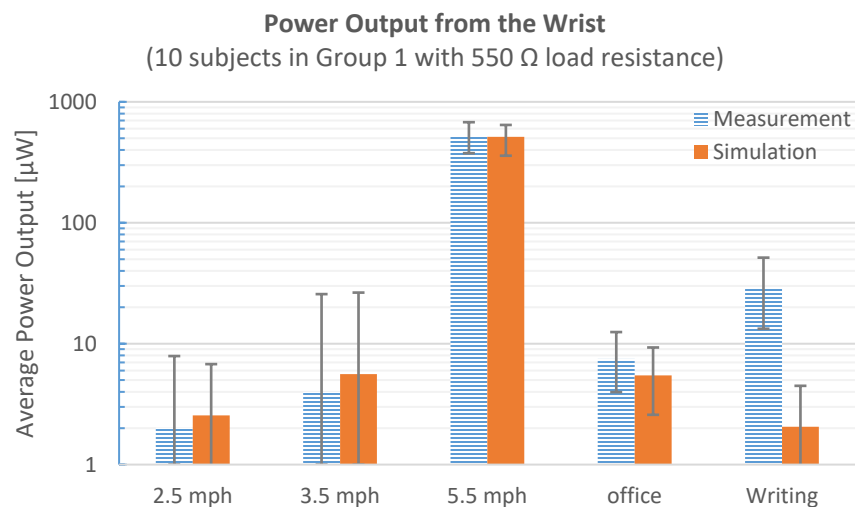


Figure 3.10. Measured and simulated power output from Kinetron MGS on the wrist with a $550\ \Omega$ resistive load (Group 1).

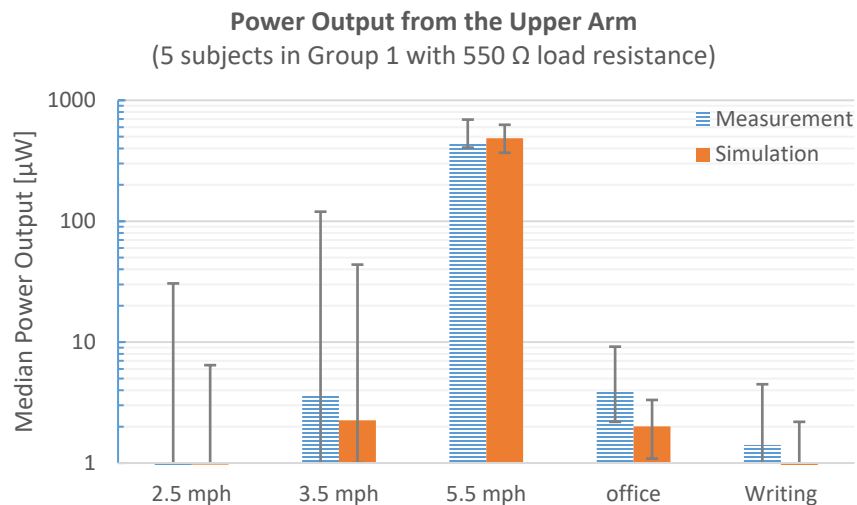


Figure 3.11. Measured and simulated power output from Kinetron MGS on the upper arm with a 550 Ω resistive load (Group 1).

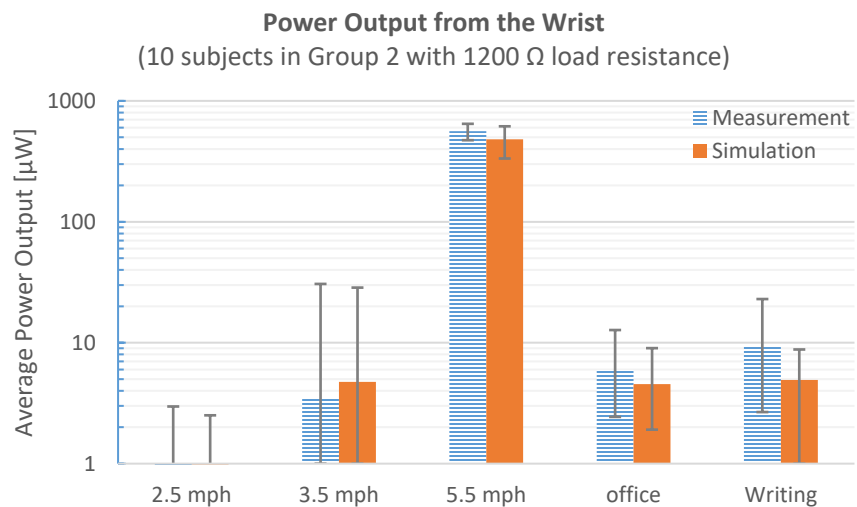


Figure 3.12. Measured and simulated power output from Kinetron MGS on the wrist with a 1200 Ω resistive load (Group 2).

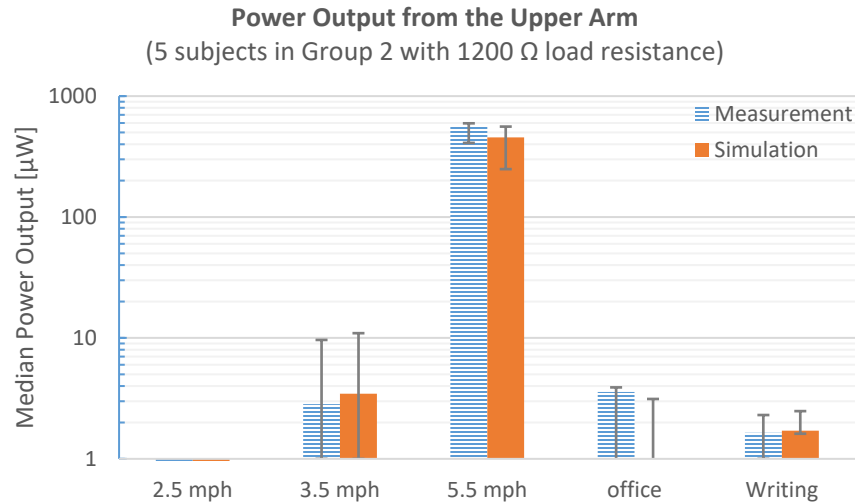


Figure 3.13. Measured and simulated power output from Kinetron MGS on the upper arm with a 1200 Ω resistive load (Group 2).

variability in gait pattern, particularly in walking, among subjects from our observation. Some subjects walk with minimal upper limb motion, which generates no power at all. Thus, the average power output could be dominated by a few outliers even though the majority is zero. This is reflected in the IMU data as well. Quantitatively, the amplitude of linear accelerations in X and Y direction (raw accelerometer output) at the dominant frequency is in general below 2 m/s^2 for walking at both 2.5 and 3.5 mph with a significant variation (extremities are 0.2 and 3 m/s^2). For jogging at 5.5 mph, the acceleration amplitude can go beyond 10 m/s^2 . Compared to the wrist, the upper arm location performs equally well in treadmill activities but generates lower power from the office routine and writing on a whiteboard due to a relatively still motion profile especially in writing. The wrist exhibits a larger range of motion that often goes through a significant change in its orientation with respect to the gravitational field, but, overall both the wrist and the upper arm are promising location candidates for inertial energy extraction to power wearables.

The simulated power output is in good agreement with the measured data in most

cases in terms of both the average and the variation of power output. However, the predictability deteriorates as the input becomes less energetic and irregular, which resembles the borderline cases in the bench-top swing arm tests. There is some error induced due to the fact that the IMU is placed on top of the Kinetron MGS, and therefore experiences a slightly different excitation. The elastic bandage could also add to this inaccuracy. In addition, the model itself lacks some accuracy due to the approximated damping parameters obtained from a manual data fitting. The nonlinearity and discontinuity in the model accelerates the error accumulation in the numerical solver as well. Nevertheless, the model appears sufficient to predict power output on an average basis when the effect of initial conditions is eliminated and thus will be used for further investigation.

3.5 Design Considerations

An overall impression from the human subject test results is that the Kinetron MGS performs relatively well in jogging with approximately $500 \mu\text{W}$ output on average, whereas in walking, it suffers from zero power output from many subjects. What happens in those scenarios is that the device is trapped in the rectification deadband. This is one limiting factor of the design, which imposes an excitation threshold for the microgenerator to function. Given how much mild activities occupy in a normal daily routine, this may affect the power capability of the Kinetron MGS for a less energetic population as a wearable energy harvester. To illustrate this, we simulate the power output with hypothetical smaller deadband angles using collected inertial data samples from the wrist. As shown in Fig. 3.14, there is a trend of increasing power output for walking at both 2.5 and 3.5 mph

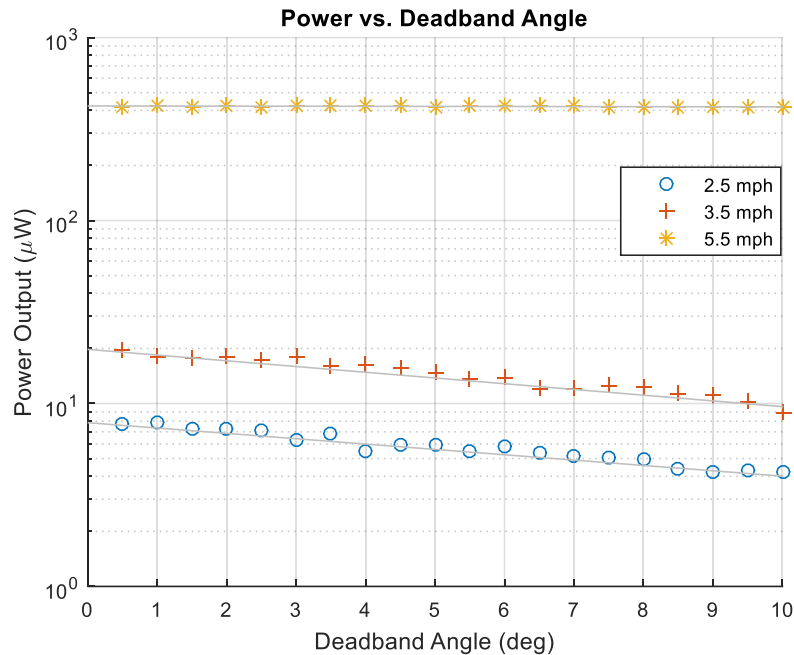


Figure 3.14. Simulated power output using sample treadmill inertial data as a function of the mechanical rectifier deadband angle.

with decreasing deadband angles. However, it appears that the deadband angle has no apparent effect when the input becomes as vigorous as jogging at 5.5 mph. Under this scenario, the limiting factor becomes the viscous frictional damping due to a higher proof mass velocity. Nevertheless, the elimination of the mechanical rectifier is a potential improvement for the device, which may require an alternative mechanism to engage the spring with the oscillating weight.

The Kinetron MGS was originally designed to be in the shape of a wrist-worn watch. In other applications, with a different form factor or body location, the geometry of the rotor can be altered in the allowed design space to fully capture the available inertial energy. This is another optimization opportunity. In Fig. 3.15, we use least square regression to illustrate the scaling relationship between the sizing and the power capability with the same inertial inputs used in Fig. 3.14. We multiply the radius of the oscillating

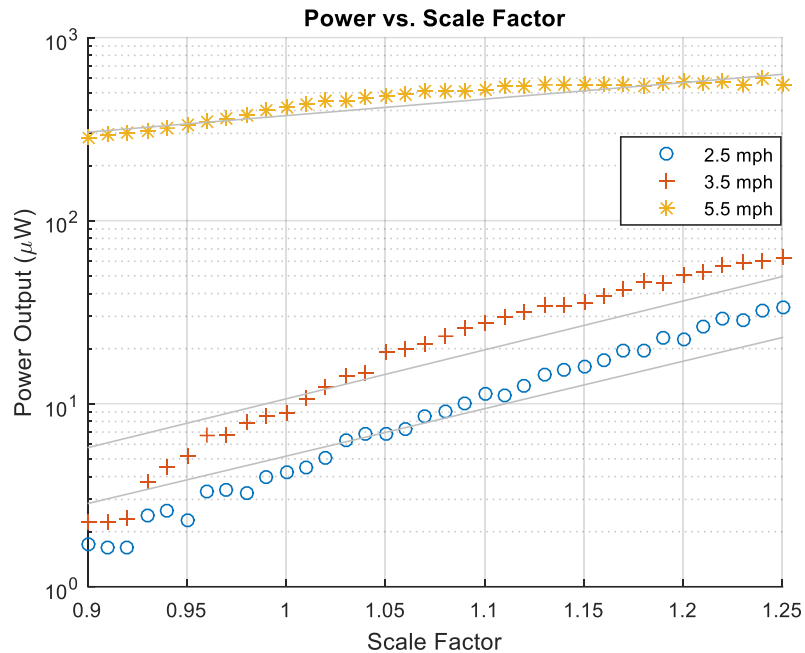


Figure 3.15. Simulated power output using sample treadmill inertial data as a function of the scale function.

weight by a scale factor while maintaining the same thickness. Note that we keep the same microgenerator parameters for simplicity although there is potential room for optimization with multiple degrees of freedom for a given oscillating weight geometry. In general, a larger design space creates more available power for most activities. The potential improvement appears to be dependent on the excitation as well. Particularly for walking at 2.5 and 3.5 mph, a 10% increase in radius doubles the power output. Theoretically, more electromechanical coupling can be introduced to further increase the power output when a larger proof mass is available, which can be either implemented in the design of the microgenerator itself or the power conditioning circuitry.

3.6 Conclusion

This paper has presented the characterization of the Kinetron MGS, one example of the generators used in motion-powered quartz watches. We derived a system-level model that links the power output directly to the environmental input with a mathematical representation of both the rotor kinematics and the transducer dynamics. We characterized the Kinetron MGS using both repeatable mechanical swing arm tests and human subject tests. The bench-top results are useful for potential benchmarking and model validation. The real-world performance evaluation provides a state-of-art characterization for commercial wearable energy harvesting capabilities. The model achieves good predictive capability for long-term average power output, especially for vigorous activities.

Through numerical simulations, we found potential improvement with a reduced rectification deadband for less vigorous activities. This, however, may require an alternative design to link the proof mass rotation to the spiral spring. Furthermore, we used the modal to evaluate the scaling relationship between the sizing and the power output to investigate the power capabilities for other potential applications. In general, power scales with the rotor radius and the scaling is dependent on the input. In particular, the power output doubles with a 10 % increase in rotor radius for walking at 2.5 and 3.5 mph.

3.7 Appendix

In this discussion, the directional subscripts for rotational variables are dropped since the problem is constrained in the local $X_I Y_I$ wrist plane (see Fig. 3.16). The absolute acceleration of the rotor can be expressed as

$$\mathbf{a}_{abs} = \ddot{\mathbf{x}} = \mathbf{a}_{ref} + \ddot{\boldsymbol{\theta}} \times \mathbf{L} + \dot{\boldsymbol{\theta}} \times (\dot{\boldsymbol{\theta}} \times \mathbf{L}) + 2\dot{\boldsymbol{\theta}} \times \mathbf{v}_{rel} + \mathbf{a}_{rel} \quad (3.15)$$

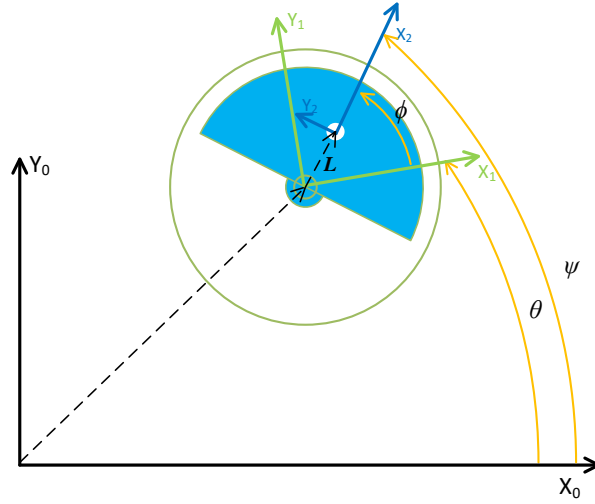


Figure 3.16. Schematic of the generalized rotational harvester model.

where \mathbf{a}_{ref} and \mathbf{a}_{rel} are the absolute acceleration of housing, measured from the global inertial frame, and the relative acceleration of the rotor with respect to the housing, respectively. \mathbf{v}_{rel} is the relative velocity of the rotor with respect to the housing. All the vectors in Eq. (3.15) can be expressed with the Cartesian components along X_I , Y_I , and Z_I axes as

$$\ddot{\boldsymbol{\theta}} \times \mathbf{L} = \ddot{\theta} \mathbf{k}_1 \times L(\cos \phi \mathbf{i}_1 + \sin \phi \mathbf{j}_1) = L\ddot{\theta}(-\sin \phi \mathbf{i}_1 + \cos \phi \mathbf{j}_1) \quad (3.16)$$

$$\begin{aligned} \dot{\boldsymbol{\theta}} \times (\dot{\boldsymbol{\theta}} \times \mathbf{L}) &= \dot{\theta} \mathbf{k}_1 \times (\dot{\theta} \mathbf{k}_1 \times L(\cos \phi \mathbf{i}_1 + \sin \phi \mathbf{j}_1)) \\ &= L\dot{\theta}^2(-\cos \phi \mathbf{i}_1 - \sin \phi \mathbf{j}_1) \end{aligned} \quad (3.17)$$

$$\begin{aligned} 2\dot{\boldsymbol{\theta}} \times \mathbf{v}_{rel} &= 2\dot{\theta} \mathbf{k}_1 \times L\dot{\phi}(-\sin \phi \mathbf{i}_1 + \cos \phi \mathbf{j}_1) \\ &= 2L\dot{\theta}\dot{\phi}(-\cos \phi \mathbf{i}_1 - \sin \phi \mathbf{j}_1) \end{aligned} \quad (3.18)$$

$$\mathbf{a}_{rel} = (-L\dot{\phi}^2 \cos \phi - L\ddot{\phi} \sin \phi)\mathbf{i}_1 + (-L\dot{\phi}^2 \sin \phi + L\ddot{\phi} \cos \phi)\mathbf{j}_1 \quad (3.19)$$

In addition, acceleration of the housing can be expressed along X_I and Y_I axes, which corresponds to the linear acceleration measured by the accelerometer if it is attached to the housing,

$$\mathbf{a}_{ref} = \ddot{X}\mathbf{i}_1 + \ddot{Y}\mathbf{j}_1 \quad (3.20)$$

Substitute Eq. (3.16) - (3.20) into Eq. (3.15),

$$\mathbf{a}_{abs} = (\ddot{X} - L\ddot{\psi} \sin \phi - L\dot{\psi}^2 \cos \phi)\mathbf{i}_1 + (\ddot{Y} - L\ddot{\psi} \cos \phi - L\dot{\psi}^2 \sin \phi)\mathbf{j}_1 \quad (3.21)$$

Similarly, the gravity vector can also be expressed along X_I and Y_I axes as,

$$\mathbf{g} = g_x\mathbf{i}_1 + g_y\mathbf{j}_1 \quad (3.22)$$

The governing equation can be obtained by substituting Eq. (3.21) and Eq. (3.22) into Eq. (3.1) and Eq. (3.2),

3.8 References

- [1] V. Misra et al., “Flexible Technologies for Self-Powered Wearable Health and Environmental Sensing,” Proc. IEEE, vol. 103, no. 4, pp. 665–681, Apr. 2015.
- [2] T. Galchev, E. E. Aktakka, and K. Najafi, “A Piezoelectric Parametric Frequency Increased Generator for Harvesting Low-Frequency Vibrations,” J. Microelectromechanical Syst., vol. 21, no. 6, pp. 1311–1320, 2012.
- [3] P. Pillatsch, E. M. Yeatman, and A. S. Holmes, “A Piezoelectric Frequency Up-Converting Energy Harvester with Rotating Proof Mass for Human Body Applications,” Sensors Actuators, A Phys., vol. 206, pp. 178–185, 2014.
- [4] T. Xue and S. Roundy, “On Magnetic Plucking Configurations for Frequency Up-Converting Mechanical Energy Harvesters,” Sensors Actuators, A Phys., vol. 253, pp. 101–111, 2017.
- [5] T. Xue, H. G. H. G. Yeo, S. Trolier-McKinstry, and S. Roundy, “A Wrist-Worn Rotational Energy Harvester Utilizing Magnetically Plucked {001} Oriented Bimorph PZT Thin-film Beams,” 2017 19th Int. Conf. Solid-State Sensors, Actuators Microsystems, pp. 375–378, 2017.
- [6] M. A. Halim, R. Rantz, Q. Zhang, L. Gu, K. Yang, and S. Roundy, “Electromagnetic Energy Harvesting from Swing-arm Motion Using Rotational Eccentric Mass Structure,” in 2017 19th International Conference on Solid-State Sensors, Actuators and Microsystems (TRANSDUCERS), 2017, pp. 1863–1866.
- [7] J. Nakano, K. Komori, Y. Hattori, and Y. Suzuki, “MEMS Rotational Electret Energy Harvester for Human Motion,” J. Phys. Conf. Ser., vol. 660, p. 12052, 2015.

- [8] J. Wang, W. Wang, G. W. Jewell, and D. Howe, "Design of a Miniature Permanent-Magnet Generator and Energy Storage System," *IEEE Trans. Ind. Electron.*, vol. 52, no. 5, pp. 1383–1390, 2005.
- [9] M. Lossec, B. Multon, H. Ben Ahmed, and H. Ben Ahmed, "Micro-Kinetic Generator: Modeling, Energy Conversion Optimization and Design Considerations," *MELECON 2010 - 2010 15th IEEE Mediterr. Electrotech. Conf.*, pp. 1516–1521, 2010.
- [10] Seiko Corp., "PARTS CATALOGUE / TECHNICAL GUIDE Cal. 5M62A, 5M63A."
- [11] Kinetron, "Micro Generator System '26.4,'" 2014. [Online]. Available: <http://www.kinetron.eu/wp-content/uploads/2015/01/MGS-26.4.pdf>. [Accessed: 01-Sep-2017].
- [12] P. D. Mitcheson, E. M. Yeatman, G. K. Rao, A. S. Holmes, and T. C. Green, "Energy Harvesting from Human and Machine Motion for Wireless Electronic Devices," vol. 96, no. 9, pp. 1457–1486, 2008.
- [13] G. Gorge, M. Kirstein, and R. Erbel, "Microgenerators for Energy Autarkic Pacemakers and Defibrillators: Fact or Fiction?" *Herz*, vol. 26, no. 1, pp. 64–68, 2001.
- [14] M. Magno, L. Spadaro, J. Singh, and L. Benini, "Kinetic Energy Harvesting: Toward Autonomous Wearable Sensing for Internet of Things," 2016 *Int. Symp. Power Electron. Electr. Drives, Autom. Motion, SPEEDAM 2016*, pp. 248–254, 2016.
- [15] T. Xue, S. Kakkar, Q. Lin, and S. Roundy, "Characterization of Micro-Generators Embedded in Commercial-Off-the-Shelf Watches for Wearable Energy Harvesting," *SPIE Smart Struct. Mater. Nondestruct. Eval. Heal. Monit. Int. Soc. Opt. Photonics*, 2016., vol. 9801, pp. 1–8, 2016.
- [16] T. Xue, X. Ma, C. Rahn, and S. Roundy, "Analysis of Upper Bound Power Output for a Wrist-Worn Rotational Energy Harvester from Real-World Measured Inputs," *J. Phys. Conf. Ser.* 557 012090, vol. 557, no. 1, pp. 3–7, 2014.
- [17] P. D. Mitcheson, T. C. Green, E. M. Yeatman, and A. S. Holmes, "Architectures for Vibration-Driven Micropower Generators," *J. Microelectromechanical Syst.*, vol. 13, no. 3, pp. 1–12, 2004.
- [18] E. Halvorsen, C. P. Le, P. D. Mitcheson, and E. M. Yeatman, "Architecture-Independent Power Bound for Vibration Energy Harvesters," *J. Phys. Conf. Ser.*, vol. 476, pp. 117–121, 2013.
- [19] Kinetron, "The 14-pole Micro Generator with Sm₂Co₁₇ magnet (MG4.0)," 2014.

- [Online]. Available: <http://www.kinetron.eu/wp-content/uploads/2014/04/MG4.0.pdf>. [Accessed: 01-Sep-2017].
- [20] D. Zarko, D. Ban, and T. A. Lipo, “Analytical Solution for Cogging Torque in Surface Permanent-Magnet Motors Using Conformal Mapping,” *IEEE Trans. Magn.*, vol. 44, no. 1, pp. 52–65, Jan. 2008.
- [21] Kinetron, “The Micro Generating System for a Watch,” 2014. [Online]. Available: <http://www.kinetron.eu/wp-content/uploads/2014/04/MGSWatch.pdf>. [Accessed: 01-Sep-2017].
- [22] Y. Naruse, N. Matsubara, K. Mabuchi, M. Izumi, and S. Suzuki, “Electrostatic Micro Power Generation from Low-Frequency Vibration Such as Human Motion,” *J. Micromechanics Microengineering*, vol. 19, no. 9, p. 94002, 2009.
- [23] R. Rantz, T. Xue, Q. Zhang, L. Gu, K. Yang, and S. Roundy, “Comparative Analysis of Wrist-Worn Energy Harvesting Architectures,” *J. Phys. Conf. Ser.*, vol. 773, no. 1, pp. 10–13, 2016.
- [24] “IMU Sensor Development Kit | Wireless IMU Sensor | 9DOF Motion Sensor | IMU Development Kit.” [Online]. Available: <http://www.shimmersensing.com/products/shimmer3-development-kit>. [Accessed: 08-Nov-2017].
- [25] S. J. Lee and J. Hidler, “Biomechanics of Overground vs. Treadmill Walking in Healthy Individuals.,” *J. Appl. Physiol.*, vol. 104, no. 3, pp. 747–55, Mar. 2008.

CHAPTER 4

MAGNETIC PLUCKING FOR FREQUENCY UP-CONVERTING PIEZOELECTRIC ENERGY HARVESTERS

© 2016 Elsevier. Reprinted, with permission from, T. Xue and S. Roundy, “On magnetic plucking configurations for frequency up-converting mechanical energy harvesters,” *Sensors Actuators, A Phys.*, vol. 253, pp. 101–111, 2017.



On magnetic plucking configurations for frequency up-converting mechanical energy harvesters



Tiancheng Xue*, Shad Roundy

Department of Mechanical Engineering, University of Utah, Salt Lake City, UT 84112, USA

ARTICLE INFO

Article history:

Received 19 September 2016
Received in revised form
18 November 2016
Accepted 23 November 2016
Available online 24 November 2016

Keywords:

Energy harvesting
Frequency up-conversion
Magnetic plucking
Piezoelectric
Wearables

ABSTRACT

Magnetic plucking applies the strategy of frequency up-conversion in inertial energy harvesting when the energy source, such as human motion, provides excitations with very low and irregular frequencies. In a typical implementation, a slower moving inertial mass magnetically plucks a piezoelectric cantilever beam which converts mechanical energy to electrical energy at a higher frequency. We categorize several feasible magnet configurations to achieve plucking. We classify these as either in-plane (the beam is deflected in the plane of proof mass motion) or out-of-plane (the beam is deflected orthogonal to the plane of proof mass motion). Whereas in-plane plucking induces a clean ring down due to its inherent jump phenomenon, out-of-plane plucking enables the capability of fabricating multiple piezoelectric beams on a single substrate. This paper presents an analysis of three different out-of-plane plucking configurations along with the in-plane repulsive configuration based on a three-dimensional analytical cube permanent magnet model. We derive a magnetically plucked piezoelectric beam model to investigate the dynamic characteristic for different plucking configurations. After validating the model with experimental results we extend the simulation into a larger driving frequency domain to compare two types of magnet configurations in terms of power generation.

© 2016 Elsevier B.V. All rights reserved.

1. Introduction

Mechanical energy harvesters convert ambient vibration into electricity to power sensors and electronics as an alternative to conventional batteries when energy independence is preferred. In general, these harvesters apply one of three basic transduction mechanisms to achieve the electromechanical conversion: electrostatic, electromagnetic, or piezoelectric. The feasibility of using energy harvesters to power wireless sensor nodes has been validated [1–3] and industrial applications such as self-powered tire pressure sensors have been realized [4].

In recent years, there has been a growing interest in studying energy harvesting from human motion in the research community due to the emerging market for wearables. Currently, commercially available wearable wellness products all suffer from the hassle of needing to frequently recharge the batteries. Wearable energy harvesting could provide the potential for continuous 24/7 health monitoring which is crucial for some clinical applications such as electrocardiographic (ECG) monitoring [5]. We categorize human motion into inertia motion, in which the human motion excites

an inertial mass from which power is generated, and joint motion, in which energy is harvested directly from the rotation of a joint such as the knee. In the case of joint motion, a conventional electric generator based harvester has been demonstrated in Ref. [6] to generate power from the knee joint during human gait. The prototype is considerably bulky (790 g) as a wearable device. As the size of the harvester reduces, piezoelectric transducers becomes more practical. This is especially true if gearing systems can't be used which are usually necessary to increase the voltage from electromagnetic harvesters. Wearable electronic devices are typically designed as wrist bands or chest bands. At these body locations the inertia motion is more relevant. However, the inherent limitation of utilizing human motion as the source for inertial energy harvesting is that it only provides excitations with very low and irregular frequencies. Typically, a linear oscillator based energy harvester operates at its natural frequency to take advantage of the peak dynamic magnification. At very low frequencies, this requires very large proof mass motions, which are not feasible for wearable energy harvesters. Furthermore, the very slow and large amplitude proof mass motion does not directly actuate a transducer very effectively. For example, as mentioned earlier, the slow speed results in very low voltages from an electromagnetic transducer. Furthermore, a large amplitude motion would typically require unfeasibly large piezoelectric displacements. Thus a standard linear

* Corresponding author.

E-mail address: tiancheng.xue@utah.edu (T. Xue).

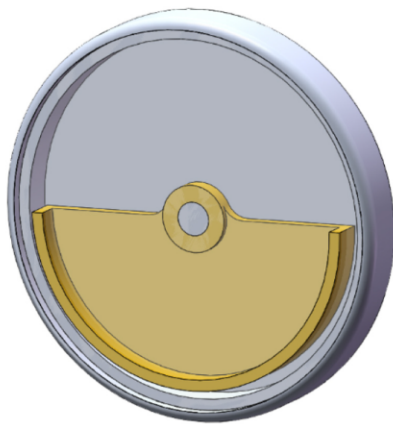


Fig. 1. Eccentric rotor-based energy harvester.

energy harvester suffers from low effectiveness [7] in the case of wearables. Frequency up-conversion is a commonly applied strategy to tackle this issue by transforming the low-frequency input motion into a high-frequency actuation of the transducer. In terms of piezoelectric energy harvesters, plucking a cantilever beam is one technique that applies such a strategy. Eccentric rotor-based wearable energy harvesters have been demonstrated in the literature either using magnets [8–10] or pins [11,12] to pluck piezoelectric beams. Depending on the location, the target power output of these harvesters are either a few dozen microwatts (wrist) or milliwatts (knee joint). In these harvesters, the proof mass is a semicircular rotor, such as those originally used in self-winding automatic and motion-powered quartz watches [13,14]. As shown in Fig. 1, the rotational proof mass can be excited in all directions with no inherent motion limit, which caters to the irregular nature of human motion. Compared to mechanical plucking, the use of magnetic coupling to pluck the piezoelectric beams provides better reliability since it can be designed to be contact-free. Usually magnets are arranged to pluck the beam in the direction of magnet motion as shown in Fig. 2(a), which is defined as in-plane plucking. Whereas the in-plane plucking introduces a jump phenomenon to cause ring down in the cantilever beam, another configuration, the out-of-plane plucking provides some alternative advantages, making it worth investigation. In addition, a better understanding of the

plucked beam dynamics will help improve the performance of the plucked piezoelectric beam-based energy harvesters.

We present three alternative out-of-plane magnetic plucking configurations in this paper: the direct repulsive configuration (DRC), the orthogonal configuration (OC), and the indirect repulsive configuration (IRC). As shown in Fig. 2(b)–(d), the beam deflection direction is perpendicular to the plane of magnet motion in the out-of-plane plucking configurations. This arrangement enables the possibility of fabricating multiple beams on a single substrate [15] which reduces assembly complexity when multiple beams are embedded in the device to achieve higher power output. In addition, it has better MEMS process compatibility when the device is scaled down.

This work expands upon a previous analysis on magnetic plucking configurations based on static magnetic force profiles [15] (i.e. interaction between one fixed magnet and one moving magnet). We have augmented the model into a full dynamic magnetic plucking system based on a distributed parameter piezoelectric bimorph beam model while incorporating magnetic actuation forces in both transverse and axial directions. A three-dimensional surface fitting technique can be employed to save computation time by simplifying the analytical magnet model in a dynamic simulation. Both simulation and experimental results will be presented and discussed with respect to implementation in frequency up-converting energy harvesting systems.

2. Magnetic plucking configurations

2.1. Forces exerted between permanent magnets

The fundamental idea behind magnetic plucking is to use magnetic coupling to create a force profile in the form of a narrow Gaussian function, mimicking an abrupt and clean release of the beam tip. Therefore, the quantitative determination of the magnetic interaction force is of great importance. In a degenerate case, permanent magnets can be simplified to magnetic dipoles when the sizes are negligible compared to the distance between them. In a more general case, however, it is difficult to obtain an accurate expression analytically for the interaction between permanent magnets. Nevertheless, some analytical solutions for simple geometries exist in the literature based on either the Coulombian charge model [16] or the Ampère's current model [17] with the assumption of constant and uniform polarization. In more recent work, Kelvin's formula has also been applied to derive closed-form solutions for forces acting on the magnet due to

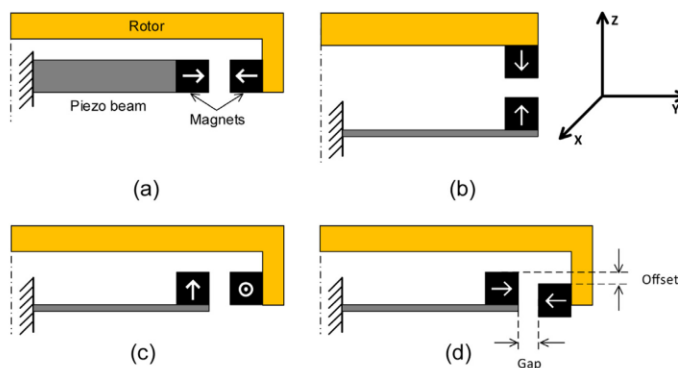


Fig. 2. Magnetic plucking configurations in section view: (a) in-plane plucking configuration, (b) out-of-plane direct repulsive configuration (DRC), (c) out-of-plane orthogonal configuration (OC), (d) out-of-plane indirect repulsive configuration (IRC). The moving magnet is attached on the rotor and moves in the x direction at this instance. In (a), the beam bends in the x direction whereas in (b) (c) (d), it bends in the z direction.

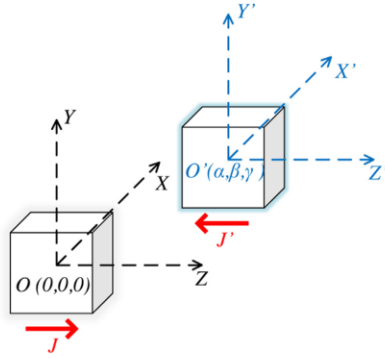


Fig. 3. Schematic of the generic magnetic configuration with repelling magnets.

the field originated by a second magnet [18,19]. Although computationally expensive, finite element methods based on Maxwell's stress tensor or virtual work principle predict more reliable results [20] especially for complex geometries.

For many energy harvesting devices, the size of the magnets used for plucking piezoelectric beams is on the same order of magnitude as the distance. Thus, a simple magnetic dipole model is not appropriate. In addition, the magnetic torque is often overlooked in previous studies on magnetic plucking whereas it could potentially provide a nontrivial excitation [10,21]. We applied an analytical solution [16] in this study to obtain the static magnetic force profile as a starting point. Note that the aspect ratio, i.e., the ratio of the thickness to the width of a magnet for a given volume plays an important role in determining its strength. It has been shown that an aspect ratio of 1 falls in the optimal range to achieve maximum contact force per volume [19]. Therefore, cube magnets are chosen for this study. Granted the fact that modern rare-earth magnets exhibit good magnetization uniformity, a cube magnet can be modelled as two surfaces of evenly distributed magnetic charges [16]. The total potential energy between two cube magnets shown in Fig. 3 with parallel magnetization directions is given by:

$$E = \frac{JJ'}{4\pi\mu} \sum_{m=0}^1 \sum_{n=0}^1 \sum_{l=-1}^1 \sum_{l'=-1}^1 \int \int \int \int \frac{(-1)^{m-n}}{\sqrt{(\alpha + X' - X)^2 + (\beta + Y' - Y)^2 + (\gamma + 2(m-n)l)^2}} dX'dY'dXdY \quad (1)$$

where J and J' are the magnetic polarizations for each cube magnet of length $2l$ and μ is the permeability of the medium. Note that here we assume uniform permeability whereas a difference does exist between air and magnetic material, which introduces a small error of less than 5%. O and O' are the center of the cube magnets. The origin of the $O'X'Y'Z'$ frame is located at (α, β, γ) with respect to the $OXYZ$ frame (see Fig. 3). The forces acting on the fixed magnet originating at O are the derivative of the potential energy with respect to each direction:

$$F = -\frac{JJ'}{4\pi\mu} \sum_{i=0}^1 \sum_{j=0}^1 \sum_{k=0}^1 \sum_{l=0}^1 \sum_{p=0}^1 \sum_{q=0}^1 (-1)^{i+j+k+l+p+q} \psi'(\bar{U}_{ij}, \bar{V}_{kl}, \bar{W}_{pq}, \bar{R}) \quad (2)$$

where

$$\psi_x(\bar{U}, \bar{V}, \bar{W}, \bar{R}) = \frac{(\bar{V}^2 - \bar{W}^2)}{2} \ln\left(\frac{\bar{R} - \bar{U}}{l_0}\right) + \bar{U}\bar{V} \ln\left(\frac{\bar{R} - \bar{V}}{l_0}\right) + \bar{V}\bar{W}\tan^{-1}\left(\frac{\bar{U}\bar{V}}{\bar{W}\bar{R}}\right) + \frac{1}{2}\bar{U}\bar{R} \quad (3)$$

$$\psi_y(\bar{U}, \bar{V}, \bar{W}, \bar{R}) = \frac{(\bar{U}^2 - \bar{W}^2)}{2} \ln\left(\frac{\bar{R} - \bar{V}}{l_0}\right) + \bar{U}\bar{V} \ln\left(\frac{\bar{R} - \bar{U}}{l_0}\right) + \bar{U}\bar{W}\tan^{-1}\left(\frac{\bar{U}\bar{V}}{\bar{W}\bar{R}}\right) + \frac{1}{2}\bar{V}\bar{R} \quad (4)$$

$$\psi_z(\bar{U}, \bar{V}, \bar{W}, \bar{R}) = -\bar{U}\bar{W} \ln\left(\frac{\bar{R} - \bar{U}}{l_0}\right) - \bar{V}\bar{W} \ln\left(\frac{\bar{R} - \bar{V}}{l_0}\right) + \bar{U} \bar{V}\tan^{-1}\left(\frac{\bar{U}\bar{V}}{\bar{W}\bar{R}}\right) - \bar{W}\bar{R} \quad (5)$$

where l_0 is the unit rate constant to keep the argument of the logarithm function dimensionless. \bar{U} , \bar{V} , \bar{W} , and \bar{R} are geometric parameters given by:

$$\bar{U}_{ij} = \alpha + ((-1)^j - (-1)^i)l \quad (6)$$

$$\bar{V}_{kl} = \beta + ((-1)^l - (-1)^k)l \quad (7)$$

$$\bar{W}_{pq} = \gamma + ((-1)^q - (-1)^p)l \quad (8)$$

$$\bar{R} = \sqrt{\bar{U}_{ij}^2 + \bar{V}_{kl}^2 + \bar{W}_{pq}^2} \quad (9)$$

A similar formula can be derived for the case where the magnetic polarizations are perpendicular or even arbitrarily oriented [22]. The magnetic torque components can be calculated as well with respect to each axis. We applied the analytical expressions above to obtain the interactions between magnets for the different magnetic plucking configurations shown earlier in Fig. 2. The contribution of the torque to the dynamics compared with the force depends on the length of the cantilever beam. For a cantilever beam longer than 10 mm as used in our study, the contribution of the torque is more than an order of magnitude smaller than the contribution of the force. Thus, we have neglected the torque components. As illustrated in Fig. 4, the static force profile is given as a function of the magnet displacement normalized by the length of magnet $2l$. The force is normalized to be 1 at its maximum for the transverse component in the direct repulsive configuration (i.e., F_z). The moving magnet on the rotor is assumed to follow a linear path as the small angles between the opposing surfaces of the magnets can be neglected. In this example the length of the N50 magnets is 2 mm and the gap between them is 1 mm. A 1 mm offset in the z direction is applied in the indirect repulsive configuration. Note that an offset in the z direction is essential to the indirect repulsive configuration as there will be no transverse force without it. We used the boundary integral method based Radia software [23] developed by the European Synchrotron Radiation Facility (ESRF) to provide a numerical validation for the analytical model.

As is evident from Fig. 4, the analytical model matches the numerical results well. In general, the transverse force (along the direction of beam deflection) and the axial force (along the direction of beam length) are of interest for plucking. The transverse force directly deflects the beam whereas the axial force softens the beam and provides a bending moment when the beam is already deflected. Note that due to the different orientations in Fig. 2, the transverse force in the in-plane plucking configuration is F_x whereas in the out-of-plane plucking configurations it is F_z .

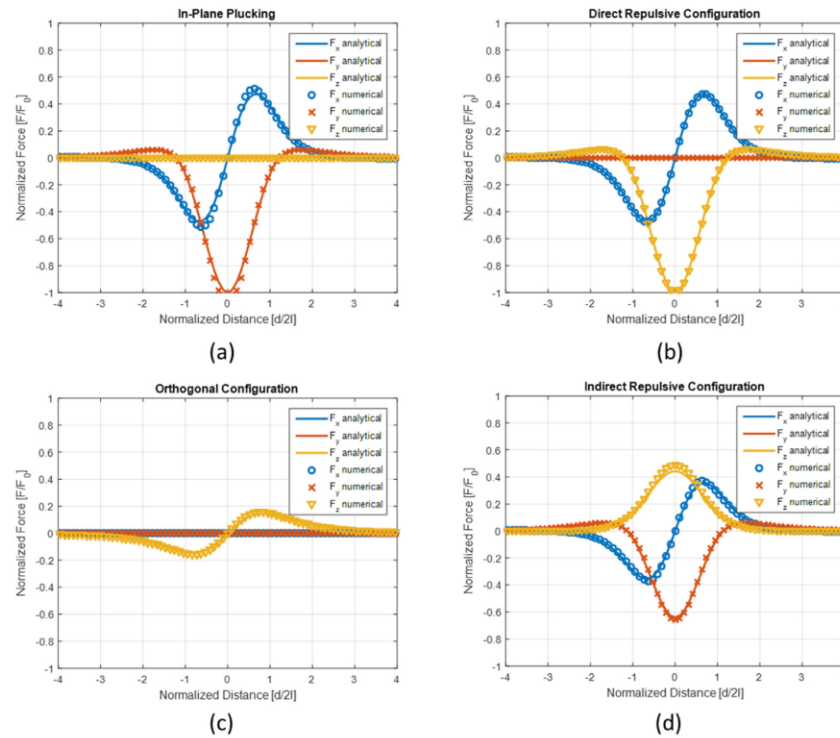


Fig. 4. Static force profiles for different magnetic plucking configurations. The transverse force is F_x in (a) in-plane plucking configuration, and F_z in (b), (c), (d) out-of-plane plucking configurations.

Although the lateral force could potentially produce a torsional movement, we leave it out in the later modelling due to a relatively high torsional rigidity of the beam applied in our study.

2.2. In-plane plucking

As shown in Fig. 4(a), the directionality of the transverse force F_x changes at the zero displacement point in the in-plane plucking configuration. As mentioned earlier a jump phenomenon will occur due to the magnetic interaction and the cantilever restoring force. To investigate this phenomenon we formulate the following equation to find the equilibrium beam tip position with a spring model for the beam and a published dipole model [24] for the magnet for simplicity.

$$\frac{3\mu_0}{4\pi|d|^5} [(m_1 \cdot d)m_2 + (m_2 \cdot d)m_1 + (m_1 \cdot m_2)d - \frac{5(m \cdot d)(m_2 \cdot d)}{|d|^2} d] \cdot \hat{i} - kx_b = 0 \quad (10)$$

where

$$\mathbf{d} = [-x_m + x_b \quad 0] \quad (11)$$

$$\hat{i} = [1 \quad 0]^T \quad (12)$$

where \mathbf{m}_1 and \mathbf{m}_2 are the dipole moments, k is the equivalent beam stiffness, x_m is the moving magnet displacement, and x_b is the beam tip displacement. The zeros of Eq. (10) are plotted in Fig. 5 with arrows marking the jump locations. This bifurcation guarantees a dynamic ring down of the beam at its natural frequency after it

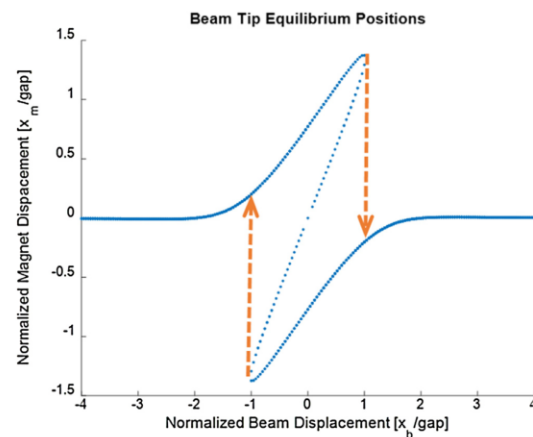


Fig. 5. Bifurcation in the in-plane plucking configuration.

has been deflected and released. In general the plucking occurs as long as the moving magnet passes the beam and the jump location. Thus, the jump phenomenon has little dependency on the velocity. The jump location will not move much as long as the velocity is moderate.

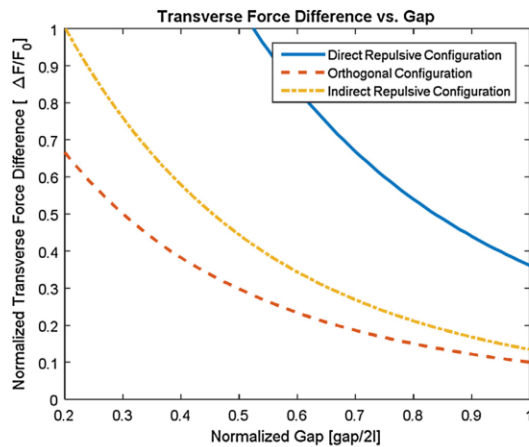


Fig. 6. Comparison of transverse force difference for different out-of-plane magnetic plucking configurations.

2.3. Out-of-plane plucking

For the out-of-plane plucking configurations, the transverse force F_z is predominantly in the same direction (i.e. it does not change sign) for both the direct repulsive and the indirect repulsive configurations. While the transverse force does change its directionality in the orthogonal configuration, its magnitude is relatively small compared to the in-plane plucking configuration given the same gap between magnets. Most importantly, the orientation of the beam eliminates the jump phenomenon in out-of-plane configurations. Therefore, for out-of-plane configurations, plucking (i.e. a dynamic ring down after the beam is deflected and released at its natural frequency) occurs only when the velocity of moving magnet exceeds a certain threshold. To be more precise, it requires the force ramp to be faster than the beam can respond due to its resonant frequency. Otherwise the beam will only undergo a gradual deflection without any dynamic ring down. The voltage output is significantly reduced in this scenario. Nevertheless, the appeal of out-of-plane plucking is that we can easily embed multiple beams to increase total power output by fabricating them on a single substrate as mentioned earlier.

Among the three out-of-plane configurations, for a given gap between magnets, the direct repulsive configuration exhibits the largest transverse force difference, i.e., the absolute difference between the maximum and the minimum transverse force during actuation. The indirect repulsive configuration benefits from a large axial force whereas the orthogonal configuration operates in a pure deflecting mode, i.e., only the transverse force is generated. Although the direct repulsive configuration seems the most promising to trigger plucking, it requires a larger gap between magnets to avoid the pull-in effect (i.e., opposing magnets get stuck together in a side by side orientation) and a larger space for beam deflection. Since the magnets are aligned in the direction of device thickness, this hurts the overall power density, which is important as wearables are extremely size-sensitive. In the other two configurations magnets are highly unlikely to touch each other, thus we are able to implement a smaller gap between magnets which results in a larger force. As illustrated in Fig. 6, by implementing a smaller gap, the indirect repulsive or the orthogonal configuration can achieve a higher transverse force difference than the direct repulsive configuration with a larger gap.

In addition, the offset in the indirect repulsive configuration can be optimized to increase the transverse force. Because of the existence of a transcendental function in Eq. (3)–(5), a geometric scaling effect on the force between magnets cannot be easily obtained via an analytical approach by non-dimensionalization. Nevertheless, a scaling of the magnetic force $F \propto l^2$ does hold in some particular cases, such as the contact force, when two magnets are aligned precisely [19]. Although no global geometric scaling invariance appears in the equation, we can numerically demonstrate the optimal range of operation for the indirect repulsive configuration. Fig. 7 shows that for a given normalized gap there is an optimal normalized offset to achieve the maximum transverse force regardless of the magnet length. In this case the magnet length is varied from $1 \mu\text{m}$ to 1mm . The optimal offset marked by the black arrow in Fig. 6 is dependent on the gap between magnets and will increase as the gap grows.

3. A model for magnetically plucked piezoelectric beams

A cantilevered composite beam, as illustrated in Fig. 8, is a common implementation of a piezoelectric energy harvester. Numerous models of a piezoelectric beam, typically under harmonic base excitation, have been published. In general, there are two approaches: the lumped parameter model and the distributed parameter model. A detailed review of these various modelling methods is given by Erturk and Inman [25]. For a magnetically plucked piezoelectric beam, however, the forcing mechanism is the magnetic force acting at the free end instead of the base excitation. Previous modelling attempts [21,26] tend to simplify the magnetic force model as in those cases the permanent magnets are in a direct repulsive or attractive configuration. However, when considering more complex magnet orientations, these simplified models lack accuracy.

Our modelling procedure follows Erturk and Inman's distributed parameter piezoelectric beam model [27] with modified forcing conditions and the addition of magnetic coupling. The piezoelectric bimorph is connected in series. Based on Euler-Bernoulli beam theory, the kinetic and potential energy of a cantilever bimorph beam with active length L and width b subjected to a transverse force F_z and an axial force F_y is given by

$$T = \frac{1}{2} \int_0^L m \left[\frac{\partial w(x, t)}{\partial t} \right]^2 dx + \frac{1}{2} M_t \left[\frac{\partial w(x, t)}{\partial t} \right]_{x=L}^2 + \frac{1}{2} I_t \left[\frac{\partial^2 w(x, t)}{\partial x \partial t} \right]_{x=L}^2 \quad (13)$$

$$U = \frac{1}{2} \int_0^L \left[YI \left[\frac{\partial^2 w(x, t)}{\partial x^2} \right]^2 - \vartheta_s v(t) \frac{\partial^2 w(x, t)}{\partial x^2} \right] dx \quad (14)$$

where

$$\vartheta_s = b \int_{\frac{1}{2}h_s}^{\frac{1}{2}h_s+h_p} \frac{d_{31} \bar{c}_{11}^E}{h_p} z dz = \frac{1}{2} d_{31} \bar{c}_{11}^E b (h_p + h_s) \quad (15)$$

where $w(x, t)$ is the transverse displacement of the beam, $v(t)$ is the voltage across the two piezoelectric layers, M_t and I_t are the mass and the mass moment of inertia of the proof mass (i.e., a permanent magnet) at the free end, and d_{31} is the piezoelectric strain coefficient. YI is the effective bending stiffness of the composite beam, which can be expressed as a function of its piezoelectric layer

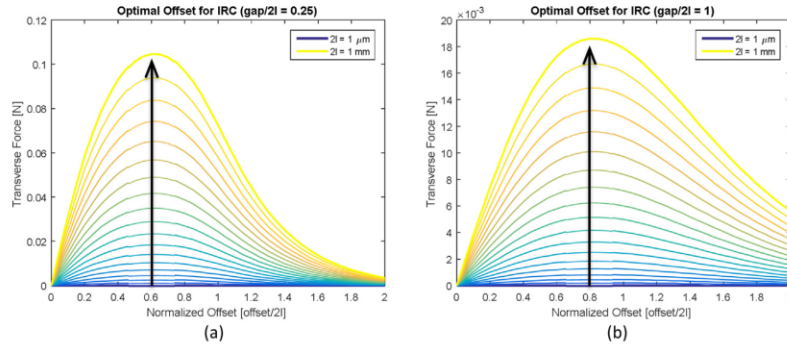


Fig. 7. Optimal offset for indirect repulsive configuration with the magnet length $2l$ varied from $1 \mu\text{m}$ to 1mm (marked by the arrow): (a) normalized optimal offset is around 0.6 when the normalized gap is 0.25, (b) normalized optimal offset is around 0.8 when the normalized gap is 1.

and substructure layer thickness h_p and h_s with the corresponding elastic modulus \bar{c}_{11}^E and Y_s respectively:

$$YI = \frac{2b}{3} \left\{ Y_s \frac{h_s^3}{8} + \bar{c}_{11}^E \left[\left(h_p + \frac{h_s}{2} \right)^3 - \frac{h_s^3}{8} \right] \right\} \quad (16)$$

m is the mass per unit length of the beam determined by the beam geometry and the densities of the piezoelectric and substructure layers ρ_p and ρ_s :

$$m = b (\rho_s h_s + 2\rho_p h_p) \quad (17)$$

The extended Hamilton's principle can be applied in the absence of mechanical damping effects:

$$\delta \int_{t_1}^{t_2} (T - U + W_{ie} + W_{nc}) dt = 0 \quad (18)$$

where W_{nc} is the total work done by the non-conservative mechanical forces including the transverse force F_z , the axial force F_y and the work due to the non-conservative electric charge output $Q(t)$, and W_{ie} is the internal electrical energy in the piezoelectric layers given by

$$W_{nc} = - \int_0^L F_y \left[\frac{\partial w(x,t)}{\partial x} \right]^2 + F_z w(L,t) + Q(t) v(t) \quad (19)$$

$$W_{ie} = \frac{1}{2} \left[\int_0^L \vartheta_s v(t) \frac{\partial^2 w(x,t)}{\partial x^2} dx + \frac{1}{2} C_p v^2(t) \right] \quad (20)$$

Here the effective capacitance of the piezoelectric layer C_p is a function of $\bar{\epsilon}_{33}^s$, the material permittivity evaluated at constant strain and beam geometry. Note that the total beam length, L_t , is used here instead of the active length L as the electrode covers the entire beam surface. In practice the capacitance can be simply obtained from measurement.

$$C_p = \frac{\bar{\epsilon}_{33}^s b L_t}{h_p} \quad (21)$$

The governing equations of the system can be obtained from the electromechanical Lagrange's equations based on the extended Hamilton's principle. By introducing viscous air damping and strain

rate damping back into the system, the equation of motion can be expressed as

$$YI \frac{\partial^4 w(x,t)}{\partial x^4} + c_s I \frac{\partial^5 w(x,t)}{\partial x^4 \partial t} + c_a \frac{\partial w(x,t)}{\partial t} + m \frac{\partial^2 w(x,t)}{\partial t^2} + \left[M_t \frac{\partial^2 w(x,t)}{\partial t^2} + I_t \frac{\partial^3 w(x,t)}{\partial x \partial t^2} \right] \delta(x-L) - \quad (22)$$

$$F_y(t) \frac{\partial^2 w(x,t)}{\partial x^2} - \vartheta_s v(t) \left[\frac{d\delta(x)}{dx} - \frac{d\delta(x-L)}{dx} \right] = F_z(t) \delta(x-L)$$

where $\delta(x)$ is the Dirac delta function, c_s and c_a are the strain rate and viscous air damping coefficients respectively. These coefficients can be calculated from the first two modal damping coefficients [27], which are typically obtained experimentally using the logarithmic decrement method. We follow the standard assumed-modes method to represent the displacement of the beam $w(x,t)$ as a convergent series of the eigenfunctions:

$$w(x,t) = \sum_{r=1}^{\infty} \phi_r(x) \eta_r(t) \quad (23)$$

where $\phi_r(x)$ and $\eta_r(t)$ are the mass normalized eigenfunction and the modal mechanical coordinate of the cantilever beam with respect to its r th mode shape. The equation of motion can be further reduced to the modal coordinate by substituting Eq. (23) into Eq. (22) and integrating over the beam length:

$$\frac{d^2 \eta_r(t)}{dt^2} + 2\zeta_r \omega_r \frac{d\eta_r(t)}{dt} + \omega_r^2 \eta_r(t) - \vartheta_s \left[\frac{d\phi_r(x)}{dx} \right]_{x=L} v(t) = [F_z(t) \phi_r(x)]_{x=L} \quad (24)$$

In the above equation, ζ_r is the modal damping ratio and ω_r is the effective undamped modal frequency of the beam in the presence of the axial excitation force. The corresponding electrical equation of a bimorph piezoelectric beam in series connection with a resistive load R_l is

$$\frac{C_p}{2} \frac{dv(t)}{dt} + \frac{v(t)}{R_l} + \sum_{r=1}^n \vartheta_s \left[\frac{d\phi_r(x)}{dx} \right]_{x=L} \frac{d\eta_r(t)}{dt} = 0 \quad (25)$$

We can obtain the full magnetically plucked piezoelectric beam model by combining the piezoelectric beam model and the magnetic force model. Eq. (2) shows that each magnetic force component is a sum of 64 values of the function ψ , which could be computationally expensive in a dynamic simulation where the force needs to be updated at each time step. Thus, we desire a further simplification without much sacrifice in precision for a full energy harvester model. Since the deflection of the beam adds

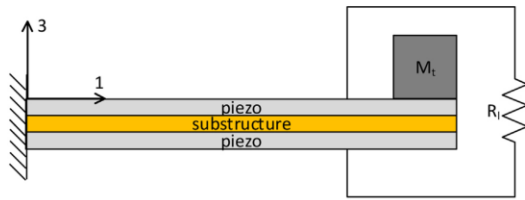


Fig. 8. Piezoelectric bimorph beam with magnet attached to the free end in series connection.

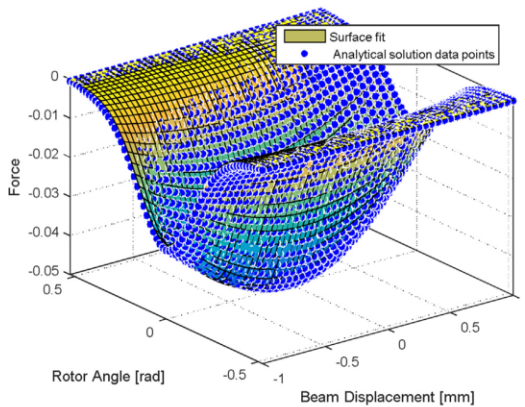


Fig. 9. Surface fitting for the transverse force F_z in indirect repulsive configuration.

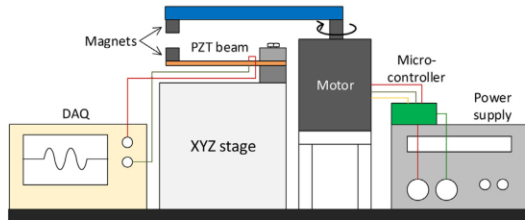


Fig. 10. Experimental set-up for the magnetically plucked piezoelectric beam model with different magnetic plucking configurations.

another dimension into the dynamic force profile, we applied a surface fit to the analytical solution using a function as the product of a Gaussian and a polynomial in two dimensions x and z respectively:

$$F = a \left((z - z_0) + (z - z_1)^2 \right) \exp \left(\frac{-(x - x_0)^2}{\sigma^2} \right) \quad (26)$$

where a , x_0 , z_0 , z_1 , and σ are fitting parameters.

Fig. 9 gives an example of the fitted surface for the transverse magnetic force in the indirect repulsive configuration as the function of the rotor angle and the beam displacement. A similar procedure can be applied to other configurations.

4. Experimental results

4.1. Experimental setup

To validate the magnetically plucked piezoelectric beam model we designed an experimental set-up as shown in Fig. 10. A piezoelectric beam made by Piezo Systems Inc. is clamped on an

Table 1
Parameters for the piezoelectric bimorph beam.

Parameter	Value
L	26.4 mm
b	3.2 mm
h_s	0.1 mm
h_p	0.14 mm
ρ_s	7800 kg m^{-3}
ρ_p	8500 kg m^{-3}
Y_s	$100 \times 10^9 \text{ N m}^{-2}$
Z_{11}^E	$66 \times 10^9 \text{ N m}^{-2}$
d_{31}	$-190 \times 10^{-12} \text{ m V}^{-1}$
ϵ_{33}^S	$1.593 \times 10^{-8} \text{ F m}^{-1}$
C_p	10 nF
R_t	120 k Ω

adjustable XYZ stage with alternative clamps for different magnetic plucking configurations. The brass reinforced piezoelectric beam is made with PSI-5A4E piezoceramic material and is coated with electrodes on each side. The original length of the beam is 31.4 mm and is shortened to an active length of 26.4 mm due to the clamp and the tip magnet. The complete list of parameters of the beam is given in Table 1.

The excitation is achieved with a motor-driven aluminum swing arm. The motor driving profile can be varied to achieve different magnetic plucking velocities. N50 cube magnets ($2 \text{ mm} \times 2 \text{ mm} \times 2 \text{ mm}$) are attached at both the end of the piezoelectric beam and the swing arm with orientations corresponding to each magnetic plucking configuration. The effective swing arm length for the magnet is 62.5 mm, which results in a tangential velocity of 196 mm s^{-1} at $\pi \text{ rad s}^{-1}$. During the excitation, we measure the voltage output from the electrodes across a 120 k Ω resistor based on impedance matching.

4.2. Results and discussion

In this section we present time domain voltage waveforms from both simulation and experimental results for different magnetic plucking configurations. The simulation was conducted in Matlab. Again, within the small region of magnetic interaction, the path of the moving magnet is approximated as linear and thus the small angles between the opposing surfaces of the magnets are neglected. In general, a good match in terms of waveform shape between simulation and measurement is demonstrated with a slight discrepancy in the value of voltage output. This is most likely due to inexactness in material properties of the piezoelectric beam and the residual flux density of the permanent magnet as in most cases the material properties are given as a range. Inaccuracies in adjusting the gap and the offset between magnets also contribute to the overall error.

For the in-plane plucking configuration, the main takeaway from the previous analysis is that the plucking is due to the bifurcation in the resultant forces, and thus places no requirement on the moving magnet velocity. This is illustrated in Fig. 11 with motor driving speed of $\pi/2 \text{ rad s}^{-1}$ and $2\pi \text{ rad s}^{-1}$. The maximum voltage output during the initial deflection is around 50 V for both cases. A clear ring down of oscillations is demonstrated, indicating a clean release of the beam. In this case, a higher excitation velocity will increase the number of excitations per unit time but the energy produced per excitation improves only marginally.

For out-of-plane plucking configurations, as shown in Figs. 12, 13 and 14, the dynamics of the piezoelectric beam are dependent on the velocity of the moving magnet. A higher driving speed will produce a cleaner ring down and a higher voltage. At a lower motor driving speed of $\pi \text{ rad s}^{-1}$, the beam in the direct repulsive and indirect repulsive configuration only exhibits a gradual deflection with minimal ring down whereas a biased

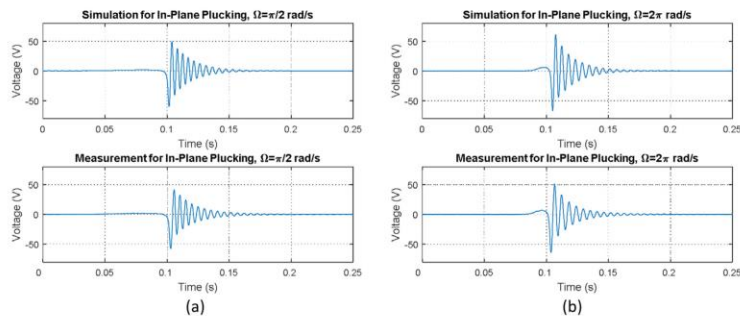


Fig. 11. Simulated and measured voltage output from the piezoelectric beam for the in-plane plucking configuration ($gap = 1\text{ mm}$) with motor driving speed of (a) $\pi/2\text{ rad s}^{-1}$ and (b) $2\pi\text{ rad s}^{-1}$.

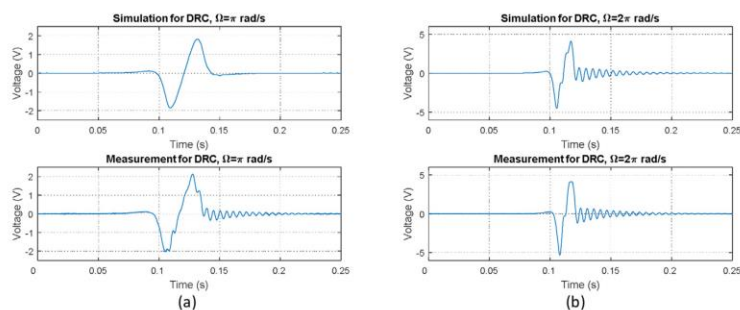


Fig. 12. Simulated and measured voltage output from the piezoelectric beam for the direct repulsive configuration ($gap = 2\text{ mm}$) with motor driving speed of (a) $\pi\text{ rad s}^{-1}$ and (b) $2\pi\text{ rad s}^{-1}$.

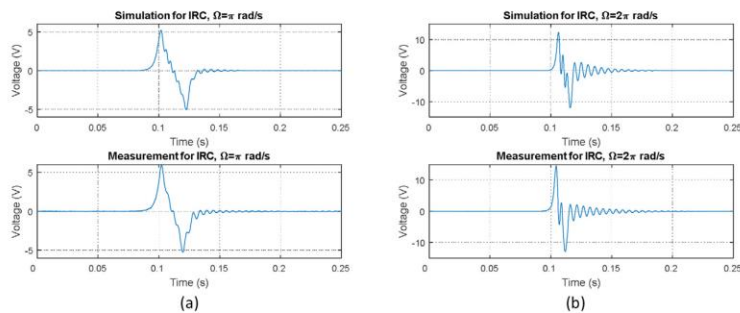


Fig. 13. Simulated and measured voltage output from the piezoelectric beam for the indirect repulsive configuration ($gap = 0.5\text{ mm}$) with motor driving speed of (a) $\pi\text{ rad s}^{-1}$ and (b) $2\pi\text{ rad s}^{-1}$.

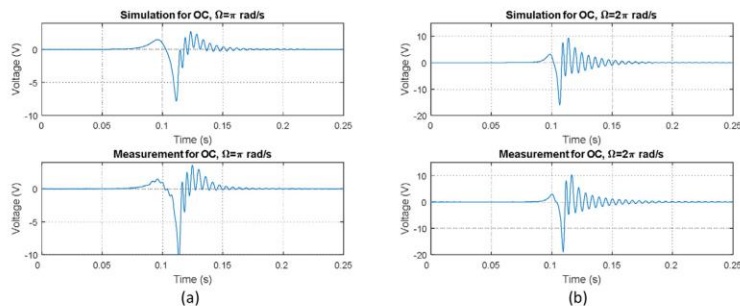


Fig. 14. Simulated and measured voltage output from the piezoelectric beam for the orthogonal configuration ($gap = 0.5\text{ mm}$) with motor driving speed of (a) $\pi\text{ rad s}^{-1}$ and (b) $2\pi\text{ rad s}^{-1}$.

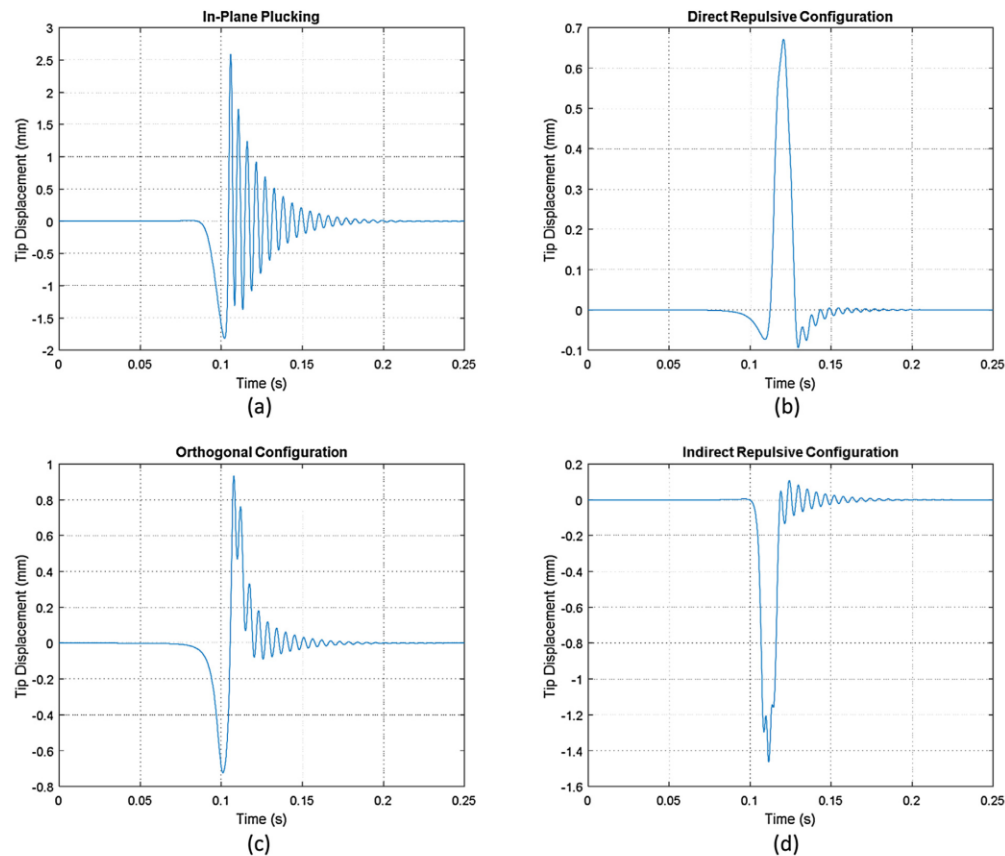


Fig. 15. Simulated beam tip displacement for different magnetic plucking configurations: (a) in-plane plucking configuration, (b) direct repulsive configuration, (c) orthogonal configuration, and (d) indirect repulsive configuration.

ring down exists in the orthogonal configuration. At a higher motor driving speed of $2\pi \text{ rad s}^{-1}$, the voltage approximately doubles with a cleaner ring down after the initial deflection for all out-of-plane plucking configurations. However, there is a big voltage reduction between the first and the second oscillation, indicating a reluctant release from the magnetic force. The voltage reduction is much larger in the direct repulsive and indirect repulsive configuration than in the orthogonal configuration. This is because in the orthogonal configuration the magnetic force directionality changes which guarantees a positive to negative deflection. Magnetic coupling exists in the entire first oscillation of the beam for all configurations, however in the in-plane plucking configuration the beam undergoes a true free oscillation after the initial deflection. This is further illustrated in Fig. 15 with the simulated beam tip displacement for each configuration.

Note that the gap and the offset between magnets used in the experiment are different from the earlier static force profile. We applied a 2 mm gap in the direct repulsive configuration to avoid the pull-in effect, which results in a lower voltage due to the weak magnetic coupling whereas we can implement a 0.5 mm gap to increase the magnetic coupling for the indirect repulsive and orthogonal configurations. A 1 mm offset is applied in the indirect repulsive configuration, which is close to its optimal value.

In general, the in-plane plucking configuration produces more power than the out-of-plane plucking configurations given the same conditions at low driving speeds due to its larger initial deflection and the capability of free oscillation. In practice, however, the in-plane configuration requires a larger driving torque to push the beam through the bifurcation point. For a displacement-driven excitation where the driving force or torque is sufficiently large such as the knee-joint motion [11], the in-plane plucking configuration is the obvious choice. For inertia-driven excitations, when the amplitude of acceleration is low, the in-plane plucking configuration might not function as the moving magnet may not push through the beam. In this case, although the out-of-plane plucking configurations generate less energy per pluck, they may be preferable. A fundamental difference between the two lies in its dependency on velocity to extract energy from the system. The out-of-plane configurations is evidently more sensitive to the velocity of the moving magnet.

We choose to use the maximum power output instead of efficiency to compare different configurations in terms of performance. The efficiency is used typically on the transducer level. It can be defined as the ratio of energy output to potential magnetic energy at its maximum in this case. However it leaves out the velocity of moving magnets which is vital in the dynamic study. Thus a direct comparison of output power is more suitable.

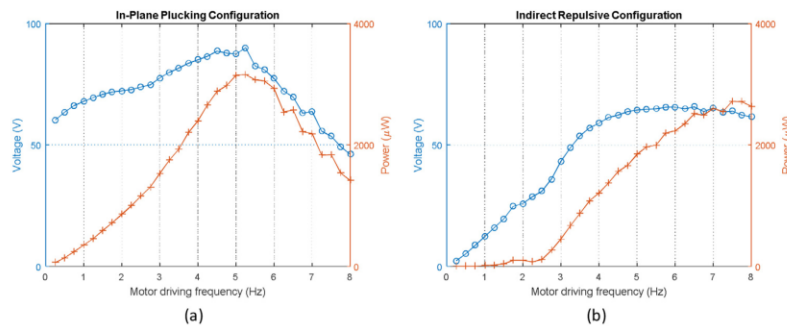


Fig. 16. Simulated maximum voltage and average power output as a function of motor driving frequency for (a) in-plane plucking configuration and (b) indirect repulsive configuration.

To gain insight into the scaling relationship between the excitation frequency (i.e., the motor driving frequency) and the power output, we extend the simulation into a larger frequency range to compare in-plane plucking and out-of-plane plucking. We choose the indirect repulsive configuration as the representative configuration. The simulation is built upon the assumption that the piezoelectric beam is actuated twice per motor cycle which is different from the test set-up. Fig. 16 shows both RMS power and maximum voltage as a function of motor driving frequency. For the in-plane plucking configuration, the maximum voltage scales approximately linearly with the driving frequency until a certain point around 5 Hz. Beyond this speed, the beam has not completely rung down when it gets plucked again. Thus, as the moving magnet starts to interact with the magnet on the beam, there will be an initial deflection, which affects the maximum voltage significantly. We call this the oscillation overlay effect. The power output follows a quadratic curve initially and drops after the oscillation overlay point. Consequently, there is an optimal driving frequency to achieve the maximum power output, which means that the number of actuations per cycle (determined by the number of beams and the number of magnets) can be optimized for a well-defined rotational input. This optimal driving frequency is also dependent on the magnetic configuration and the beam resonant frequency. Given a stiffer beam the optimal point will move towards higher frequencies. The irregular data points above 5 Hz indicate that the oscillation overlay introduces nondeterminism into the system. For the indirect repulsive configuration, the maximum voltage grows linearly at a much larger rate with the motor driving frequency initially and goes into saturation at around 5 Hz. The oscillation overlay has a smaller effect on the voltage output in this case. At lower frequencies the beam only exhibits a gradual deflection which, due to a constant resistive load, generates a very low voltage output. Therefore the indirect repulsive configuration generates minimal power output below 2 Hz. An anomaly occurs at around 2.5 Hz due to a cancelling effect that reduces the dynamic ring down. At this critical driving speed, the magnetic force opposes the second oscillation of the beam which significantly affects the power output. We have only examined frequencies below 10 Hz as this is where frequency up-conversion usually applies.

5. Conclusions

This paper explores alternative configurations to achieve magnetic plucking in frequency up-converting energy harvesters. A piezoelectric beam can be plucked in or out of the plane of motion of the magnet. We presented three configurations to achieve out-of-plane plucking: the direct repulsive configuration, the orthogonal configuration, and the indirect repulsive configuration. An initial

analysis based on a static force profile obtained from an analytical permanent magnet force model explains the underlying physics in achieving the magnetic plucking. Whereas the in-plane plucking configuration induces a jump phenomenon by creating a bifurcation, the out-of-plane plucking configurations rely on the speed of the moving magnet to resemble a narrow Gaussian function. The primary advantage of the out-of-plane plucking configurations is the capability of fabricating multiple piezoelectric beams on a single substrate to increase power density with lower assembly difficulty, which is especially useful in micro scale implementations.

To further study the dynamics of the magnetic plucking we derived a system level model incorporating a distributed parameter piezoelectric beam model and the analytical permanent magnet force model. A surface fitting technique can be applied to the 3 dimensional magnet force profile to reduce computation time. We developed a test setup to validate the model with a controlled excitation. In general, we have observed a good agreement between simulation and measurement. We extended the simulation to investigate the scaling relationship between power output and driving frequency. In-plane plucking and out-of-plane plucking exhibit different power vs. frequency profiles which indicates that a high-level optimization can be achieved by selection of the number and spacing of beams and magnets to implement an eccentric-rotor based frequency up-converting energy harvesting system.

Acknowledgements

This research is supported by National Science Foundation through the NSF Nanosystems Engineering Research Center (NERC) for Advanced Self-Powered Systems of Integrated Sensors and Technologies (ASSIST) under award number EEC 1160483. The authors would also like to thank Xiaokun Ma and Professor Chris Rahn at Pennsylvania State University for providing support on beam modelling.

References

- [1] M. El-hami, P. Glynn-Jones, N.M. White, M. Hill, S. Beeby, E. James, A.D. Brown, J.N. Ross, Design and fabrication of a new vibration-based electromechanical power generator, *Sens. Actuators A Phys.* 92 (2001) 335–342, [http://dx.doi.org/10.1016/S0924-4247\(01\)00569-6](http://dx.doi.org/10.1016/S0924-4247(01)00569-6).
- [2] S. Roundy, P.K. Wright, J. Rabaey, A study of low level vibrations as a power source for wireless sensor nodes, *Comput. Commun.* 26 (2003) 1131–1144, [http://dx.doi.org/10.1016/S0140-3664\(02\)00248-7](http://dx.doi.org/10.1016/S0140-3664(02)00248-7).
- [3] P.D. Mitcheson, T.C. Green, E.M. Yeatman, A.S. Holmes, Architectures for vibration-driven micropower generators, *J. Microelectromech. Syst.* 13 (2004) 429–440, <http://dx.doi.org/10.1109/JMEMS.2004.830151>.
- [4] S. Roundy, J. Tola, Energy harvester for rotating environments using offset pendulum and nonlinear dynamics, *Smart Mater. Struct.* 23 (2014) 105004, <http://dx.doi.org/10.1088/0964-1726/23/10/105004>.

- [5] A. Pantelopoulos, N.G. Bourbakis, A survey on wearable sensor-based systems for health monitoring and prognosis, *IEEE Trans. Syst. Man Cybern. Part C Appl. Rev.* 40 (2010) 1–12, <http://dx.doi.org/10.1109/TSMCC.2009.2032660>.
- [6] J.M. Donelan, Q. Li, V. Naing, J.A. Hoffer, D.J. Weber, A.D. Kuo, Biomechanical energy harvesting: generating electricity during walking with minimal user effort, *Science* (80-) 319 (2008).
- [7] P.D. Mitcheson, E.M. Yeatman, G.K. Rao, A.S. Holmes, T.C. Green, Energy harvesting from human and machine motion for wireless electronic devices, *Proc. IEEE* 96 (2008) 1457–1486.
- [8] P. Pillatsch, E.M. Yeatman, A.S. Holmes, A piezoelectric frequency up-converting energy harvester with rotating proof mass for human body applications, *Sens. Actuators A Phys.* 206 (2014) 178–185, <http://dx.doi.org/10.1016/j.sna.2013.10.003>.
- [9] T. Xue, X. Ma, C. Rahn, S. Roundy, Analysis of upper bound power output for a wrist-worn rotational energy harvester from real-world measured inputs, *J. Phys. Conf. Ser.* 557 (2014) 12090, <http://dx.doi.org/10.1088/1742-6596/557/1/012090>.
- [10] M. Pozzi, Magnetic plucking of piezoelectric bimorphs for a wearable energy harvester, *Smart Mater. Struct.* 25 (2016) 45008, <http://dx.doi.org/10.1088/0964-1726/25/4/045008>.
- [11] M. Pozzi, M.S.H. Aung, M. Zhu, R.K. Jones, J.Y. Goulermas, The pizzicato knee-joint energy harvester: characterization with biomechanical data and the effect of backpack load, *Smart Mater. Struct.* 21 (2012) 75023, <http://dx.doi.org/10.1088/0964-1726/21/7/075023>.
- [12] R. Lockhart, P. Janphuang, D. Briand, N.F. de Rooij, A wearable system of micromachined piezoelectric cantilevers coupled to a rotational oscillating mass for on-body energy harvesting, 2014 IEEE 27th Int. Conf. Micro Electro Mech Syst. (2014) 370–373, <http://dx.doi.org/10.1109/MEMSYS.2014.6765653>.
- [13] M. Hayakawa, Electronic Wristwatch with Generator, U.S. Patent No. 5, 001, 685, 19 Mar. 1991.
- [14] Kinetron, Micro Generator System 26.4, <http://www.kinetron.eu/wp-content/uploads/2015/01/MGS-26.4.pdf>, 2015 (Accessed 19.09.2016).
- [15] T. Xue, S. Roundy, Analysis of magnetic plucking configurations for frequency up-converting harvesters, *J. Phys. Conf. Ser.* (2015) 1–5, <http://dx.doi.org/10.1088/1742-6596/660/1/012098>.
- [16] G. Akoun, J. Yonnet, 3D analytical calculation of the forces exerted between two cuboidal magnets, *IEEE Trans. Magn.* MAG-20 (1984) 1962–1964, <http://dx.doi.org/10.1109/TMAG.1984.1063554>.
- [17] R. Ravaut, G. Lemarquand, S. Babic, V. Lemarquand, C. Akyel, Cylindrical magnets and coils: fields, forces, and inductances, *IEEE Trans. Magn.* 46 (2010) 3585–3590, <http://dx.doi.org/10.1109/TMAG.2010.2049026>.
- [18] H.S. Choi, L.H. Park, S.H. Lee, Force calculation of magnetized bodies in contact using Kelvin's formula and virtual air-gap, *IEEE Trans. Appl. Supercond.* 16 (2006) 1832–1835, <http://dx.doi.org/10.1109/TASC.2005.864335>.
- [19] J.S. Agashe, D.P. Arnold, A study of scaling and geometry effects on the forces between cuboidal and cylindrical magnets using analytical force solutions, *J. Phys. D Appl. Phys.* 42 (2009), <http://dx.doi.org/10.1088/0022-3727/42/9/099801>, 099801–099801.
- [20] L.H. De Medeiros, G. Reyne, G. Meunier, Comparison of global force calculations on permanent magnets, *IEEE Trans. Magn.* 34 (1998) 3556–3559, <http://dx.doi.org/10.1109/20.717839>.
- [21] P. Pillatsch, E.M. Yeatman, A.S. Holmes, Magnetic plucking of piezoelectric beams for frequency up-converting energy harvesters, *Smart Mater. Struct.* 23 (2014) 25009, <http://dx.doi.org/10.1088/0964-1726/23/2/025009>.
- [22] H. Allag, J. Yonnet, Coulombian model for 3D analytical calculation of the torque exerted on cuboidal permanent magnets with arbitrarily oriented polarizations, LDIA 2011, 8th Int. Conf. Linear Drives Ind. Appl. 2011 (2011) 1–5 <http://hal.archives-ouvertes.fr/hal-00608059>.
- [23] P. Elleaume, O. Chubar, J. Chavanne, Computing 3D magnetic fields from insertion devices, *Proc. 1997 Part. Accel. Conf. (Cat. No.97CH36167)* 3 (1997) 3509–3511, <http://dx.doi.org/10.1109/PAC.1997.753258>.
- [24] K.W. Yung, P.B. Landecker, D.D. Villani, An analytic solution for the force between two magnetic dipoles, *Magn. Electr. (Sep. 9)* (1998) 39–52, <http://dx.doi.org/10.1155/1998/79537>.
- [25] A. Erturk, D.J. Inman, Issues in mathematical modeling of piezoelectric energy harvesters, *Smart Mater. Struct.* 17 (2008) 65016, <http://dx.doi.org/10.1088/0964-1726/17/6/065016>.
- [26] M.A. Karami, J.R. Farmer, D.J. Inman, Parametrically excited nonlinear piezoelectric compact wind turbine, *Renew. Energy* 50 (2013) 977–987, <http://dx.doi.org/10.1016/j.renene.2012.07.037>.
- [27] A. Erturk, D.J. Inman, *Piezoelectric Energy Harvesting*, John Wiley & Sons, Ltd, Chichester UK, 2011, <http://dx.doi.org/10.1002/9781119991151>.

Biographies

Tiancheng Xue received his BEng degree in Mechanical Engineering from Huazhong University of Science and Technology (HUST), China in 2013. He is currently a PhD student at the Systems, Harvesting and Design Optimization (SHADO) lab in the Department of Mechanical Engineering, University of Utah. His research focus is inertial energy harvesting from human motion.

Shad Roundy received his PhD in Mechanical Engineering from the University of California, Berkeley in 2003. From there he moved to the Australian National University where he was a senior lecturer for 2 years. He spent the next several years working with startup companies LV Sensors and EcoHarvester developing MEMS pressure sensors, accelerometers, gyroscopes, and energy harvesting devices. In 2012, he re-entered academia joining the mechanical engineering faculty at the University of Utah. Dr. Roundy is the recipient of the DoE Integrated Manufacturing Fellowship, the Intel Noyce Fellowship, and was named by MIT's Technology Review as one of the world's top 100 young innovators for 2004. His current research interests are in harvesting energy for wireless sensors, particularly from vibrations, acoustics, and human motion, and in MEMS inertial sensing.

CHAPTER 5

DEVELOPMENT OF WRIST-WORN ROTATIONAL ENERGY HARVESTERS WITH OUT-OF-PLANE PLUCKED PIEZOELECTRIC TRANSDUCERS: PART I: ASTERISK-SHAPE THIN-FILM PIEZOELECTRIC ELEMENT

5.1 Introduction

In this project, the development of wrist-worn rotational energy harvester prototypes is done in close collaboration with researchers (primarily Dr. Hong Goo Yeo and Prof. Susan Trolier-McKinstry) from Pennsylvania State University (PSU). Specifically, Dr. Yeo is in charge of the thin-film PZT fabrication whereas the overall system design and integration is carried out at the University of Utah. More detailed work on the material side of this project can be found in Dr. Yeo's Ph.D. dissertation [1]. Below is a summary aiming to answer one paramount question: why thin-film PZT?

Piezoelectric energy harvesters for industrial applications predominantly utilize Commercial off-the-shelf COTS piezoelectric composite beams made with bulk ceramic PZT due to their high piezoelectric coefficient. These beams are quite thick ($> 250 \mu\text{m}$) and therefore stiff due to material fabrication limitations. As a result, their use often results in low space utilization in rotational structures for human applications as the inertial force is not likely to overcome an accumulated rigidity from multiple bulk beams. This low space utilization is reflected in the work by Pillatsch et al. [2], in which only one bulk PZT beam

(two 130 μm PZT layers with a 110 μm center shim) is placed in the device, occupying the full diameter in order to achieve the lowest possible stiffness. Polymer PVDF beams are more flexible, but they exhibit a substantially lower piezoelectric coefficient. For instance, the piezoelectric coefficient d_{31} of the PZT sheet (PSI-5A4E) made by Piezo Systems is -190 pm/V [3] whereas the PVDF film provided by TE Connectivity only shows -33 pm/V [4]. For wearable applications, thin-film PZT is manifestly the ideal choice for a multibeam implementation as it combines a high material figure of merit with a desired flexibility. For a piezoelectric transducer under repetitive strain cycles, the RMS power output from an impedance matched resistive load is given by

$$P_{rms} = \frac{\omega}{4} \left(\frac{e^2}{\epsilon_0 \epsilon^T} \right) (At) S^2 \quad (5.1)$$

where ω is the excitation frequency, e is the piezoelectric stress coefficient (d coefficient multiplied by Young's modulus c), ϵ_0 is the vacuum permittivity, ϵ^T is the free relative permittivity of the piezoelectric material, At is the volume of the piezoelectric material (area and thickness, respectively), and S is the zero to peak strain magnitude. The term in the parentheses is sometimes referred to as the energy harvesting material figure of merit (FoM). A desirable material should exhibit a high piezoelectric coefficient and a low permittivity.

In addition, the piezoelectric energy harvesting coupling coefficient k is often used to compare material properties. The square of k indicates the ratio of converted energy to input energy. For a cantilever operating in 31 (bending) mode, the coupling efficient is defined as

$$k_{31} = \sqrt{\frac{d_{31}^2 c_{11}}{\epsilon_{33}}} \quad (5.2)$$

Note that in some literature, the term $e_{31,f}$ is used instead of e_{31} . The subscript f denotes the zero-strain condition in the plane of the film, while being stress free out-of-the-plane [5]. The relationship between $e_{31,f}$ and d_{31} and the compliance s ($s = 1/c$) is given by

$$e_{31,f} = \frac{d_{31}}{s_{11} + s_{12}} \quad (5.3)$$

For thin-film PZT beams, given that the thickness of the substrate layer is usually much larger than the PZT layer, the power output approximately scales with the PZT volume At as the change in strain is not significant. Figure 5.1 further illustrates this in a plucking scenario with a simulation study on the theoretical optimal PZT ratio for a bimorph beam of fixed thickness. In this simulation, the piezoelectric beam is 10 mm in length and 3 mm in width with a proof mass of 28 mg. The material properties are defined using existing data of custom fabricated piezoelectric materials by PSU. The PZT thickness ratio $t_{\text{piezo}}/t_{\text{total}}$ is varied for a given total thickness of $50 \mu\text{m}$. The beam is subject to a

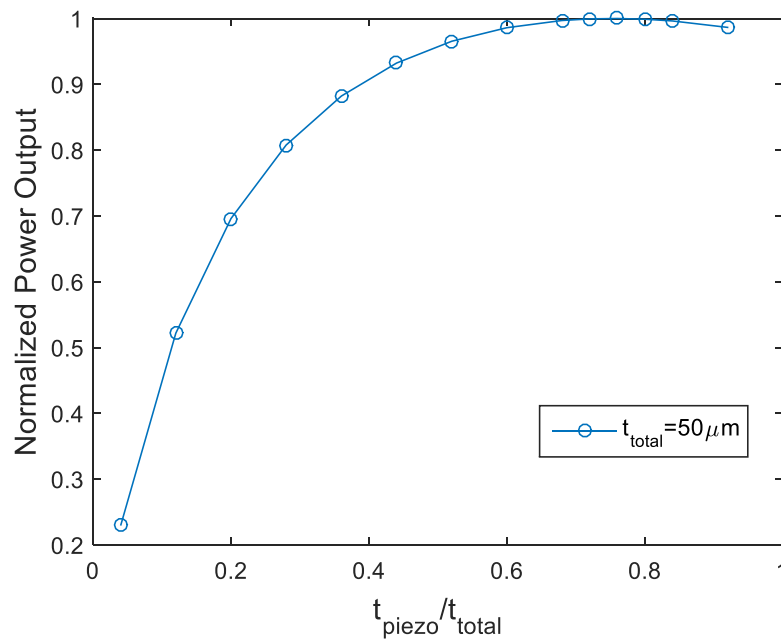


Figure 5.1. Simulated power output from a PZT/Ni/PZT bimorph with various PZT ratio.

plucking input of normalized initial velocity and the power output is computed using an optimal resistive load for each beam configuration. Based on Fig. 5.1, power output can be greatly improved in the region below the ratio of 0.4 whereas saturation occurs around the ratio of 0.6 for this particular case. Beyond that, a further increase in PZT thickness will be counterproductive due to the change in beam characteristics. This result indicates that for a beam with total thickness of 50 μm , an increase of power output by a factor of 4 can be achieved when the PZT layer thickness grows from 1 μm to 10 μm (since this is a bimorph, the corresponding ratio is 0.04 to 0.4). In reality, thicker PZT thin-films are prone to fracture during fabrication with either an additive method (i.e., thin-film deposition) or a subtractive method (i.e., bonding and grinding bulk PZT).

Nevertheless, the takeaway from this simulation agrees with the work in [6] where an experimental comparison is conducted using PZT/Ni unimorph beams with PZT thickness from 1 μm to 3 μm (on a 25 μm Ni substrate). Therefore, there is an incentive to grow thicker PZT films for energy harvesting purposes. As a matter of fact, a large portion of the research effort of our collaborators has been dedicated to grow thicker highly (001) oriented PZT films on metal foils. Metal foils are chosen due to their flexibility and high fracture strength compared to silicon. Nickel is one convenient option that exhibits a similar acoustic impedance to PZT, which may efficiently achieve interlayer strain transfer. One challenge for metal-based PZT deposition under high temperature is the difference in thermal expansion coefficients. However, by utilizing the thermal expansion of the metal layer (equivalently, the PZT film is under compression), the favored formulation of *c*-domain crystals leads to a lower permittivity [1], which is beneficial for improving power output as per Eq. (5.1). During our prototyping effort, the fabrication methods of chemical

solution deposition (CSD) [7] and high-temperature sputtering [6] have both been carried out and studied by Dr. Yeo and Prof. Trolrier-McKinstry, producing thick PZT thin-films of thickness up to $5.4 \mu\text{m}$ [8].

This chapter reports the first prototyping effort in a series of design iterations of implementing piezoelectric transducers within a rotational energy harvester architecture. The initial prototype applies the out-of-plane plucking configuration with an attempt to fabricate all the thin-film PZT beam on a single Ni substrate.

5.2 Design and Fabrication

The first prototype applies the out-of-plane indirect repulsive configuration (IRC) as illustrated in Fig. 4.2(d) for magnetic plucking. The overall design, as shown in Fig. 5.2, allows the fabrication of 6 piezoelectric beams on a single Ni substrate. N50 permanent magnet cubes (1.59 mm in length) are arranged both on the tip of the beams and in the rotor

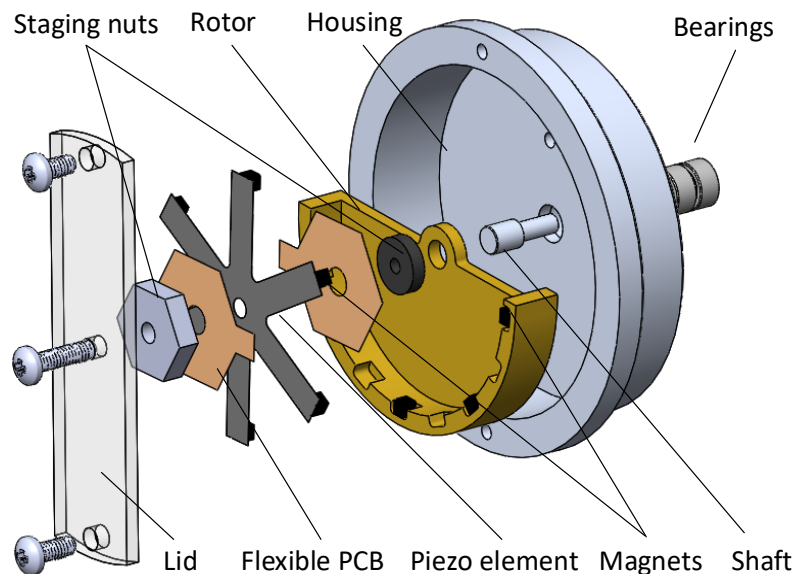


Figure 5.2. Exploded view of the harvester with asterisk-shape piezoelectric element.

slots. The eccentric rotor (16 mm in radius, brass) and the shaft (stainless steel) are supported by two ball bearings (Dynaroll SMR52ZZ A5). When the rotor moves as a result of human excitation, the piezoelectric beam will be plucked magnetically. The asterisk-shape piezoelectric element is sandwiched between two layers of flexible printed circuit boards for electrical signal extraction. Two staging nuts clamp the piezoelectric element, effectively creating 6 cantilever beams of 10 mm length and 3.6 mm width. This arrangement improves the space utilization compared to a single-beam device while minimizing the difficulty of a multibeam assembly. In addition, this design provides a feasible path for potential miniaturization using existing MEMS technologies.

The asterisk-shape piezoelectric element shown in Fig. 5.3 was laser cut from a PZT/Ni/PZT bimorph film fabricated by Hong Goo Yeo. It was found that laser cutting achieves a smaller damaged area on the edge compared to manual cutting by scissors. PZT films of 3 μm thickness were grown by *rf*-magnetron sputtering with postannealing on both sides of a 50 μm thick Ni foil (99.99%, made by Alfa Aesar). Platinum electrodes were patterned using standard lithography. Two flexible printed circuits made from a wet-etched copper coated polyimide (in collaboration with Israel Ramirez and Alex Tellado) were bonded onto both sides of the piezoelectric element with silver epoxy to access the electrodes. A photo of the asterisk-shape piezoelectric element with bonded printed circuits is given in Fig. 5.3. More details of the fabrication process can be found in Chapter 7 of [1].

Two layers of PZT were later poled in opposite directions for a series bimorph connection. Both high-temperature (HT) poling (150 $^{\circ}\text{C}$) and room-temperature (RT) poling were attempted. Five copies of samples were made over the course and the electrode

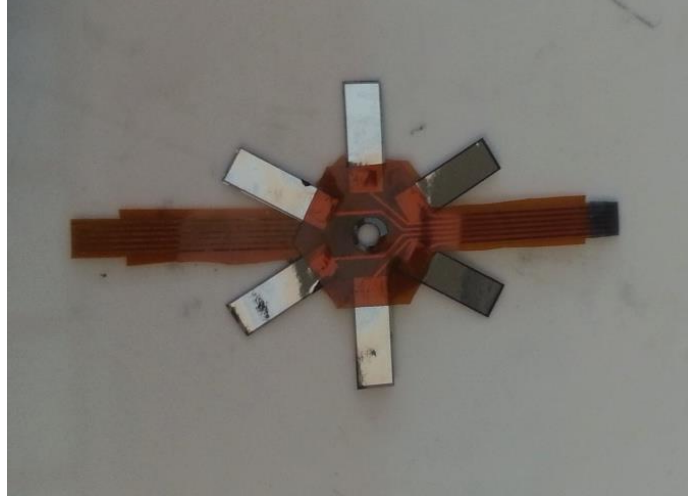


Figure 5.3. Asterisk-shape piezoelectric element bonded with flexible printed circuits.

yield ranges from 8.3% to 41.7%. It is likely that due to the large aspect ratio of the bimorph thin-film, some Pt electrodes partially undercoated to the backside of the beam, creating an electrical pathway. When one electrode is shorted to the Ni substrate, the beam becomes a *de facto* unimorph electrically.

Before the full assembly, the cube magnets were all glued at their corresponding locations. In this design, there is a 1 mm gap and a 0.5 mm offset between the pairing magnets, which limits the beam tip displacement within 1 mm as predicted in the simulation. In addition, there are 8 slots in the rotor to allow room for adjustment in terms of the number of magnets. The full prototype with asterisk-shape piezoelectric element is shown in Fig. 5.4. Four magnets were evenly placed in the figure and were later used in the following experiment. Two staging PCBs with zero insertion force (ZIF) connectors were placed on the rim of the housing for data acquisition.

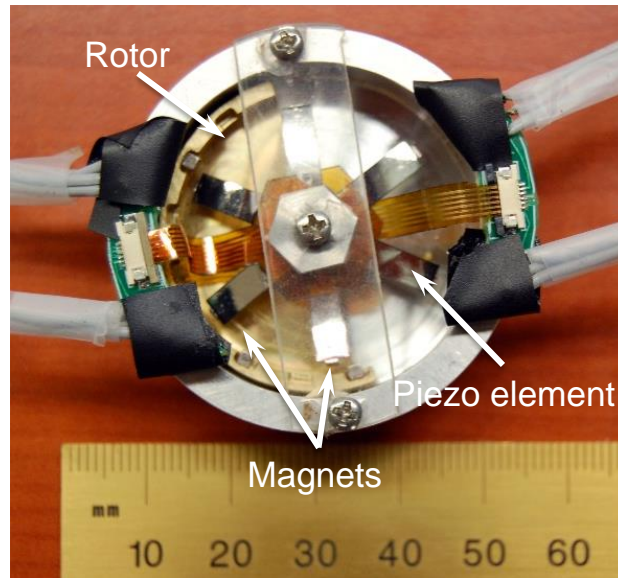


Figure 5.4. Assembled prototype with asterisk-shape piezoelectric element.

5.3 Experiment and Result

One of the thin-film PZT/Ni/PZT samples (HT poled) was used for a comprehensive material characterization. The relative permittivity ϵ_r was 328 and 346 for upper and lower layers, respectively. The transverse piezoelectric constant was evaluated as -12.1 ± 1.3 and -13.1 ± 1.0 C/m², respectively, for upper and lower layers. Again, the details of the material characterization can be found in Chapter 7 of [1]. As mentioned earlier, the thin-film PZT/Ni/PZT samples were all partially shorted. It was found that HT poling yielded a slighter lower (preferable) permittivity than RT poling. HT poled PZT layer (single) showed a capacitance between 27 to 30 nF whereas RT poled samples exhibited a capacitance anywhere between 30 to 32 nF. A 47 k Ω resistance was chosen as the impedance matched load for experimental characterization.

One of the observations concluded in the earlier literature review is that a standardized experimental characterization is lacking for evaluating wearable inertial

energy harvesters. In this work, a pendulum-based test set-up is proposed as the benchmarking tool that provides a pseudo walking excitation. The motor-controlled swing arm resembles the actual human arm in locomotion while maintaining simplicity and repeatability with its reduced degree of freedom. Figure 5.5 illustrates all the components of the test system. Note that the first test set-up built employed a radio-controlled (RC) hobby servo motor and a plastic arm (30 cm in length) and it was upgraded with a stepper motor and an aluminum arm (50 cm in length) in later prototyping characterizations (Chapters 6 and 7). In this characterization, the device under test (DUT) was screwed at the end of the swing arm to mimic a wrist-worn scenario. The motor projected sinusoidal trajectories with varying amplitudes and frequencies that correspond to different modes of real-world locomotion (e.g., slow walking).

Functioning individual PZT layers generated anywhere between 0.5 to 3.5 μW from a sinusoidal excitation of 120 degrees (± 60 degrees) at 1 Hz, which corresponds to a form of vigorous walking. There are two factors contributing to the postfabrication variation

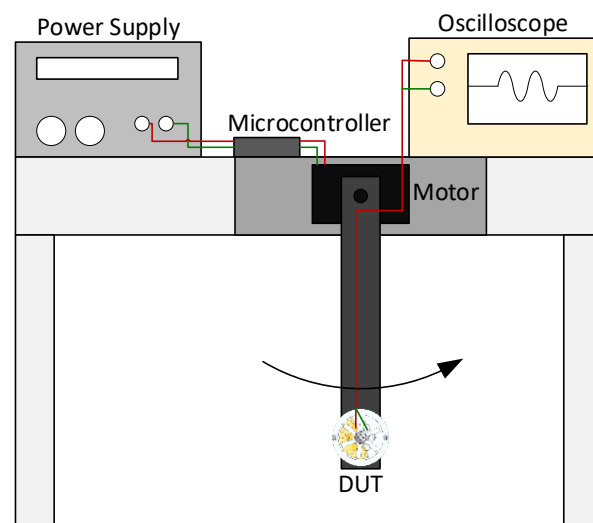


Figure 5.5. Swing arm test set-up [9].

among the beams: assembly tolerance (largely arisen from the inexact manual magnet alignment) and material degradation during handling. Nevertheless, based on the best performing PZT *de facto* unimorph, the prototype projected $42 \mu\text{W}$ power output assuming an ideal scenario where all beams are functioning and can perform as well as the current best one. A sample voltage output from one *de facto* unimorph beam across a $47 \text{ k}\Omega$ load is given in Fig. 5.6 where a directly usable voltage output (up to 3V) is demonstrated.

5.4 Conclusion

The first prototype serves mainly as a proof of concept for a wearable rotational energy harvester implementing multiple magnetically plucked thin-film PZT beams. The assembled prototype can generate up to $3.5 \mu\text{W}$ per unimorph from a vigorous pseudo walking input, projecting a total power output of $42 \mu\text{W}$ assuming all 12 piezoelectric

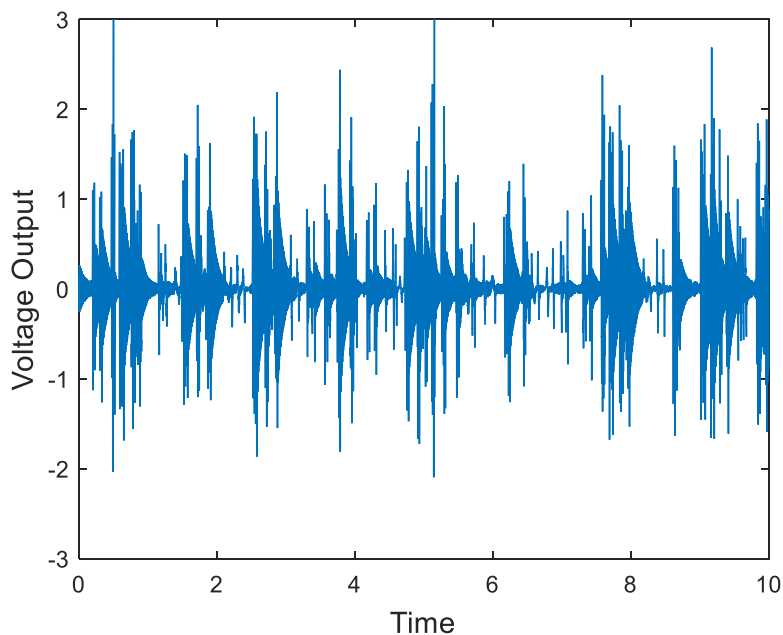


Figure 5.6. Sample voltage output of one *de facto* unimorph across $47 \text{ k}\Omega$ resistive load.

layers are functional. This validates the feasibility of the proposed approach despite some imperfections in material fabrication and prototype assembly.

Although the elegant design of a single substrate-based piezoelectric element reduces the assembly difficulty, it turned out to be at a greater cost of fabrication difficulty due to its irregular geometry. The low yield of poling resulted in insufficient functioning beams for proper characterization. Therefore, the next two iterations of designs (Chapters 6 and 7) employ individually cut piezoelectric beams in an attempt to achieve a higher yield.

Based on Eq. (5.1), the power output scales with the piezoelectric material volume for a controlled input. The primary motivation for the petal-shape design in the next chapter is to furtherly increase space utilization while maintaining the out-of-plane magnetic plucking configuration. The asterisk-shape design uses less than half of available area for piezoelectric materials. In the petal-shape design, piezoelectric beams are rearranged to be inward towards the rotating center with a trapezoidal shape. In addition, the in-plane magnetic plucking configuration is employed in Chapter 7 with an aim to increase the power output by implementing a stronger electromechanical coupling.

5.5 References

- [1] Yeo, H. G., 2017, "Mechanical Energy Harvesters Utilizing {001} Textured PZT Films on Flexible Metal Foils," Ph.D. Dissertation, The Pennsylvania State University, University Park, PA.
- [2] Pillatsch, P., Yeatman, E. M., and Holmes, A. S., 2014, "A Piezoelectric Frequency Up-Converting Energy Harvester with Rotating Proof Mass for Human Body Applications," *Sensors Actuators, A Phys.*, **206**, pp. 178–185.
- [3] Piezo Systems, "PSI-5A4E Piezoceramic Sheets and Plates" [Online]. Available: <http://piezo.com/prodsheet1sq5A.html>. [Accessed: 19-Mar-2018].

- [4] TE Connectivity, 2017, "METALLIZED PIEZO FILM SHEETS" [Online]. Available:http://www.te.com/commerce/DocumentDelivery/DDEController?Action=showdoc&DocId=Data+Sheet%7FMetallized_Piezo_Film_Sheets%7FA1%7Fpdf%7FEnglish%7FENG_DS_Metallized_Piezo_Film_Sheets_A1.pdf%7FCAT-PFS0003. [Accessed: 19-Mar-2018].
- [5] Trolier-McKinstry, S., and Muralt, P., 2004, "Thin Film Piezoelectrics for MEMS," *J. Electroceramics*, **12**(1/2), pp. 7–17.
- [6] Yeo, H. G., and Trolier-McKinstry, S., 2018, "Effect of Piezoelectric Layer Thickness and Poling Conditions on the Performance of Cantilever Piezoelectric Energy Harvesters on Ni Foils," *Sensors Actuators, A Phys.*, **273**, pp. 90–97.
- [7] Yeo, H. G., and Trolier-McKinstry, S., 2014, "{001} Oriented Piezoelectric Films Prepared by Chemical Solution Deposition on Ni Foils," *J. Appl. Phys.*, **116**(1), p. 14105.
- [8] Xue, T., Yeo, H. G., Trolier-McKinstry, S., and Roundy, S., 2017, "A Wrist-Worn Rotational Energy Harvester Utilizing Magnetically Plucked {001} Oriented Bimorph PZT Thin-Film Beams," *2017 19th International Conference on Solid-State Sensors, Actuators and Microsystems (TRANSDUCERS)*, pp. 375–378.
- [9] Xue, T., Ma, X., Rahn, C., and Roundy, S., 2014, "Analysis of Upper Bound Power Output for a Wrist-Worn Rotational Energy Harvester from Real-World Measured Inputs," *J. Phys. Conf. Ser.* **557** 012090, **557**(1), pp. 3–7.

CHAPTER 6

DEVELOPMENT OF WRIST-WORN ROTATIONAL ENERGY HARVESTERS

WITH OUT-OF-PLANE PLUCKED PIEZOELECTRIC TRANSDUCERS:

PART II: PETAL-SHAPE THIN-FILM PZT BEAMS

© 2017 IEEE. Reprinted, with permission from, T. Xue, H. G. H. G. Yeo, S. Trolier-McKinstry, and S. Roundy, “A wrist-worn rotational energy harvester utilizing magnetically plucked {001} oriented bimorph PZT thin-film beams,” in *2017 19th International Conference on Solid-State Sensors, Actuators and Microsystems (TRANSDUCERS)*, 2017, pp. 375–378.

A WRIST-WORN ROTATIONAL ENERGY HARVESTER UTILIZING MAGNETICALLY PLUCKED {001} ORIENTED BIMORPH PZT THIN-FILM BEAMS

Tiancheng Xue¹, Hong Goo Yeo², Susan Trolier-McKinstry² and Shad Roundy¹

¹University of Utah, Salt Lake City, USA and

²Pennsylvania State University, University Park, USA

ABSTRACT

A wrist-worn eccentric rotor-based energy harvester utilizing multiple magnetically plucked flower petal-shaped bimorph lead zirconate titanate (PZT) thin-film beams was designed and fabricated. The bimorph beams were formed by depositing {001} oriented PZT films up to 5.4 μm in thickness on both sides of a 50 μm thick nickel foil. The prototype was characterized with an analytical system-level model and a bench-top swing-arm test set-up. The prototype can achieve approximately 40 μW power output from a bench-top pseudo walking motion input. Further simulation suggests that improvement can be made by growing thicker PZT layers.

KEYWORDS

Energy harvesting, piezoelectric, wearable, frequency up-conversion, magnetic plucking,

INTRODUCTION

Energy harvesting for wearable wellness sensors provides the potential for continuous 24/7 health monitoring by eliminating the need to replace or recharge batteries. For healthcare, this enables mobility and may provide a safe alternative to hospital-based monitoring, whereas for consumer electronics it improves user experience by minimizing user intervention. Inertial energy harvesters are typically designed to be unidirectional and resonant at a particular frequency to take advantage of the peak dynamic magnification. However excitation from human motion exhibits low and irregular frequencies along multiple axes. Frequency up-conversion is a popular approach to address the issue by transforming the low-frequency excitation into a higher-frequency actuation of the transducer. In a typical implementation, a slower inertial mass plucks a piezoelectric cantilever beam and lets it ring down at its natural frequency; the piezoelectric converts mechanical to electrical energy. Compared to a translational proof mass, a rotational one without intrinsic motion limit caters better to a multidirectional input such as human motion.

Eccentric rotor-based energy harvesters utilizing plucked piezoelectric beams through either pins [1], [2] or magnetic coupling [3]–[5] have been demonstrated in the literature. Magnetic plucking provides better robustness and lower mechanical damping by eliminating mechanical contact compared to its counterpart. Commercial off-the-shelf bulk PZT beams are often used in existing prototypes. However the design space of a wrist-worn device generally allows only one bulk PZT beam due to its higher stiffness. Polyvinylidene fluoride (PVDF) beams are softer than bulk PZT beams but suffer from a poor piezoelectric figure of merit. PZT thin-film beams exhibit a similar amount of flexibility as PVDF beams without the

corresponding sacrifice in the piezoelectric properties. It is the ideal candidate for implementing multiple beams in one device to improve power density.

In this paper, a novel wrist-worn energy harvester architecture is proposed with flower petal-shaped beams prepared from PZT/Ni/PZT thin-film bimorphs. Typically piezoelectric beams are designed to be plucked in the plane of the proof mass motion whereas we previously introduced the concept of out-of-plane plucking (i.e., the beam is deflected orthogonal to the plane of proof mass motion) [6]. Out of plane plucking allows for more piezoelectric material without a significant increase in assembly difficulties in the proposed prototype.

DESIGN AND MODELING

Figure 1 illustrates the design of the proposed harvester in an exploded view. Six petal-shape bimorph PZT thin-film beams are mechanically clamped on the casing. The active length of the piezoelectric beam is 14.4 mm while the width is 3 mm and 15 mm at the tip and the base, respectively. The proposed petal shape not only improves the strain profile [7] but also fully utilizes the available area for sufficiently strained piezoelectric materials. The brass rotor is supported by two ball bearings. Tungsten weights are added to the outer rim of the rotor to increase mass and eccentricity which in theory increases the maximum potential power that can be generated [4]. Four cube NdFeB magnets (2mm \times 2mm \times 2mm) are evenly placed on the rotor. There are identical magnets attached on the tip of the six beams. This mismatch between rotor magnets and beam magnets is a deliberate arrangement to avoid synchronized beam plucking, which is likely to induce a large detent torque on the rotor that inhibits its continuous rotation, especially when the excitation is weak. The magnets are in a repulsive configuration along the direction of beam length with an intentional offset in the out of plane direction to realize the out-of-plane plucking [6].

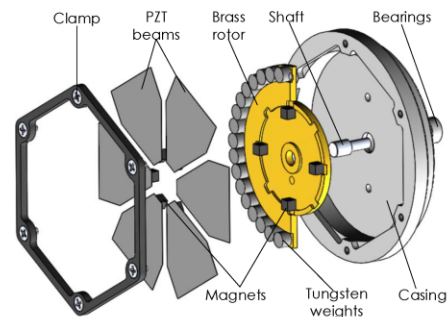


Figure 1: Exploded view of the rotational energy harvester with petal-shape bimorph PZT thin-film beams.

The model for the piezoelectric energy harvester is built upon a generalized rotational energy harvester model previously developed [4], where the transducer is modeled as a viscous damper. The motion of the rotor in a generalized rotational energy harvester constrained in its local plane is governed by

$$\ddot{\phi}_z = \frac{-(b_m + b_e)\dot{\phi}_z + mL[(\ddot{X} - g_x)\sin\phi - (\ddot{Y} - g_y)\cos\phi]}{I_g + mL^2} - \ddot{\theta}_z \quad (1)$$

where m , I_g and L are the mass, the moment of inertia about the center of mass and the eccentricity of the rotor respectively. \ddot{X} , \ddot{Y} and g_x , g_y are linear and gravitational accelerations to the casing, respectively in their local coordinates. θ_z denotes the angular displacement of the casing whereas ϕ_z denotes the relative angular displacement of the rotor with respect to the casing. A mechanical damper b_m and an electrical damper b_e are included in the model to represent lost and extracted energy, respectively. To model the proposed petal-shape piezoelectric energy harvester, the electrical damper was replaced with a magnetically plucked piezoelectric cantilever beam model [6]. Given that the system is not only nonlinear due to the trigonometric functions but also numerically stiff in the form of ordinary differential equations because of the implementation of the plucked beam model, the purpose of this model-based simulation is not to obtain an exact match in the time domain. As a matter of fact, the system is highly sensitive to initial conditions. However a good agreement in the average power output over a long period of time lends credibility to the proposed model.

FABRICATION AND ASSEMBLY

Bimorph beams were fabricated by depositing {001} oriented PZT films on both sides of a nickel foil (5cm × 5cm × 50μm). The continuous bimorph PZT films were grown by high temperature in-situ rf-magnetron sputtering with {100} textured LaNiO₃ (LNO) seed layer and HfO₂ buffer layer described in [8] and [9]. The cross section schematic of the PZT bimorph structure is shown in Figure 2. Strongly {001} oriented PZT films were deposited onto both sides of LaNiO₃/HfO₂/Ni/HfO₂/LaNiO₃ foils up to a thickness of 5.4 μm by sputtering at 550 ~ 585 °C from a 10% Pb excess Pb(Zr_{0.52}Ti_{0.48})O₃ target. No pyrochlore phase was detected in as-grown films by either X-ray diffraction or scanning electron microscopy.

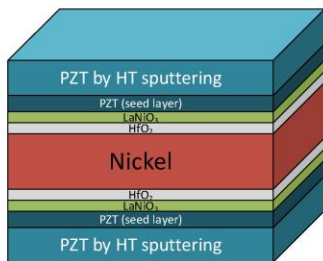


Figure 2: Cross section schematic of the bimorph structure.

A sol-gel PZT capping layer was deposited on top of the sputtered layers to decrease the surface roughness. Both PZT layers exhibited a relative permittivity of

approximately 450 with loss tangents less than 0.04 at 10 kHz. Highly {001} oriented PZT films showed well-saturated polarization – electric field hysteresis loops with large remanent polarizations (42 μC/cm²) at 100 Hz.

The fabrication and assembly process flow is illustrated in Figure 3. Platinum electrodes were patterned on the bimorph PZT films as demonstrated in Figure 3(b) by a standard lithography process. Petal-shape beams were cut with scissors after depositing electrodes by DC-magnetron sputtering on both sides. Wires were bonded onto both the electrodes and the center shim by silver paste and Kapton tape for electrical connection. The bimorph beams were hot poled in opposite directions for series connection before being assembled into the prototype. A high yield (~ 80%) was achieved for the large-area (>1 cm²) electrodes after using the resurrection treatment described in previous work [9]. Consequently, some beams are electrically functioning as unimorphs despite physically being bimorphs.

Due to the compliance of the polyoxymethylene clamp, the fastening was reinforced with cyanoacrylate as shown in Figure 4(d). To improve robustness six intermediate staging PCBs were placed on the casing as a stress relief for fine gauge wires attached to the PZT beams. Ribbon cable wires were used for final data acquisition.

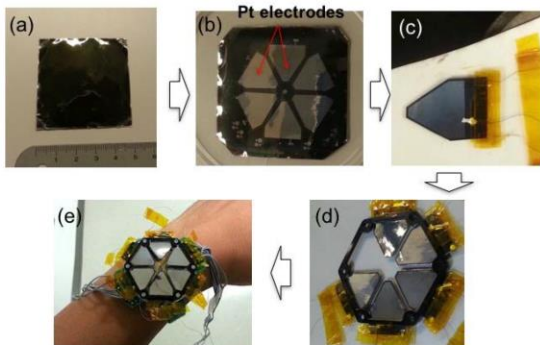


Figure 3: Fabrication and assembly process flow of the harvester prototype with bimorph PZT thin-film beams.

A photo of the fully assembled harvester prototype is given in Figure 4. The diameter of the prototype is 45 mm and the thickness is 8.5 mm, excluding the bearings.

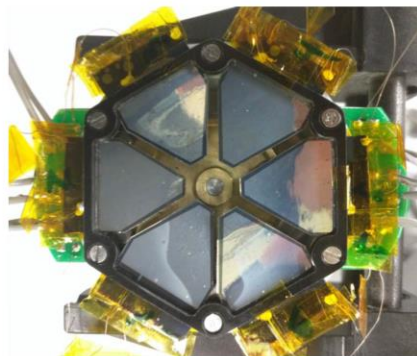


Figure 4: Photo of the assembled rotational energy harvester with bimorph PZT thin-film beams.

After assembly, all the beams maintained their previous integrity without any further damage. However not all the beams perform equally due to manufacturing variation and imperfect yield. In a more mature manufacturing operation, it is reasonable to assume that all beams would perform identically, given the evenly distributed magnet arrangement on the rotor. This assumption allows the simulations to be compared with measured performance by multiplying the power output of the best performing unimorph by 12 to obtain the total power output.

TESTING RESULTS

A bench-top motor controlled swing arm was built as the test set-up to characterize the prototype. As shown in Figure 5, the 50 cm long swing arm roughly mimics the upper limb in human locomotion. The motor creates varying motion profiles in a sinusoidal fashion with different amplitudes and frequencies as an approximation of various walking profiles.

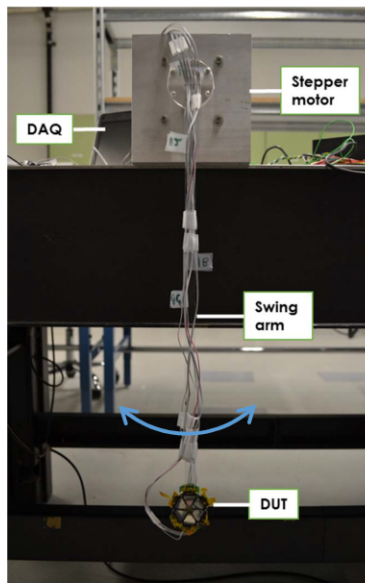


Figure 5: The swing arm test set-up with the prototype attached at the end.

Each beam was terminated with a matching load resistor of values 18 k Ω for de facto unimorphs, and a 33 k Ω for bimorphs. The sinusoidal excitation for characterization tests ranged from 30 to 60 degrees in amplitude and from 0.25 Hz to 1 Hz in frequency. The RMS power was calculated over 20 seconds and the initial power spike during operation was eliminated. As expected the variation among individual beams is significant due to differences in beam properties and assembly tolerances. Thus, the output power was calculated by multiplying the best performing unimorph by 12.

A comparison between simulation and measured power output is given in Figure 6. In the simulation a set of feasible initial rotor resting angles were applied to evaluate the effect of sensitivity to initial conditions on long term average power output. The error bars in Figure 6 represent

the minimum and maximum simulated power output based on 3 different initial conditions. The result suggests that model is stable in terms of predicting average power output over a long period of time. In general there is a good agreement between simulation and measurement with the simulated power being consistently lower. For instance, the measured power output from the excitation of $30 \sin 2\pi t$ results in a 41.8 μW and the simulated power output averages 37.6 μW . This discrepancy is likely due to the non-smoothness of the motion profile generated by the stepper motor. In fact the energy harvester benefits from any excess non-periodic excitation which is anticipated in a real wrist-worn situation.

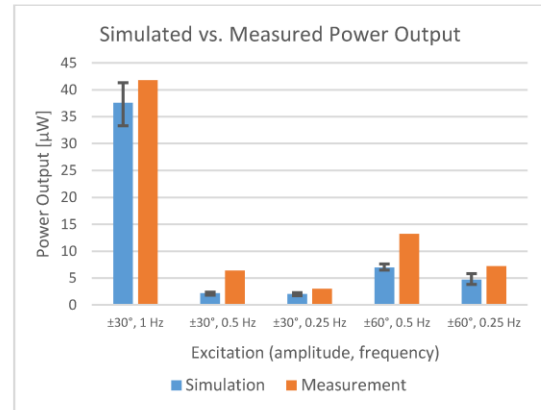


Figure 6: Simulated vs. measured power output from different excitations.

In addition to bench-top controlled experiments, the prototype was tested on the wrist of a human subject with a series of constrained motions including rotating the wrist and jogging in place. By holding the arm horizontally and rotating the wrist from -90° to $+90^\circ$ at approximately 1 Hz, the prototype generates 91.4 μW . In this case, gravitational excitation plays the primary role. A jogging-in-place excitation outputs 156.6 μW . Simply holding the prototype in hand and shaking it generates a similar amount of power. In both cases, the rotor goes into continuous rotation. This prototype was intended to be lightly coupled, i.e., it is targeting weak excitations such as walking or regular office routines. Thus, there is a saturation point for power output once the rotor goes to continuous rotation. Note that the calculations above are all based on the best unimorph assumption made earlier. A sample of instantaneous voltage and power output from one unimorph during an on-wrist test is given in Figure 7.

Further investigation into potential improvement can be done in simulation with the corroborated model. By maintaining the mechanical characteristics of the cantilever beam, a larger PZT to substructure ratio improves the power output since there is more piezoelectric material undergoing the same strain cycles. A bimorph beam with two 10 μm PZT layers will greatly improve the power output to 200 μW in simulation for the same excitation of $30 \sin 2\pi t$.

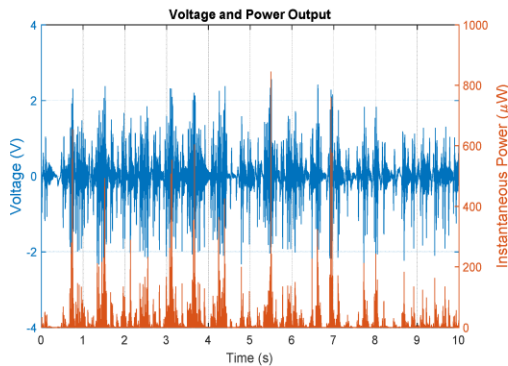


Figure 7: Sample instantaneous voltage and power output from one unimorph across a $27k\Omega$ resistor during an on-wrist test.

CONCLUSIONS

A wrist-worn rotational energy harvester utilizing magnetically plucked $\{001\}$ oriented bimorph PZT thin-film beams was designed, fabricated, and characterized. A state of the art $5.4 \mu\text{m}$ thick dense PZT layer on a nickel foil with a high piezoelectric figure of merit for energy harvesting was utilized. The prototype demonstrated approximately $40 \mu\text{W}$ power output from a bench-top pseudo walking input, which provides potential for a self-powered wearable wellness sensor.

ACKNOWLEDGEMENTS

This research is supported by National Science Foundation through the NSF Nanosystems Engineering Research Center (NERC) for Advanced Self-Powered Systems of Integrated Sensors and Technologies (ASSIST) under award number EEC 1160483.

REFERENCES

- [1] M. Pozzi, M. S. H. Aung, M. Zhu, R. K. Jones, and J. Y. Goulermas, "The pizzicato knee-joint energy harvester: characterization with biomechanical data and the effect of backpack load," *Smart Mater. Struct.*, vol. 21, no. 7, p. 75023, Jul. 2012.
- [2] R. Lockhart, P. Janphuang, D. Briand, and N. F. de Rooij, "A wearable system of micromachined piezoelectric cantilevers coupled to a rotational oscillating mass for on-body energy harvesting," *2014 IEEE 27th Int. Conf. Micro Electro Mech. Syst.*, pp. 370–373, 2014.
- [3] P. Pillatsch, E. M. Yeatman, and A. S. Holmes, "A piezoelectric frequency up-converting energy harvester with rotating proof mass for human body applications," *Sensors Actuators, A Phys.*, vol. 206, pp. 178–185, Feb. 2014.
- [4] T. Xue, X. Ma, C. Rahn, and S. Roundy, "Analysis of Upper Bound Power Output for a Wrist-Worn Rotational Energy Harvester from Real-World Measured Inputs," *J. Phys. Conf. Ser.*, vol. 557, p. 12090, Nov. 2014.
- [5] M. Pozzi, "Magnetic plucking of piezoelectric bimorphs for a wearable energy harvester," *Smart*

- [6] *Mater. Struct.*, vol. 25, no. 4, p. 45008, 2016.
- [7] T. Xue and S. Roundy, "On magnetic plucking configurations for frequency up-converting mechanical energy harvesters," *Sensors Actuators, A Phys.*, vol. 253, pp. 101–111, 2017.
- [8] S. Roundy, E. S. Leland, J. Baker, E. Carleton, E. Reilly, E. Lai, B. Otis, J. M. Rabaey, P. K. Wright, and V. Sundararajan, "Improving power output for vibration-based energy scavengers," *IEEE Pervasive Comput.*, vol. 4, no. 1, pp. 28–36, 2005.
- [9] H. G. Yeo and S. Trolier-McKinstry, "{001} Oriented piezoelectric films prepared by chemical solution deposition on Ni foils," *J. Appl. Phys.*, vol. 116, no. 1, p. 14105, Jul. 2014.
- [10] H. G. Yeo, X. Ma, C. Rahn, and S. Trolier-McKinstry, "Efficient Piezoelectric Energy Harvesters Utilizing (001) Textured Bimorph PZT Films on Flexible Metal Foils," *Adv. Funct. Mater.*, vol. 26, no. 32, pp. 5940–5946, Aug. 2016.

CONTACT

*T Xue, tel: +1-801-587-3180; tiancheng.xue@utah.edu

CHAPTER 7

DEVELOPMENT OF WRIST-WORN ROTATIONAL ENERGY HARVESTER WITH IN-PLANE PLUCKED BIMOPRH THIN-FILM PZT BEAMS

This chapter is a journal manuscript that has been submitted to *Smart Materials and Structures* and is currently under review.

7.1 Introduction

Energy harvesting is a promising alternative to batteries for powering long-term mobile health monitoring. The need to recharge batteries frequently undermines the user experience for many consumer electronics [1]. As the power consumption becomes a major obstacle to the emerging wearable market, various forms of energy harvesting from the body are being explored to reduce or eliminate battery changes [2]. Body motion, body heat, and breathing are all candidates to provide a continuous power supply; each methodology entails trade-offs in terms of available power and wearability. Based on the calculation of the “work” done, available power from human motion (on the order of Watts) is at least an order of magnitude higher than other sources [2]. However only a small portion of that energy can be actually exploited, as most of the mechanical work is produced and dissipated within the body itself. Walking, in particular, involves a cycle between kinetic energy and gravitational-potential energy to minimize chemical energy expenditure [3]. Nevertheless, harvesting inertial energy from human motion is interesting as the energy is readily accessible; other energy sources impose more requirements on environmental conditions [4–6]. For instance, thermal energy harvesting is improved when the thermoelectric is in good thermal contact to the skin and there is a continuous airflow over the device to maintain the temperature gradient [7]. These conditions undermine the general wearability of the devices.

Harvesting inertial energy from human motion entails a number of challenges. On one hand, due to the low and irregular frequency of human motion (usually around 1 Hz [8]), resonant harvesters operating at much higher frequencies cannot directly benefit from peak dynamic magnification. Moreover, human motion contains a high amount of

multiaxial movement with large displacement amplitude, whereas conventional translational harvesters are designed to be unidirectional allowing a small displacement amplitude.

Automatic self-winding watches are early successful exploitations in human-powered energy harvesting. The well-known Seiko Kinetic watch converts the kinetic energy of an eccentric rotor to electricity using a miniaturized electromagnetic generator [9]. Such eccentric-rotor-based rotational designs are propitious solutions to overcome the limitation of conventional linear harvesters, as a rotor can take advantage of excitations in all directions with no inherent motion limit. An early analysis on the rotational energy harvesting approach was presented in [10]. The slow and large proof mass motion is problematic, especially for electromagnetic energy harvesters, due to the need to boost the low voltages produced by slow rotation. In addition, it can be difficult to achieve the optimal level of electromechanical damping for small devices. The Seiko Kinetic watch implements a sophisticated high-ratio gear train to boost the speed, and hence the voltage, but it comes with a cost of higher mechanical damping in the form of friction from high-speed bearings [11].

Another strategy, which is often referred to as frequency up-conversion, is to excite a higher-frequency resonance in a transducer via a slower-frequency motion from environmental excitation. This strategy essentially enables a resonant oscillator to operate in a nonresonant fashion. Typically, the frequency up-conversion strategy is implemented in piezoelectric energy harvesters including impact-based operation [12–14], mechanical plucking via pins [15,16], and magnetic coupling [17–21]. Methods involving mechanical contact for the excitation usually suffer from reliability problems. Therefore, a noncontact

excitation such as magnetic coupling will be more suitable for long-term operation.

For piezoelectric transducers, contactless actuation through magnetic coupling is usually achieved by magnetically deflecting a piezoelectric cantilever beam and letting it ring down at its natural frequency. One of the first inertial wearable piezoelectric harvester prototypes was demonstrated in [20] using one bulk PZT beam with in-plane plucking, i.e., the beam deflects in the same plane as the moving magnet. An obvious solution to a higher power density is to implement multiple beams in one device. However, the design space of a wearable device tends to only allow one bulk PZT beam due to its higher stiffness. For example, the bulk PZT beam used in [20] is 370 μm in total thickness, which exhibits a resonance frequency of 400 Hz. A multibeam architecture with bulk PZT materials is more feasible in direct force (or torque) driven harvesters where the excitation can overcome the accumulated rigidity of the cantilever beams, such as the knee joint motion [18,22]. Polyvinylidene fluoride (PVDF) beams provide a superior flexibility but suffer from a poor piezoelectric figure of merit for energy harvesting [23]. Therefore, the ideal candidate for wearable applications is a PZT thin-film that combines flexibility with strong piezoelectric response. A mechanically plucked 4-beam piezoelectric energy harvester was proposed using silicon-based PZT unimorph beams [16]. However, the eventual prototype has only one beam. In this work, a 10-beam harvester architecture is proposed implementing custom fabricated bimorph PZT/Ni/PZT thin-film beams. The total thickness of the bimorph is around 60 μm and exhibits a resonance frequency of 150 Hz.

This paper extends a previous analysis on the theoretical power upper bound for rotational energy harvesters [24]. A generalized 3-dimensional eccentric-rotor-based energy harvester model was derived to provide an estimate of the maximum power output

from such harvester architectures regardless of the energy conversion mechanism. Artificial excitations constructed based on the characteristics of real-world human activities served as the inputs to the model. A previous study indicates that the upper bound on power generation from an eccentric-rotor-based harvester during normal activities is approximately an order of magnitude greater than what has been demonstrated by commercial electromagnetic generators [11]. The proposed prototype in this study is intended to narrow this gap by replacing the highly damped gearing system with the contactless magnetic coupling to up-convert the frequency. The implementation of multiple beams and magnets allows for tuning the system dynamics and optimization of the system electromechanical coupling based on more design variables from a system-level harvester model. For simplicity and repeatability, the proposed harvester prototype is characterized on a bench-top motor-controlled swing arm to approximately mimic the upper limb in locomotion.

7.2 Generalized Rotational Harvester Model

In order to provide an estimate of the maximum possible power generation from real-world multidimensional inputs, a full rotational harvester model in 3 dimensions is required. The planar rotational harvester model described in [10] only accounted for one rotational or linear excitation individually. This model was extended to 3 dimensions with 6 axial simultaneous inputs [24] as illustrated in Fig. 7.1. An electrical and a mechanical rotational damper are included in the model to represent extracted and lost energy respectively. The electrical damper represents any kind of ideal energy transducer and the mechanical damper represents a combined pathway for all kinds of energy losses (e.g.,

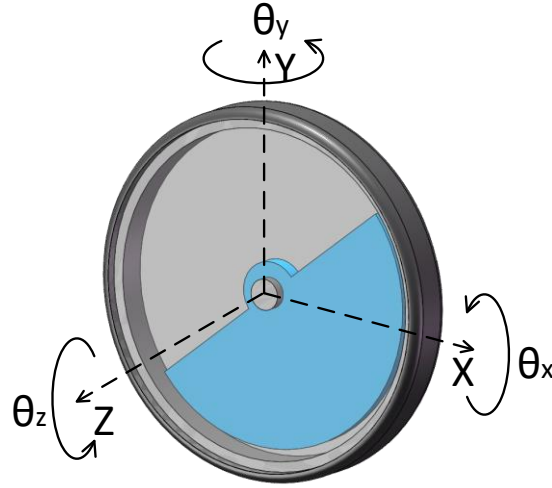


Figure 7.1. A generalized eccentric-rotor-based rotational energy harvester.

friction). As in many previous published studies [6,25], this model makes the assumption that the power dissipated through an optimal viscous damper that represents the electromechanical transducer is the maximum electrical power that can be extracted from the system. The motion of the rotor is constrained in the local 2D wrist frame as

$$m\ddot{\mathbf{x}} = \mathbf{F}_h + m\mathbf{g} \quad (7.1)$$

$$I_g\ddot{\psi}_z = T_d + (-\mathbf{L}) \times \mathbf{F}_h \quad (7.2)$$

where m , I_g , and \mathbf{L} are the mass, the moment of inertia about the center of mass, and the eccentricity vector of the rotor, respectively. \mathbf{x} and ψ_z are absolute linear and angular displacement of the rotor. \mathbf{F}_h is the force acted on the rotor from the housing via the shaft and T_d is the sum of all the damping torques with respect to the center of the rotor mass. The governing equations of the generalized rotational energy harvester (see the Appendix for the detailed Newtonian derivation) can be determined from Eq. (7.1) and (7.2) as:

$$m \begin{bmatrix} \ddot{X} - L\ddot{\psi}_z \sin \phi_z - L\dot{\psi}_z^2 \cos \phi_z \\ \ddot{Y} + L\ddot{\psi}_z \cos \phi_z - L\dot{\psi}_z^2 \sin \phi_z \end{bmatrix} = \begin{bmatrix} F_x \\ F_y \end{bmatrix} + m \begin{bmatrix} g_x \\ g_y \end{bmatrix} \quad (7.3)$$

$$I_g(\ddot{\phi}_z + \ddot{\theta}_z) = -(b_m + b_e)\dot{\phi}_z + F_x L \sin \phi_z - F_y L \cos \phi_z \quad (7.4)$$

Note that Eq. (7.3) was given with erroneous angular velocity and angular acceleration terms in [24] and has been corrected here. \ddot{X} , \ddot{Y} , and $\ddot{\theta}_z$ are linear accelerations (without gravitational components) and rotational excitation to the housing-rotor system, respectively. F_x , F_y , and g_x , g_y are the forces from the housing and the gravitational accelerations acting on the rotor, respectively, in each local coordinate. b_e and b_m are electrical and mechanical damping coefficients, respectively. ϕ_z denotes the relative angular displacement between the rotor and the housing, which determines the instantaneous power output as:

$$P = b_e \dot{\phi}_z^2 \quad (7.5)$$

Furthermore, the governing equation can be reduced to the following by analytically evaluating Eq. (7.3) and Eq. (7.4),

$$\ddot{\phi}_z = \frac{-(b_m + b_e)\dot{\phi}_z + mL[(\ddot{X} - g_x) \sin \phi_z - (\ddot{Y} - g_y) \cos \phi_z]}{I_g + mL^2} - \ddot{\theta}_z \quad (7.6)$$

The generalized rotational harvester model provides an estimate of the maximum power output in an ideal scenario in which the electromechanical coupling can be closely approximated by an optimal linear viscous damper and mechanical damping losses and parasitic electrical losses are neglected. This may seem counterintuitive as assuming $D_m = 0$ in a linear vibration energy harvester would result in an optimal D_e of almost zero with nearly infinite displacement and power output. In this rotational case, however, there is no resonant effect as there is no restoring spring. As a result, the optimal D_e is much higher than the implemented realistic D_m as observed in simulation. Real-world constraints such as the existence of mechanical friction and the need for power conditioning will certainly lower the obtainable power.

A pseudo walking motion in the form of a trajectory generated by a one-degree-of-freedom swing arm (i.e., motor-controlled pendulum) with length l_a was used as the input to the system. For a sinusoidal swing arm trajectory with an amplitude of α and a period of τ , the corresponding accelerative excitations are given by

$$\ddot{X} = -l_a \left(\frac{2\pi\alpha}{\tau} \right)^2 \cos^2 \left(\frac{2\pi t}{\tau} \right) \quad (7.7)$$

$$\ddot{Y} = -l_a \alpha \left(\frac{2\pi}{\tau} \right)^2 \sin \left(\frac{2\pi t}{\tau} \right) \quad (7.8)$$

$$g_x = g \cos \left(\alpha \sin \frac{2\pi t}{\tau} \right) \quad (7.9)$$

$$g_y = -g \sin \left(\alpha \sin \frac{2\pi t}{\tau} \right) \quad (7.10)$$

where the X axis is pointing down perpendicular to the ground. As shown in Fig. 7.2, the power output was found to be a function of the electrical damping coefficient and the eccentric rotor inertia. The optimal electrical damping is dependent on both the input excitation and the rotor inertia itself. In the simulation, D_m is set to be zero as described

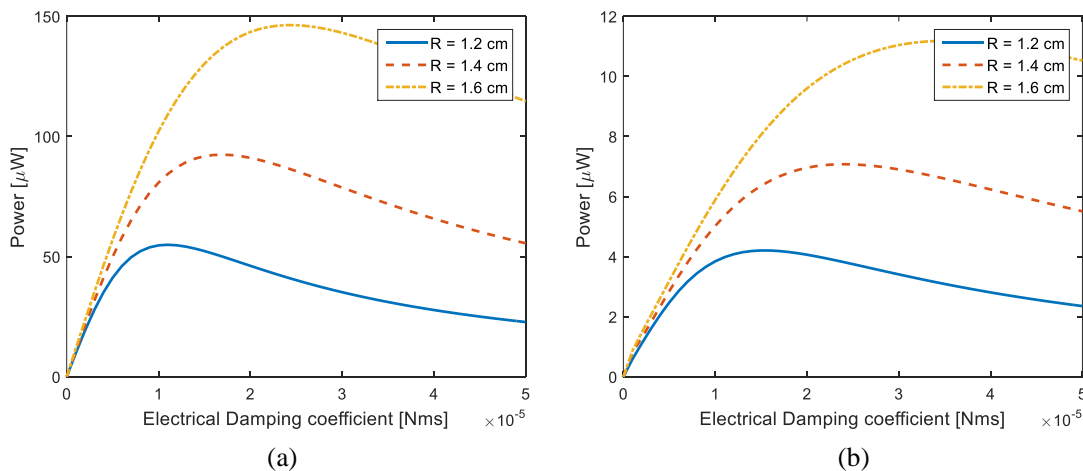


Figure 7.2. Calculated RMS power output as a function of electrical damping coefficient for different rotor inertia from a sinusoidal swing arm motion input: (a) amplitude = 12.5 degrees, period = 0.8 seconds, (b) amplitude = 12.5 degrees, period = 1.1 seconds.

earlier. For Fig. 7.2(a), the amplitude and the period of the input is 12.5 degrees and 0.8 seconds, respectively. The amplitude of linear excitations in both directions follows the inverse-square law with respect to the period. In addition, a smaller period leads to a larger number of pendulum swings per unit time. Thus, the power is greatly reduced when the period is increased to 1.1 seconds as shown in Fig. 7.2(b). For simplicity, the eccentric semicircular rotor is assumed to be made of brass with a 2 mm uniform thickness; thus, the eccentricity and the inertia are reciprocally determined. For a rotor with a 1.6 cm radius, the corresponding inertia about the center of mass is 796.2 g mm^2 . Note that in reality, a nonuniform thickness or a nonsemicircular shape can be applied to obtain an arbitrary eccentricity for a given inertia. A material with higher density such as tungsten can also be used for a larger inertia to increase the obtainable maximum power. Fig. 7.3 illustrates the theoretical maximum power output obtained at the optimal electrical damping coefficient from a series of swing arm motions with different amplitudes and periods that correspond to various walking profiles.

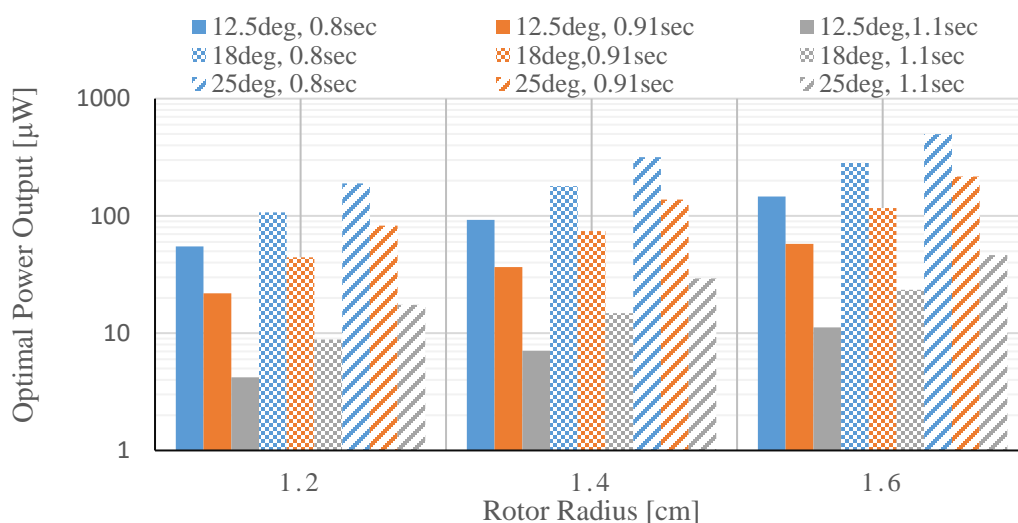


Figure 7.3. Upper bound on power generation for the generalized rotational harvester model from a sinusoidal swing arm motion input with different amplitudes and periods.

7.3 Multibeam Harvester Development

Magnetically actuated cantilever beams can be plucked in the plane or orthogonally out of the plane of the moving magnet. A comparison among different magnet configurations to achieve magnetic plucking [26] suggests that the primary advantage of out-of-plane plucking configurations in implementing a multibeam harvester lies in the manufacturability and associated difficulty in assembly especially when the device is miniaturized. For instance, a prototype utilizing a star-shape piezoelectric element with out-of-plane plucking in [21] demonstrated the feasibility of fabricating multiple bimorph PZT beams on a single substrate. Out-of-plane plucking configurations usually lead to light electromechanical coupling with high dependency on the speed of moving magnet. In-plane plucking configurations provide higher coupling due to their intrinsic bifurcation in the forcing profile, especially when the velocity of the moving magnet is low [26]. The bifurcation guarantees a dynamic ring down of the piezoelectric beam to efficiently extract energy from the system. However, when the inertial excitation is weak, a strong magnetic detent torque acting on the rotor tends to inhibit the device function. In this scenario, the moving magnet fails to drive the beam beyond the bifurcation point, and hence the rotor is caught between two beams. Nevertheless, at lower actuation frequencies, as in the case of wrist motion, the in-plane plucking configurations outperform out-of-plane configurations assuming the inertial driving torque surpasses the detent torque.

7.3.1 Design and Prototyping

The design of the rotational energy harvester utilizing magnetically plucked PZT thin-film beams is illustrated in Fig. 7.4. The eccentric rotor was fabricated out of brass

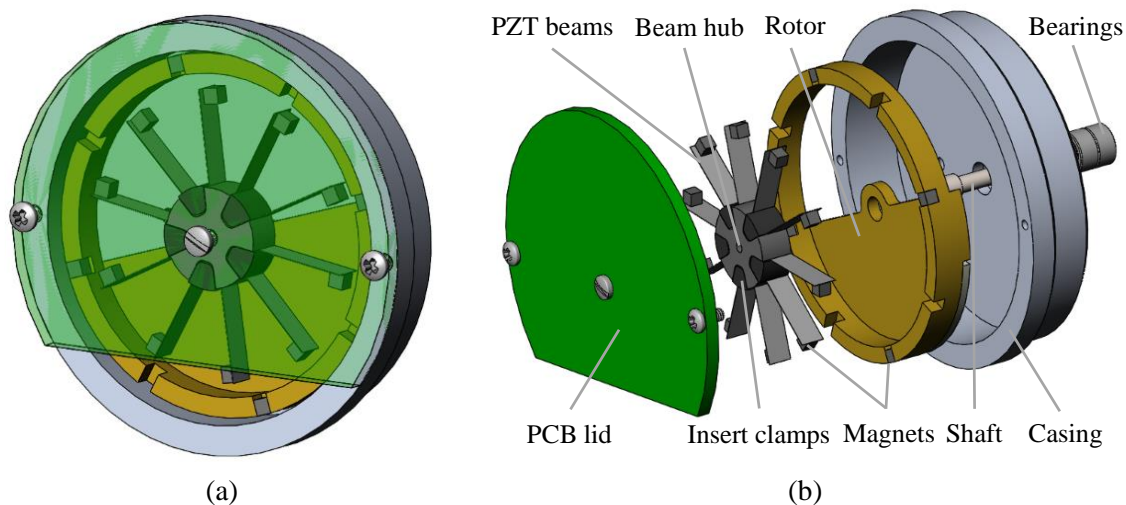
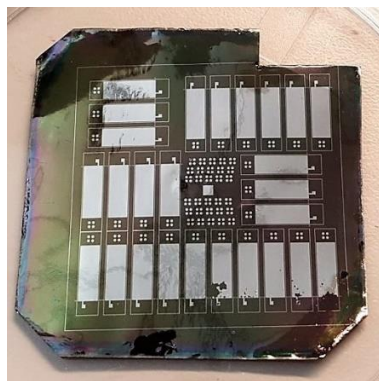


Figure 7.4. Rendering of the energy harvester (a) in assembly and (b) in an exploded view.

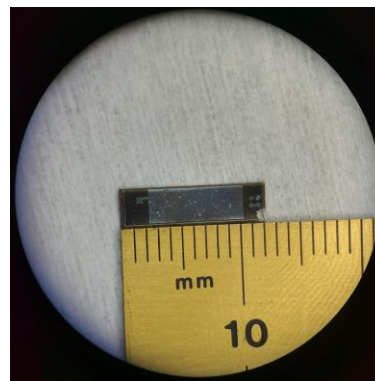
with an outer diameter of 36 mm. Tungsten weights were glued on the outer rim of the rotor to increase mass and eccentricity. The whole proof mass weighs 13 g with a 4.63 mm eccentricity and a 2663 g mm² moment of inertia at the center of mass. The rotor is supported by two ball bearings (SMR52ZZ) made by Dynaroll Corporation with dimensions of 2 mm × 5 mm × 2.5 mm. The corresponding diameter of the stainless steel shaft is 2 mm. Four neodymium N50 cube magnets with sides of length 1 mm were evenly placed and glued into the slots in the outer rim of the rotor. Note that the slots are designed to be open channels with 8 in total to allow changes in magnet arrangement in terms of size, numbers, and gap to tune the system in the future. A deliberate mismatch is arranged between magnets on the rotor and magnets on the beams to avoid synchronized plucking. The synchronization at the instance of initial beam deflection is likely to induce a large detent torque on the rotor, which, as mentioned earlier, restrains the rotor motion. This, however, means that each beam will require its own rectifier, which could reduce the overall efficiency of the power conditioning circuitry. Ten bimorph PZT thin-film beams

were mounted in the beam hub and fastened with insert clamps. The aluminum beam hub and insert clamps were anodized to provide electrical insulation. The printed circuit board (PCB) serves not only as the lid of the prototype, but also as a robust gateway to data acquisition.

Each cantilever beam is designed with a total length of 12 mm, out of which 2 mm is clamped within the hub. An N42 cube magnet with length 1.59 mm serves as the tip mass, which reduces the active length of the beam to approximately 9.21 mm. The magnets on the beam and the rotor are designed to be in a repulsive configuration with an air gap of 1.3 mm between magnets. The piezoelectric beams were fabricated by depositing {001} oriented PZT films on both sides of a 50 μm thick flexible nickel foil. The 5 μm thick continuous bimorph PZT films were grown by high temperature in-situ *rf*-magnetron sputtering with a LaNiO_3 (LNO) seed layer and a HfO_2 buffer layer described in [27,28]. The final prepared film with patterned platinum electrodes is shown in Fig. 7.5(a). Individual bimorph beams were cut and hot-poled in opposite directions for a series connection. The photo of a beam sample is given in Fig. 7.5(b).



(a)



(b)

Figure 7.5. Photo of (a) the PZT/Ni/PZT film with platinum electrodes and (b) one bimorph PZT/Ni/PZT thin-film beam.

The electrical connection is made through copper tapes placed on both the beam hub and the insert clamps. Silver epoxy was added onto the beam electrodes and cured for a robust connection. Wires were soldered to the copper tapes for connection to the PCB. The copper tape has a nonconductive adhesive and is reinforced with cyanoacrylate due to its exposure to high temperature during soldering. Photos of the prototype assembly are given in Fig. 7.6. The jumper switch on the PCB can reroute one beam's output to light up a light-emitting diode (LED) from the ribbon cable connectors. Although the beams were both mechanically and electrically intact before assembly, the increase of measured capacitance of a few beams afterwards indicates a short between sandwiched layers in the beam, possibly due to excessive silver epoxy. For an individual beam, if only one electrode is shorted to the nickel shim, the beam electrically becomes a de facto unimorph; if both are shorted, then no power will be generated. Nevertheless, the change in electrical domain from an individual beam is unlikely to alter the overall mechanical dynamics of the system, and thus the power output from other functional beams can be treated as unaffected.

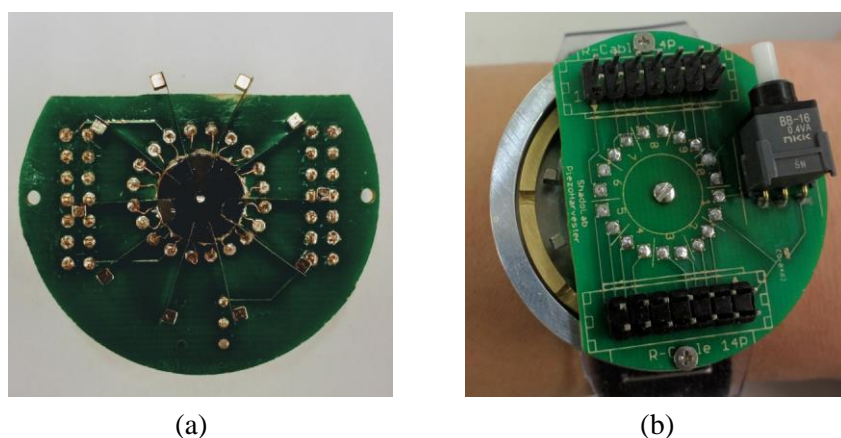


Figure 7.6. Photo of (a) the assembled beams in the hub and (b) the assembled prototype worn on the wrist.

7.3.2 Modeling

In order to model the system, the generalized rotational harvester model needs to be augmented with a magnetically plucked piezoelectric beam model. Many researchers have developed different approaches to formulate mathematical models for piezoelectric cantilever beams. The beam model adopted in this work has been derived in our previous work [26]. It is based on the distributed parameter model presented in [29] with a different forcing function in the form of magnetic force on the tip instead of a base excitation. Similar modeling procedures can also be found in [30]. An analytical Coulombian model was applied to calculate the force between cube permanent magnets [31] for improved accuracy as the distance between magnets is on the same order of magnitude as the dimension of magnets themselves.

The governing equation of the piezoelectric beam is given by

$$\begin{aligned}
 YI \frac{\partial^4 w(x,t)}{\partial x^4} + c_s I \frac{\partial^5 w(x,t)}{\partial x^4 \partial t} + m \frac{\partial^2 w(x,t)}{\partial t^2} + \left[M_t \frac{\partial^2 w(x,t)}{\partial t^2} + I_t \frac{\partial^3 w(x,t)}{\partial x \partial t^2} \right] \delta(x-l) \\
 + c_a \frac{\partial w(x,t)}{\partial t} - \vartheta_s v(t) \left[\frac{d\delta(x)}{dx} - \frac{d\delta(x-l)}{dx} \right] = F_m(t) \delta(x-l) \quad (7.11)
 \end{aligned}$$

In the equation above, $w(x,t)$ is the transverse displacement of the beam. M_t and I_t are the mass and the mass moment of inertia of the proof mass, respectively. YI and l are the effective bending stiffness and the active length of the beam, respectively. c_s and c_a are the strain rate and viscous air damping coefficients, respectively. ϑ_s is the backward coupling term for a bimorph beam connected in series. $F_m(t)$ is the transverse force acting on the proof mass as a result of the magnetic coupling. $\delta(t)$ denotes the Dirac delta function. The coupled electrical circuit equation for a bimorph in the series connection is given by

$$\frac{c_p}{2} \frac{dv(t)}{dt} + \frac{v(t)}{R_l} + i_p(t) = 0 \quad (7.12)$$

where C_p and i_p are the internal capacitance and the corresponding current source term for one piezoelectric layer. $v(t)$ is the output voltage from the bimorph beam in the presence of a load resistance R_l .

With the introduction of the magnetically plucked piezoelectric beams in the model, the electrical damping term in the governing equation for the rotor can be replaced with the corresponding magnetic coupling as well,

$$\ddot{\phi}_z = \frac{-b_m \dot{\phi}_z + mL[(\ddot{X} - g_x) \sin \phi_z - (\ddot{Y} - g_y) \cos \phi_z] + T_m}{I_g + mL^2} - \ddot{\theta}_z \quad (7.13)$$

where T_m is the sum of the magnetic torques.

In addition, relationships between the rotor displacement and the distance between each magnet pair are established with basic trigonometric approximation. The magnetic coupling is calculated based on the distance between magnets, which results in a Gaussian-like function with respect to the rotor path as the rotor magnet passes one beam [26]. The entire system consists of 32 state variables from 10 piezoelectric beams and one eccentric rotor. It can be solved numerically in the time domain with proper inputs such as the sinusoidal swing arm motion mentioned earlier. Due to the intricate rotor-beam interaction, the system exhibits a strong dependence on initial conditions with high nonlinearity. Consequently, it is unlikely to obtain an exact match between simulation and measurement in the time domain. Nevertheless, the model should be able to predict the average power output over a long period of time after eliminating the effect of initial conditions.

7.4 Experiment

7.4.1 Experimental Set-up

As stated earlier, the chosen input for this study is a pseudo walking motion in the form of a sinusoidal one-degree-of-freedom swing arm trajectory. This artificial input carries some of the upper limb characteristics from real-world locomotion with the capability to provide rotational and accelerative excitations simultaneously. In addition, its simplicity and repeatability allow the prototype to be easily characterized against the model for corroboration.

A bench-top motor-controlled swing arm was built to replicate a pseudo walking motion. As shown in Fig. 7.7, the 50 cm long aluminum arm roughly mimics the human upper limb. The microstepping-enabled stepper motor creates varying motion profiles in a sinusoidal fashion with different amplitudes and periods as an approximation of various

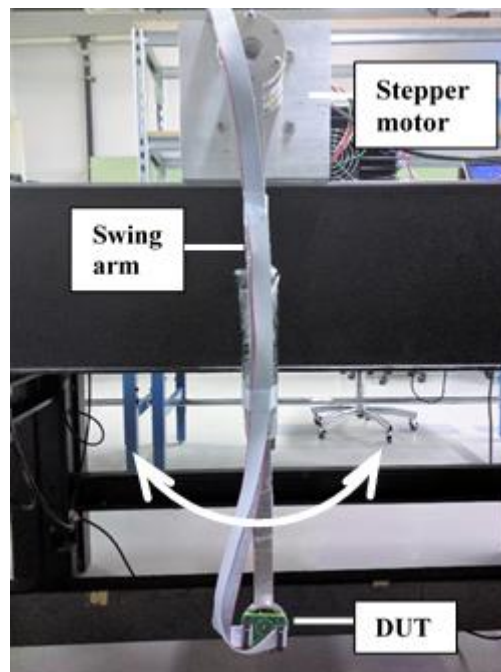


Figure 7.7. Photo of the swing arm test set-up with the prototype attached at the end.

walking profiles. The prototype was characterized with all the motion profiles applied earlier in the simulation of the generalized rotational harvester model. Each beam is terminated with a load resistor and the data acquisition is carried out with a PC oscilloscope.

7.4.2 Experimental Results

A separate beam validation test was conducted beforehand in which the beam was manually deflected at the tip and released to undergo a damped oscillation. The tip displacement (via a laser displacement sensor) and the open circuit voltage output were measured simultaneously. Whereas the permittivity was calculated from the measured capacitance, the piezoelectric coefficient d_{31} can be obtained by matching the simulation to the measurement. For the particular beam shown in Fig. 7.8, the d_{31} is characterized as -28 pC/N. Overall, the d_{31} of the beams distribute in a range from -25 to -35 pC/N. The low values for the effective piezoelectric coefficients are believed to be a result of defects

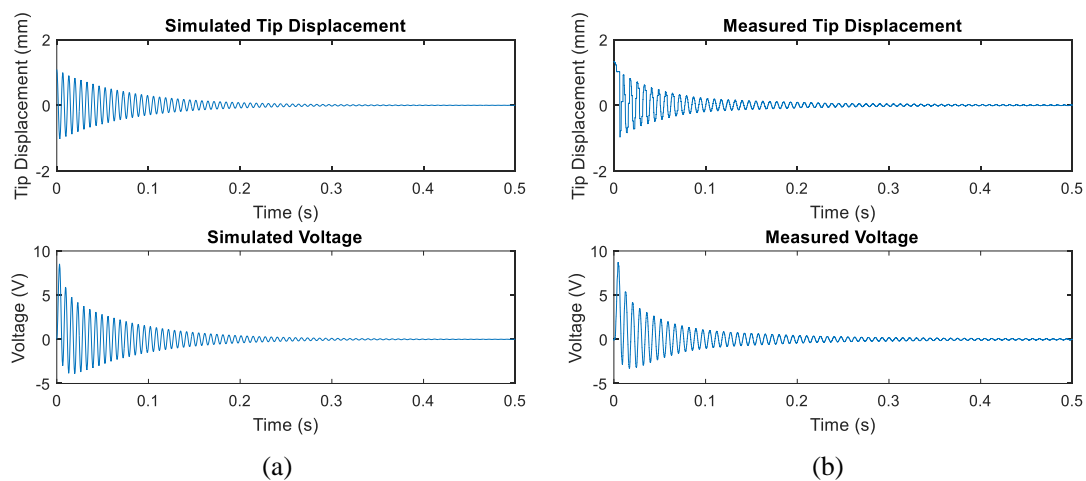


Figure 7.8. Individual beam validation of damped oscillation:
(a) simulation vs. (b) measurement.

induced during the poling and device assembly, along with variations in the initial beam curvature due to handling. In addition, the damping ratio of the cantilever beam can be determined via the logarithmic decrement method. These parameters will be fed back to the system level model. A detailed list of parameters for the piezoelectric beam used in simulation is given in Table 7.1.

Figure 7.9(a) gives an example of measured voltage output from one beam with a 150 k Ω resistive load under the sinusoidal swing arm excitation with a 25-degree amplitude and a 0.8-second period. A close-up view with two beam plucks is given in Fig. 7.9(b). A shift in polarity of the initial peak voltage indicates the change in plucking direction. By

Table 7.1. Parameters for the bimorph PZT/Ni/PZT beam

Parameter	Symbol	Value
Active length	l	9.2 mm
Width	b	3.0 mm
Thickness of Ni layer	h_s	50 μm
Thickness of PZT layer	h_p	5 μm
Density of Ni	ρ_s	8900 kg m ⁻³
Density of PZT	ρ_p	7500 kg m ⁻³
Young's modulus of Ni	Y_s	200×10^9 N m ⁻²
Young's modulus of PZT	\bar{c}_{11}^E	70×10^9 N m ⁻²
Piezoelectric coefficient	d_{31}	-30×10^{-12} m V ⁻¹
Capacitance of PZT layer	C_p	12 nF
Load resistance	R_l	150 k Ω

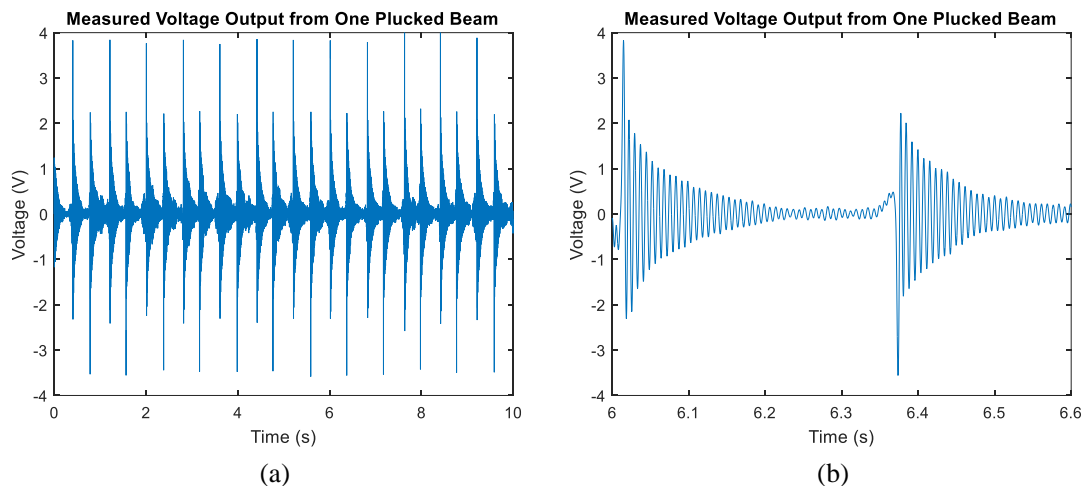


Figure 7.9. Measured voltage output from one beam during operation: (a) in 10 seconds and (b) in a close-up view.

examining the measured waveforms, all the beams exhibit a resonant frequency between 130 Hz and 155 Hz whereas the model indicates 150 Hz, which is reasonably good agreement given the variation in beam properties (e.g., resting curvature and electrode/hole distribution) and mounting conditions.

The prototype demonstrates a significant beam to beam variation in terms of power output although the piezoelectric coefficients are close among all the beams. This variation is likely due to inaccuracies in assembly, especially the gap between magnets, which governs the maximum strain in the beam and its voltage output via the piezomagnetoelastic coupling. The potential differences in degradation among the beams during assembly and testing could also contribute to the variation as well. Therefore, parameters are evaluated as an average value among all beams for simulation to be compared with measured result on a system level. The optimal load resistance has been identified as 150 k Ω for most beams, which corroborates the impedance match based on the measured capacitance of 7 nF per bimorph on average.

The total power output from a series of sinusoidal swing arm excitation is given in Fig. 7.10. The simulated power output is multiplied by a factor of 0.9. This is to achieve a fair comparison with simulation as one beam out of 10 is shorted in the prototype. Note that the excitation of 18 degrees and 0.91 seconds generates no power. As a matter of fact, the harvester does not function in either simulation or experiment under any weaker excitation, including the excitation of 12.5 degrees and 0.91 seconds, and all 3 excitations with a period of 1.1 seconds. In those scenarios, the excitation is not strong enough to overcome the magnetic detent torque and to push the rotor through the bifurcation point of the first beam to be plucked. Consequently, the rotor is trapped between two beams and does not produce any power. For stronger excitations, the power output generally scales with the intensity of the excitation. A total power output of approximately $40 \mu\text{W}$ can be generated from the excitation of 25 degrees and 0.8 seconds, which can be seen as a pseudo fast walking profile.

Note that the d_{31} of -30 pC/N does not represent the optimal performance of such

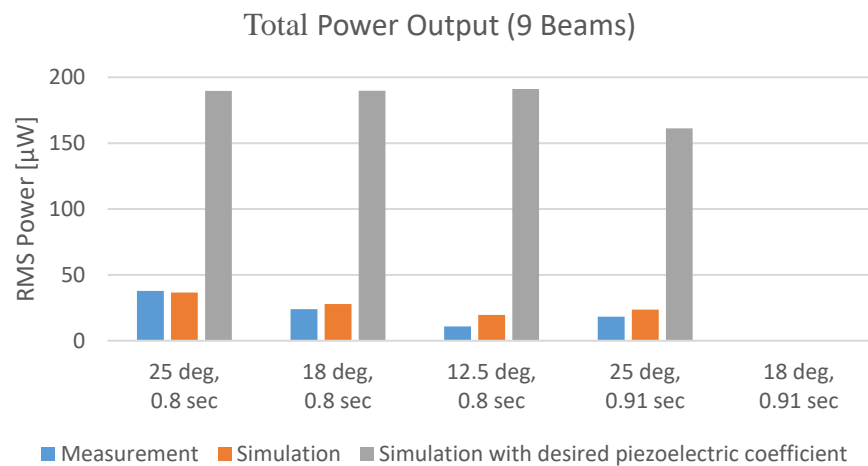


Figure 7.10. Average RMS power output per beam under different excitations from measurement and simulation.

PZT material. Previous fabrications indicate a d_{31} of up to -110 pC/N can be achieved from the sputtered high-density PZT thin-films [21] (for reference, commercial bulk PZT exhibits higher d_{31} , e.g., -190 pC/N from PSI-5A4E by Piezo Systems [32]). Thus, a simulation with a higher piezoelectric coefficient of 110 pm/V was conducted as well to investigate the potential of such architecture with improved material properties. In the simulation with the higher d_{31} , the 3 excitations with a period 0.8 seconds generate a total power output of roughly $230 \text{ }\mu\text{W}$ consistently (assume 10 functioning beams) whereas the excitation of 25 degrees and 0.91 seconds generates slightly less power output. This is different from the power scaling with the lower d_{31} value where the power output decreases as the excitation is reduced. The discrepancy in power scaling between different piezoelectric coefficients can be interpreted with a potential-well analogy, which is conceptually illustrated in Fig. 7.11. Fig. 7.11(a) corresponds to the blue and orange bars with lower d_{31} whereas Fig. 7.11(b) corresponds to the grey bar with higher d_{31} . The apparent damping torque experienced by the rotor is conceptually plotted against the

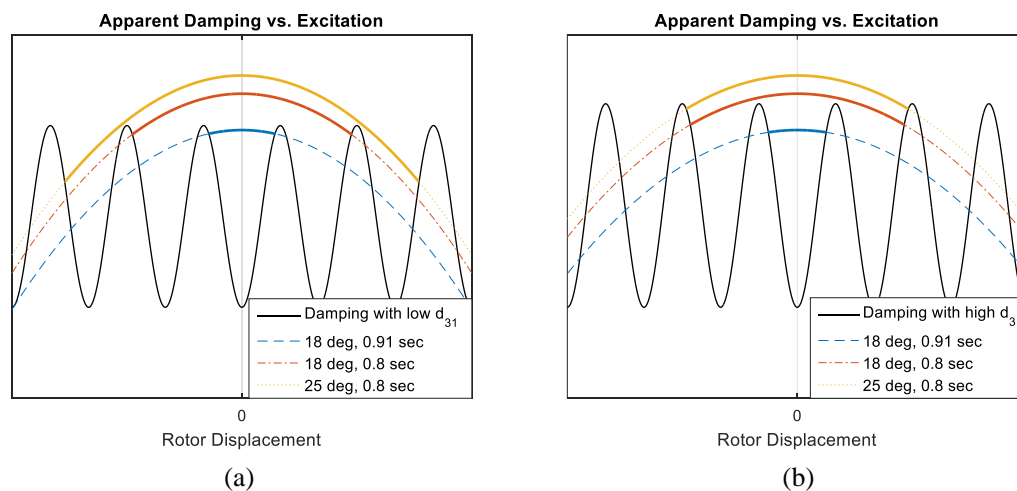


Figure 7.11. Characteristics of the piezoelectric harvester with a potential-well analogy.

excitation torque produced by the sinusoidal swing arm motion on the linear map of rotor displacement in a quasi-static fashion. On one hand, the total apparent damping consists of both the frictional mechanical damping from the bearings and the electrical damping imposed by the electromechanical coupling from the PZT bimorph, the latter of which is location dependent due to the discrete existence of piezoelectric beams. On the other hand, the excitation torque is the largest when the arm is pointing down to the ground and decreases as the arm moves up sidewise. As observed in both simulation and experiment, after the initial transient period with a cold start, the rotor will eventually go into a periodic oscillation that tracks the sinusoidal swing arm excitation in steady state. Thus, the excitation torque can be qualitatively plotted as a concave function of the rotor displacement as well. Fig. 7.11 visually illustrates the failure points (the boundary between solid lines and dotted lines) where the excitation torque fails to overcome the apparent damping torque, which correspond to the steady-state rotor displacement limit in the dynamic simulation.

A potential well is established by two local maximum damping points described by the system, which constrains the rotor motion. Each beam imposes a local maximum damping at its location where the rotor needs to overcome the magnetic detent torque. It has been shown that the energy produced per pluck for one beam is more or less consistent, with only marginal improvement with respect to the increase in the proof mass velocity [26]. This indicates that the total power output can be seen as a measurement of the number of plucks, which is determined by the rotor displacement limit per cycle per unit time. Therefore, a more distant potential well from the zero-displacement point grants a higher achievable power output for a given driving frequency. Note that the potential wells are

higher in Fig. 7.11(b) than in Fig. 7.11(a) due to a higher piezoelectric coefficient d_{31} . Consequently, the same excitation is not necessarily trapped in the same potential well. For instance, the excitation of 25 degrees and 0.8 seconds jumps into the third potential well in Fig. 7.11(a), whereas it is trapped in the second potential well in Fig. 7.11(b) due to an increased apparent damping. The excitation of 18 degrees and 0.91 seconds falls into the potential well at zero displacement in both cases, indicating that the rotor motion is constrained between the adjacent two beams and no power is produced. Qualitatively, this agrees with the results in Fig. 7.10.

The potential-well analogy illustrates a staircase function-like system response to a sinusoidal swing arm excitation in terms of power output. There is an excitation threshold for the harvester to function governed by the mechanical damping and the electromechanical coupling. An inherent trade-off exists between the function threshold and the maximum achievable power. A smaller mechanical damping will certainly lower the threshold to function. Given the same mechanical damping, a prototype capable of functioning under weaker excitation will suffer from a lower saturation power due to its associated weaker electromechanical coupling. Nevertheless, the system can be tuned with respect to its electromechanical damping to approach optimal power output for a given input. This can be easily achieved by adjusting the magnet configuration, i.e., the gap between and the size of magnets. Furthermore, by comparing the simulated power output with $d_{31} = -110 \text{ pC/N}$ to the theoretical power upper bound, it is clear that among excitations with a period of 0.8 seconds, the design with higher electromechanical coupling is more effective [33] towards the excitation of 12.5 degrees, achieving a higher ratio of generated power to theoretical limit. The generalized rotational harvester model predicts a theoretical

upper bound power output of 1419 μW and 424 μW for the excitation of 25 degrees and 12.5 degrees with the period of 0.8 seconds, respectively, for the same rotor inertia. However, the actual plucked piezoelectric beam harvester can produce 230 μW for each of these excitations.

7.5 Conclusions

This paper presents a wearable inertial energy harvester utilizing a rotational proof mass and magnetically plucked piezoelectric beams, which specifically caters to harvesting energy efficiently from human motion. Compared to commercial electromagnetic energy harvesters such as the Seiko Kinetic watch, a frequency up-converting piezoelectric harvester not only reduces mechanical friction from the gearing system, but also provides useful voltage at low proof mass velocities. A 3-dimensional generalized rotational energy harvester model is derived as the basis of the model for the proposed harvester and to predict the upper bound power output. The generalized rotational harvester model makes the assumption that the optimal transducer can be modeled as a viscous damper. It is found that for a given excitation, an optimal level of electrical damping is required to achieve the maximum power output. In general, power output scales with the eccentric proof mass inertia. In real-world applications, the power upper bound will be reduced with increased mechanical damping primarily from friction.

Sputtered bimorph PZT/Ni/PZT thin-films were fabricated as the piezoelectric transducers for the harvester prototype. Compared to off-the-shelf piezoelectric products, these beams provide the appropriate combination of stiffness and material figure of merit for energy harvesting. The 10-beam prototype is characterized on a bench-top swing arm

set-up with a system-level model that incorporates the rotor dynamics, the electromechanical governing equation of a piezoelectric beam, and the analytical magnet model. The swing arm generates a series of sinusoidal excitations that mimics the human upper limb in locomotion, which is a more representative excitation than linear base excitation with respect to wearable energy harvesters. A good match between simulation and measurement is achieved considering the inaccuracy in assembly and the beam to beam variation due to degradation. Under the sinusoidal excitation of 25 degrees and 0.8 seconds, the prototype generates approximately 40 μW whereas the simulation suggests a 230 μW power output can be obtained with a higher but achievable piezoelectric coefficient.

Finally, the characteristics of the harvester prototype is investigated using a potential-well analogy, which provides a reasonable interpretation of measured and simulated power output under different excitations. An intrinsic trade-off between the function threshold and the maximum achievable power is identified for this architecture. The system can be further tuned to approach optimal operation for a given harmonic input. In real-world wrist-worn scenarios, however, the harvester will benefit from the ubiquitous nonperiodic excitations that will help overcome the function threshold issue.

7.6 Appendix

In this discussion, the directional subscripts for rotational variables are dropped since the problem is constrained in the local $X_I Y_I$ wrist plane (see Fig. 7.12). The absolute acceleration of the rotor can be expressed as

$$\mathbf{a}_{abs} = \ddot{\mathbf{x}} = \mathbf{a}_{ref} + \ddot{\boldsymbol{\theta}} \times \mathbf{L} + \dot{\boldsymbol{\theta}} \times (\dot{\boldsymbol{\theta}} \times \mathbf{L}) + 2\dot{\boldsymbol{\theta}} \times \mathbf{v}_{rel} + \mathbf{a}_{rel} \quad (7.14)$$

where \mathbf{a}_{ref} and \mathbf{a}_{rel} are the absolute acceleration of housing, measured from the global

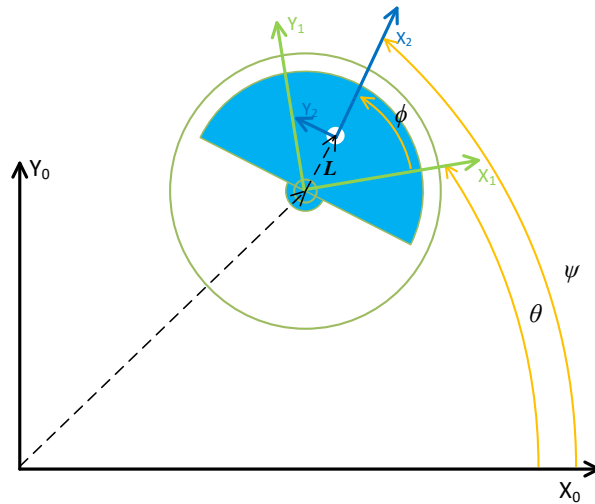


Figure 7.12. Schematic of the generalized rotational harvester model; θ is the rotational excitation to the system, ϕ is the relative rotation of the rotor, and ψ is the absolute rotation of the rotor.

inertial frame, and the relative acceleration of the rotor with respect to the housing, respectively. \mathbf{v}_{rel} is the relative velocity of the rotor with respect to the housing. All the vectors in Eq. (7.14) can be expressed with the Cartesian components along X_I , Y_I , and Z_I axes as

$$\ddot{\boldsymbol{\theta}} \times \mathbf{L} = \ddot{\theta} \mathbf{k}_1 \times L(\cos \phi \mathbf{i}_1 + \sin \phi \mathbf{j}_1) = L\ddot{\theta}(-\sin \phi \mathbf{i}_1 + \cos \phi \mathbf{j}_1) \quad (7.15)$$

$$\begin{aligned} \dot{\boldsymbol{\theta}} \times (\dot{\boldsymbol{\theta}} \times \mathbf{L}) &= \dot{\theta} \mathbf{k}_1 \times (\dot{\theta} \mathbf{k}_1 \times L(\cos \phi \mathbf{i}_1 + \sin \phi \mathbf{j}_1)) \\ &= L\dot{\theta}^2(-\cos \phi \mathbf{i}_1 - \sin \phi \mathbf{j}_1) \end{aligned} \quad (7.16)$$

$$\begin{aligned} 2\dot{\boldsymbol{\theta}} \times \mathbf{v}_{rel} &= 2\dot{\theta} \mathbf{k}_1 \times L\dot{\phi}(-\sin \phi \mathbf{i}_1 + \cos \phi \mathbf{j}_1) \\ &= 2L\dot{\theta}\dot{\phi}(-\cos \phi \mathbf{i}_1 - \sin \phi \mathbf{j}_1) \end{aligned} \quad (7.17)$$

$$\mathbf{a}_{rel} = (-L\dot{\phi}^2 \cos \phi - L\ddot{\phi} \sin \phi)\mathbf{i}_1 + (-L\dot{\phi}^2 \sin \phi + L\ddot{\phi} \cos \phi)\mathbf{j}_1 \quad (7.18)$$

In addition, acceleration of the housing can be expressed along X_I and Y_I axes, which corresponds to the linear acceleration measured by the accelerometer if it is attached

to the housing,

$$\mathbf{a}_{ref} = \ddot{X}\mathbf{i}_1 + \ddot{Y}\mathbf{j}_1 \quad (7.19)$$

Substitute Eq. (7.16) - (7.19) into Eq. (7.15),

$$\mathbf{a}_{abs} = (\ddot{X} - L\ddot{\psi} \sin \phi - L\dot{\psi}^2 \cos \phi)\mathbf{i}_1 + (\ddot{Y} - L\ddot{\psi} \cos \phi - L\dot{\psi}^2 \sin \phi)\mathbf{j}_1 \quad (7.20)$$

Similarly, the gravity vector can also be expressed along X_l and Y_l axes as,

$$\mathbf{g} = g_x\mathbf{i}_1 + g_y\mathbf{j}_1 \quad (7.21)$$

The governing equation can be obtained by substituting Eq. (7.20) and Eq. (7.21) into Eq. (7.1) and Eq. (7.2),

$$\ddot{\psi} = \frac{-(b_m + b_e)\dot{\phi} + mL[(\ddot{X} - g_x) \sin \phi - (\ddot{Y} - g_y) \cos \phi]}{I_g + mL^2} \quad (7.22)$$

which is equivalent to Eq. (7.6).

7.7 References

- [1] B. Ballard, *Designing the Mobile User Experience*, Wiley, 2007. doi:10.1145/1453805.1453841.
- [2] T. Starner, Human-Powered Wearable Computing, *IBM Syst. J.* 35 (1996) 618–629. doi:10.1147/sj.353.0618.
- [3] G.A. Cavagna, N.C. Heglund, C.R. Taylor, Mechanical Work in Terrestrial Locomotion: Two Basic Mechanisms for Minimizing Energy Expenditure, *Am. J. Physiol.* 233 (1977) R243–R261. doi:10.1152/ajpregu.1977.233.5.R243.
- [4] T. Starner, J. A Paradiso, Human Generated Power for Mobile Electronics, *Low-Power Electron.* 1990 (2004) 1–30. doi:10.1.1.104.2324.
- [5] S. Roundy, P.K. Wright, J. Rabaey, A Study of Low Level Vibrations As a Power Source for Wireless Sensor Nodes, *Comput. Commun.* 26 (2003) 1131–1144. doi:10.1016/S0140-3664(02)00248-7.
- [6] P.D. Mitcheson, E.M. Yeatman, G.K. Rao, A.S. Holmes, T.C. Green, Energy Harvesting From Human and Machine Motion for Wireless Electronic Devices, 96 (2008) 1457–1486. doi:10.1109/JPROC.2008.927494.

- [7] M. Hyland, H. Hunter, J. Liu, E. Veety, D. Vashaee, Wearable Thermoelectric Generators for Human Body Heat Harvesting, *Appl. Energy*. 182 (2016) 518–524. doi:10.1016/j.apenergy.2016.08.150.
- [8] J. Yun, S.N. Patel, M.S. Reynolds, G.D. Abowd, Design and Performance of an Optimal Inertial Power Harvester for Human-Powered Devices, *IEEE Trans. Mob. Comput.* 10 (2011) 669–683. doi:10.1109/TMC.2010.202.
- [9] M. Hayakawa, *Electronic Wristwatch with Generator*, US5001685A, 1991.
- [10] E.M. Yeatman, Energy Harvesting from Motion Using Rotating and Gyroscopic Proof Masses, *Proc. Inst. Mech. Eng. Part C J. Mech. Eng. Sci.* 222 (2008) 27–36. doi:10.1243/09544062JMES701.
- [11] T. Xue, S. Kakkar, Q. Lin, S. Roundy, Characterization of Micro-Generators Embedded in Commercial-Off-the-Shelf Watches for Wearable Energy Harvesting, *Proceedings of SPIE - The International Society for Optical Engineering*, p. 98010O. doi:10.1117/12.2218993.
- [12] M. Renaud, P. Fiorini, R. van Schaijk, C. van Hoof, Harvesting Energy from the Motion of Human Limbs: the Design and Analysis of an Impact-Based Piezoelectric Generator, *Smart Mater. Struct.* 18 (2009) 035001. doi:10.1088/0964-1726/18/3/035001.
- [13] S. Ju, C.-H. Ji, Piezoelectric Vibration Energy Harvester Using Indirect Impact of Springless Proof Mass, *J. Phys. Conf. Ser.* 660 (2015) 012122. doi:10.1088/1742-6596/660/1/012122.
- [14] L. Gu, C. Livermore, Impact-Driven, Frequency Up-Converting Coupled Vibration Energy Harvesting Device for Low Frequency Operation, *Smart Mater. Struct.* 20 (2011) 045004. doi:10.1088/0964-1726/20/4/045004.
- [15] M. Pozzi, M.S.H. Aung, M. Zhu, R.K. Jones, J.Y. Goulermas, The Pizzicato Knee-Joint Energy Harvester: Characterization with Biomechanical Data and the Effect of Backpack Load, *Smart Mater. Struct.* 21 (2012) 075023. doi:10.1088/0964-1726/21/7/075023.
- [16] R. Lockhart, P. Janphuang, D. Briand, N.F. De Rooij, A Wearable System of Micromachined Piezoelectric Cantilevers Coupled to a Rotational Oscillating Mass for on-Body Energy Harvesting, *Proc. IEEE Int. Conf. Micro Electro Mech. Syst.* (2014) 370–373. doi:10.1109/MEMSYS.2014.6765653.
- [17] T. Galchev, E.E. Aktakka, K. Najafi, A Piezoelectric Parametric Frequency Increased Generator for Harvesting Low-Frequency Vibrations, *J. Microelectromechanical Syst.* 21 (2012) 1311–1320. doi:10.1109/JMEMS.2012.2205901.

- [18] M. Pozzi, Magnetic Plucking of Piezoelectric Bimorphs for a Wearable Energy Harvester, *Smart Mater. Struct.* 25 (2016) 045008. doi:10.1088/0964-1726/25/4/045008.
- [19] H.T. Luong, N.S. Goo, Use of a Magnetic Force Exciter to Vibrate a Piezocomposite Generating Element in a Small-Scale Windmill, *Smart Mater. Struct.* 21 (2012) 025017. doi:10.1088/0964-1726/21/2/025017.
- [20] P. Pillatsch, E.M. Yeatman, A.S. Holmes, A Piezoelectric Frequency Up-Converting Energy Harvester with Rotating Proof Mass for Human Body Applications, *Sensors Actuators, A Phys.* 206 (2014) 178–185. doi:10.1016/j.sna.2013.10.003.
- [21] T. Xue, S. Roundy, Analysis of Magnetic Plucking Configurations for Frequency Up-Converting Harvesters, *J. Phys. Conf. Ser.* 012098 (2015) 1–5. doi:10.1088/1742-6596/660/1/012098.
- [22] Y. Kuang, Z. Yang, M. Zhu, Design and Characterisation of a Piezoelectric Knee-Joint Energy Harvester with Frequency Up-Conversion through Magnetic Plucking, *Smart Mater. Struct.* 25 (2016) 085029. doi:10.1088/0964-1726/25/8/085029.
- [23] C.B. Yeager, Y. Ehara, N. Oshima, H. Funakubo, S. Trolier-McKinstry, Dependence of $e_{31, f}$ on Polar Axis Texture for Tetragonal $\text{Pb}(\text{Zr}_x\text{Ti}_{1-x})\text{O}_3$ Thin Films, *J. Appl. Phys.* 116 (2014) 104907. doi:10.1063/1.4895339.
- [24] T. Xue, X. Ma, C. Rahn, S. Roundy, Analysis of Upper Bound Power Output for a Wrist-Worn Rotational Energy Harvester from Real-World Measured Inputs, *J. Phys. Conf. Ser.* 557 (2014). doi:10.1088/1742-6596/557/1/012090.
- [25] E. Halvorsen, C.P. Le, P.D. Mitcheson, E.M. Yeatman, Architecture-Independent Power Bound for Vibration Energy Harvesters, *J. Phys. Conf. Ser.* 476 (2013) 117–121. doi:10.1088/1742-6596/476/1/012026.
- [26] T. Xue, S. Roundy, On Magnetic Plucking Configurations for Frequency Up-Converting Mechanical Energy Harvesters, *Sensors Actuators, A Phys.* 253 (2017) 101–111. doi:10.1016/j.sna.2016.11.030.
- [27] H.G. Yeo, S. Trolier-McKinstry, {001} Oriented Piezoelectric Films Prepared by Chemical Solution Deposition on Ni foils, *J. Appl. Phys.* 116 (2014) 014105. doi:10.1063/1.4886597.
- [28] H.G. Yeo, X. Ma, C. Rahn, S. Trolier-McKinstry, Efficient Piezoelectric Energy Harvesters Utilizing (001) Textured Bimorph PZT Films on Flexible Metal Foils, *Adv. Funct. Mater.* 26 (2016) 5940–5946. doi:10.1002/adfm.201601347.
- [29] A. Erturk, D.J. Inman, An Experimentally Validated Bimorph Cantilever Model for

- Piezoelectric Energy Harvesting from Base Excitations, *Smart Mater. Struct.* 18 (2009) 025009. doi:10.1088/0964-1726/18/2/025009.
- [30] P. Pillatsch, E.M. Yeatman, A.S. Holmes, Magnetic Plucking of Piezoelectric Beams for Frequency Up-Converting Energy Harvesters, *Smart Mater. Struct.* 23 (2014) 25009. doi:10.1088/0964-1726/23/2/025009.
- [31] G. Akoun, J. Yonnet, 3D Analytical Calculation of the Forces Exerted between Two Cuboidal Magnets, *IEEE Trans. Magn.* MAG-20 (1984) 1962–1964. doi:10.1109/TMAG.1984.1063554.
- [32] Piezo Systems, PSI-5A4E Piezoceramic Sheets and Plates, (n.d.). <http://piezo.com/prodsheet1sq5A.html> (accessed March 19, 2018).
- [33] S. Roundy, On the Effectiveness of Vibration-Based Energy Harvesting, *J. Intell. Mater. Syst. Struct.* 16 (2005) 809–823. doi:10.1177/1045389X05054042.

CHAPTER 8

CONCLUSIONS

The final chapter summarizes the main conclusions from the project and highlights some original contributions. In addition, some suggestions on future work are provided.

8.1 Summary of Conclusions

This project starts with a literature review on the state-of-the-art of wearable inertial energy harvesting. Human motion presents certain challenges for inertial energy harvesting due to its irregular pattern, low frequency, and large amplitude. Specific observations are made by examining existing commercial products and published research prototypes, which lead to the three objectives of this research project. In short, these objectives are modeling, benchmarking, and prototyping. The project adopts an approach that combines a rotational proof mass with magnetically plucked thin-film PZT beams for inertial wearable energy harvesting. Below are the key findings of this project:

- Chapters 2 and 3 reported the characterization of the electromagnetic microgenerators in COTS watches made by both Seiko and Kinetron. The model-based characterization includes both bench-top and human tests. To tackle the typical low voltage issue for electromagnetic transducers, two devices adopted different approaches while both making use of mechanical

gears. Seiko Kinetic uses a high-ratio gear train to boost the rotor speed. Kinetron MGS employs a spring as an intermediate energy storage element and releases the energy at a higher frequency when the spring overcomes the detent torque. Whereas these mechanisms effectively increase the electrical damping (i.e., electromechanical coupling), the associated mechanical loss, especially the friction from high-speed bearings, significantly lowers the extractable energy at weaker excitations. This argument is corroborated by the experimental results where both watches generate sub-10 μW (sometimes zero) from walking but perform relatively well from more energetic excitations such as jogging.

- Chapter 4 studied three alternative out-of-plane magnetic plucking configurations in addition to the in-plane plucking configuration via an experimentally validated distributed analytical model for magnetically plucked piezoelectric beams. A bifurcation exhibits in the in-plane plucking configuration, which guarantees a dynamic ring down (i.e., more strain cycles for power conversion per pluck). Thus, it is less sensitive to the plucking velocity compared to the out-of-plane plucking configurations, which requires a higher plucking velocity to trigger ring down. Equivalently speaking, the in-plane plucking configurations in general imposes a stronger electromechanical coupling than the out-of-plane plucking configurations. However, for inertial applications, the cogging torque occurring in the in-plane plucking configurations imposes a functioning threshold on the intensity of input, which can be seen in the harvester prototype reported in Chapter 7. In addition, the

experimentally validated models provide a useful simulation tool for potential parametric optimization especially for a controlled input.

- Chapters 5-7 recorded a series of prototyping efforts implementing alternative magnetic plucking configurations with thin-film PZT beams provided by collaborators (Dr. Hong Goo Yeo and Prof. Susan Trolier-McKinstry) from Pennsylvania State University. The first proof-of-concept prototype utilizes an asterisk-shape piezoelectric element with 6 bimorph thin-film PZT beams fabricated on a single Ni substrate. The prototype validated the out-of-plane indirect repulsive plucking configuration (IRC) but suffers from a low yield of electrodes due to its complex geometry. The second IRC prototype with a petal-shape beam layout improved the yield with individually cut beams. The inward trapezoidal beams significantly increase space utilization, which improves power output. In addition, the device thickness was reduced with a more compact design to achieve a better wrist-worn form factor. The third prototype, implementing in-plane plucked piezoelectric beams, further increased the yield, thanks to its smaller geometry (i.e., smaller aspect ratio for the electrode). In addition, the ring down of in-plane plucking is more or less at a consistent frequency, which makes it easier to design the corresponding switching power electronics. The stronger electromechanical coupling and the more apparent cogging torque lead to a more constrained and predictive response of the rotor system and the device was characterized more comprehensively based upon a system-level model compared to previous prototypes. Under the sinusoidal excitation of 25 degrees (amplitude) and 0.8 seconds (period), the prototype

generated approximately $40 \mu\text{W}$ whereas the simulation suggests a further improvement given a higher but achievable material coupling coefficient.

8.1.1 Pseudo Walking vs. Real-world Walking

Pseudo walking, the bench-top excitation generated by a pendulum, has been used throughout the dissertation to characterize wrist-worn energy harvesters. It has been shown that the real-world trajectories of the arm in locomotion require a high-order system for proper approximation [1] and may not be practical for experimental implementation. Pseudo walking reduces the degree of freedoms from 2 to 1 (i.e., there is no elbow in the swing arm). It is a single-frequency approximation of real-world walking based on its dominant frequency. Real-world walking contains many peaks in the frequency spectrum. Based on the observation that the dominant frequency occurs around 1 Hz and varies among the population, a set of frequencies including 1.25, 1.1, 0.91, and 0.8 Hz are chosen as the pseudo walking driving frequencies that correspond to walking profiles from vigorous to mild. In addition, a set of excitation amplitudes including 12.5, 18, and 25 degrees are chosen that cover different arm-swing styles as well.

In general, a higher power output is expected from a real-world walking input compared to its corresponding pseudo walking input (with the dominant frequency and a matching amplitude). This is similar to a typical phenomenon in the field of energy harvesting where the experimental power output is often higher than the simulated power due to the extra excitations occurring in the real world. In this case, the harvester is likely to benefit from the full frequency spectrum with other nondominant-frequency components. In addition, pseudo walking constrains the motion in a single plane whereas in the real

world, any out-of-plane rotation will likely contribute to an increase in power output as it induces the change in the gravitational field.

8.1.2 Geared Electromagnetic Generators vs. Plucked Piezoelectric Harvesters

One important remaining question is how to compare geared electromagnetic generators in COTS watches with plucked piezoelectric harvesters. Due to the gradual change in swing arm excitation parameters over the course and the imperfections in research prototypes, experimental results available for direct comparison are limited. Below are two existing data points:

- The petal-shape piezoelectric harvester prototype versus Kinetron MGS: from a bench-top swing arm sinusoidal input of 30 degrees (amplitude) and 1 second (period), the piezoelectric harvester prototype generates 41.8 μW (projected power output based on the best performing PZT layer, reported in Chapter 5) whereas the Kinetron MGS generates 33.5 μW (reported in internal ASSIST document). Admittedly, the piezoelectric harvester prototype has a larger proof mass, which shall capture more inertial energy from the same input.
- The in-plane plucking piezoelectric harvester prototype versus Kinetron MGS: bench-top characterization for both devices (Chapter 7 and Chapter 3, respectively) shares the same input parameters. All data points suggest that although the actual measured power output from the piezoelectric prototype is lower than what Kinetron MGS generated from these pseudo walking inputs, the piezoelectric samples used do not represent the achievable state-of-art in terms of material coupling coefficient. Simulation results suggest piezoelectric

harvester prototypes outperform Kinetron MGS in pseudo walking given a higher but achievable coupling coefficient.

Although there is no direct comparison in terms of stronger excitations such as jogging, COTS watches are likely to outperform piezoelectric generators for more energetic inputs as the power output of piezoelectric prototypes reaches saturation once the rotor goes into continuous rotation and the beams are plucked consecutively, which can be achieved with a fairly light excitation. This is experimentally demonstrated in the lightly coupled petal-shape harvester prototype.

In a grander view, this comparison can be discussed in the context of generalized viscous-damped rotational harvesters. Geared electromagnetic generators can simply be seen as highly (electrically) damped transducers that come with a cost of additional mechanical damping, whereas plucked piezoelectric harvesters, especially the ones with out-of-plane plucking configurations, are lightly (electrically) damped transducers with no additional mechanical damping. One of the findings on the simulation study of the generalized rotational harvester model is that the optimal damping is dependent on the input. Generally speaking, a smaller damping is preferred for a lighter excitation. In addition, at lower excitations, the energy availability can be greatly reduced with a larger mechanical damping. However, this sensitivity diminishes as the excitation grows stronger. This is in agreement with the experimental results presented earlier.

8.2 Original Contribution

In addition to the findings above, the following highlights the original contribution of this work:

- A generalized viscously damped rotational energy harvester model is proposed to estimate energy availability with respect to specific inertial inputs. Simulation results suggest that for an energy harvester in the size of a wrist-worn watch, the theoretical maximum power output is more than 100 μW from a walking input. Realistic constraints such as friction, however, will limit the achievable power output.
- The comprehensive benchmarking study on the electromagnetic microgenerators in the COTS watches provides new knowledge as there was no previous information available in the public domain on the power output of these watches with respect to specific excitations. System-level models for both watches are derived and experimentally validated.
- Novel out-of-plane magnetic plucking configurations are proposed, studied, and eventually implemented in a series of model-based prototyping efforts. System-level modeling is rarely given on rotational piezoelectric energy harvester devices in the literature. Although the model is prone to numerical error in simulation due to its high nonlinearity, it is a useful tool for future parametric optimization.

8.3 Future Work

Potential future studies on inertial energy harvesting from human motion will be discussed from the perspectives of material fabrication, harvester architecture design, and pathways for commercialization. Recommendations for future work include the following:

- Explore alternative thick thin-film PZT beam fabrication method. The

deposition method (include both sputtering and CSD) attempted by Dr. Hong Goo Yeo encounters a cracking problem once the PZT thickness reaches 5 μm . There is a lack of manufacturability for thick thin-film PZT with high material coupling coefficient between the thickness of 5 and 20 μm . Subtractive method in existing literature suggests that bulk PZT material can be grinded down to 20 μm thick without cracking [2]. Recently reported methods including aerosol [3] and cold sintering [4] are able to push the thickness into the desired region, but the output piezoelectric material tends to suffer from a lower density and a poorer coupling coefficient relatively compared to material produced by more matured methods.

- Study other alternative magnetic plucking methods. The use of soft magnetic material may provide a solution to the detent torque issue without a significant reduction of electromechanical coupling. In addition, since the optimal electrical damping correlates to the excitation itself, a mechanism that can implement an adaptive electromechanical coupling with respect to the inertial input is greatly desired. For instance, the adaptive electromechanical coupling can be a varying air gap between magnets for magnetically plucked piezoelectric beams.
- Investigate feasible pathways for commercialization. Since the target applications of this project are the healthcare and the consumer electronics industries, it is reasonable to talk about how far away the accomplished work in this research project is from real-world implementation. Devices built in this work are, indeed, still in the phase of laboratory prototypes. Preliminary

integration with power conditioning (in collaboration with Miao Meng and Prof. Mehdi Kiani from PSU) has been made to charge an energy storage element (e.g., a capacitor or a supercapacitor). Additionally, the petal-shape prototype can intermittently power an LED directly. Future work should include a further integration with an application-specific integrated circuit (ASIC) with a full system demo. For the energy generation unit itself, there are many challenges facing a potential project to convert the prototyping process to a mass production. Current issues include the low material yield and the complex assembly procedure. It will require significant engineering effort for a robust plucked piezoelectric energy harvesting commercial module to become an eventuality.

8.4 References

- [1] Hejrati, B., Merryweather, A. S., and Abbott, J. J., 2018, “Generating Arm-Swing Trajectories in Real-Time Using a Data-Driven Model for Gait Rehabilitation with Self-Selected Speed,” *IEEE Trans. Neural Syst. Rehabil. Eng.*, **26**(1), pp. 115–124.
- [2] Lockhart, R., Janphuang, P., Briand, D., and De Rooij, N. F., 2014, “A Wearable System of Micromachined Piezoelectric Cantilevers Coupled to a Rotational Oscillating Mass for on-Body Energy Harvesting,” *Proc. IEEE Int. Conf. Micro Electro Mech. Syst.*, pp. 370–373.
- [3] Kuo, C.-L., Lin, S.-C., and Wu, W.-J., 2016, “Fabrication and Performance Evaluation of a Metal-Based Bimorph Piezoelectric MEMS Generator for Vibration Energy Harvesting,” *Smart Mater. Struct.*, **25**(10), p. 105016.
- [4] Wang, D., Guo, H., Morandi, C. S., Randall, C. A., and Trolier-McKinstry, S., 2018, “Cold Sintering and Electrical Characterization of Lead Zirconate Titanate Piezoelectric Ceramics,” *APL Mater.*, **6**(1), p. 16101.

APPENDIX

EXPERIMENTAL METHOD TO OBTAIN MECHANICAL DAMPING RATIO

Whereas modal analysis can be used to characterize mechanical damping for a cantilever beam under base excitation, for a plucked piezoelectric beam, the most convenient way to obtain its mechanical damping ratio is the logarithmic decrement method as the experimental data are often in the form of an underdamped response with decaying oscillation.

The experimental data from the plucked piezoelectric beam can either be an open circuit voltage output or a tip displacement. The logarithmic decrement δ is defined as the natural logarithm of the ratio of the amplitudes of two adjacent peaks and can be expressed as

$$\delta = \ln \frac{x(t)}{x(t+T)} \quad (\text{A.1})$$

where T is the period of oscillation, $x(t)$ is the amplitude at time t , and $x(t+T)$ is the amplitude of the peak at time $t+T$. The damping ratio ζ can be calculated as,

$$\zeta = \frac{1}{\sqrt{1 + \left(\frac{2\pi}{\delta}\right)^2}} \quad (\text{A.2})$$

The mechanical Q factor can be evaluated using the damping ratio as,

$$Q = \frac{1}{2\zeta} \quad (\text{A.3})$$

Note that measurements of peak amplitude can be over any integer multiple of the period to increase accuracy. In this case, Eq. (A.1) can be modified as

$$\delta = \frac{1}{n} \ln \frac{x(t)}{x(t+nT)} \quad (\text{A.4})$$

where n is any integer number of successive peaks.